Doctoral theses at NTNU, 2022:88

Zakari Midjiyawa

Turbulence characterisation in complex fjord topography using measurement and numerical modelling for bridge design

Doctoral thesis

NTNU
Norwegian University of Science and Technology
Thesis for the Degree of
Philosophiae Doctor
Faculty of Information Technology and Electrical
Engineering
Department of Mathematical Sciences

NTNU
Norwegian University of
Science and Technology

Zakari Midjiyawa

Turbulence characterisation in complex fjord topography using measurement and numerical modelling for bridge design

Thesis for the Degree of Philosophiae Doctor

Trondheim, March 2022

Norwegian University of Science and Technology
Faculty of Information Technology and Electrical Engineering
Department of Mathematical Sciences

NTNU
Norwegian University of
Science and Technology

NTNU
Norwegian University of Science and Technology

Thesis for the Degree of Philosophiae Doctor

Faculty of Information Technology and Electrical Engineering
Department of Mathematical Sciences

ISBN 978-82-326-5901-2 (printed ver.)
ISBN 978-82-326-6266-1 (electronic ver.)
ISSN 1503-8181 (printed ver.)
ISSN 2703-8084 (online ver.)

Doctoral theses at NTNU, 2022:88

Printed by NTNU Grafisk senter

To Zenabou Midjiyawa.

Preface

This thesis is submitted in partial fulfilment of the requirement for the degree of Philosophiae Doctorate at the Norwegian University of Science and Technology (NTNU). The work was carried out at the Norwegian Meterological Institute (MET), the Department of Mathematical Science at NTNU, and the Geophysical Institute (UiB). The work was funded by the Norwegian Public Roads Administration (NPRA). Professor Trond Kvamsdal, Professor Joachim Reuder, Dr. Jørn Kristiansen, and Professor Adil Rasheed respectively from NTNU, University of Bergen, MET, and Sintef Digital supervised this work. The thesis consists of an introductory part and three papers published or prepared for submission to international peer-reviewed scientific journals.

- Paper 1: Midjiyawa, Z., Cheynet, E., Reuder, J.,Ágústsson, H., Kvamsdal, T., 2021. Potential andchallenges of wind measurements with met-masts in complex terrain for bridgedesign: Part 1 Integral flow characteristics. J. Wind Eng. Ind. Aerod, https://doi.org/10.1016/j.jweia.2021.104584.
- Paper 2: Midjiyawa, Z., Cheynet, E., Reuder, J.,Ágústsson, H., Kvamsdal, T., 2021. Potential andchallenges of wind measurements with met-masts in complex terrain for bridgedesign: Part 2 Spectral flow characteristics. J. Wind Eng. Ind. Aerod, https://doi.org/10.1016/j.jweia.2021.104584.
- Paper 3: Nested computational fluid dynamic modelling of mean turbulent quantities estimation in complex topography using AROME-SIMRA. Manuscript prepared for submission

In addition to the above papers included in this PhD dissertation, the candidate has the following relevant scientific contribution:

- Paper A: Furevik, B.R.,Ágústsson, H., Lauen Borg, A., Zakari, M., Nyhammer, F., Gausen, M., 2020. Meteorological observations in tall masts for mapping of atmosphericflow inNorwegian fjords. Earth Syst. Sci. Data Discuss. 1 - 28 https://doi.org/10.5194/essd-2020-32

Acknowledgement

Before I started working on this project, I overestimated my patience in real life. The importance of combining core values such as patience, teamwork, and motivation has been reinforced in the course of this work.

The Norwegian Public Roads Administration as part of the Coastal Highway E39 project in Mid-Norway, the Norwegian Meteorological Institute, Sintef Digital, the department of mathematical science at NTNU, and the University of Bergen collaborated on this project. Throughout the project, they provided resources, direction, and supervision.

I owe a great debt of gratitude to my supervisor Prof. Trond Kvamsdal (NTNU) and the Co-supervisors Prof Adil Rasheed (NTNU), Dr. Jørn Kristiansen (Norwegian Meteorological Institute), and Prof. Joachim Reuder (UiB). Furthermore, a special thanks to the scientist Knut Helge Midtbø and Dr. Birgitte Furevik at Meteorological Institute. This work would not have been possible without their patience and guidance.

I am grateful for the help and contribution from the following colleagues and collaborators of this research: Dr. Etyenne Cheynet (UiB), Dr. Hálfdán Ágústsson (Norconsult), Dr. Jon Vegard Venås (SINTEF Digital), Dr. Arne Morten Kvarving (SINTEF Digital), Dr. Konstantinos Christakos (UiB), and Dr. Cyril Palerme (Norwegian Meteorological Institute).

Finally, I would like to express my heartfelt gratitude to my family, who have always been present in high and low times. I consider myself extremely fortunate to have Zenabou Midjiyawa, Abdulwahab Midjiyawa, Aichatou Midjiyawa, Armand Mbianda, Ibrahim Midjiyawa, Karim Sani Ntieche, Maruthamuthu Venkatraman, and Sajjad Haider.

Abstract

On Norway's west coast, the Norwegian Public Road Administration initiated a major infrastructure development project that includes the design and construction of bridges to replace ferries. The width of the fjords, flow conditions, and topography will all influence the type of bridges considered. In this context, since 2014, a measurement program has been running with the purpose of providing data for turbulence characterization in bridge design. Since the available theoretical background, for turbulence characterization in the context of bridge design, is based on flat and homogeneous terrain, the proposed bridge will almost certainly be subjected to environmental conditions that could lead to a catastrophic disaster if turbulence is not properly quantified.

As a result, the first section of this work focused on the similarities and differences in flow characteristics in flat and complex terrain. The second section focused on researching common turbulence characteristics for the purpose of bridge design in multiple fjords. Finally, the study considered the use of numerical simulation for the estimation of flow characteristics relevant to bridge design across the span of the bridge where measurements are limited.

The quantification of turbulence for bridge design revealed that the topographic feature can be divided into two categories: long-fetch winds (winds blowing over an extended stretch of water) and short-fetch winds (winds blowing over irregular and heterogeneous terrain upstream of the measurement location). Wind sector dependency was observed in the estimation of turbulence intensity, normalized vertical standard deviation, and friction velocity. Furthermore, a significant deviation from the assumption of Gaussian fluctuations, which is commonly found in bridge aerodynamic theory, is observed.

The spectral characteristics of turbulence were investigated using one-point and two-point power spectral densities. Surface layer scaling may be possible under neutral conditions provided the velocity spectra are normalized by an adequate friction velocity, according to the findings. The spectral analysis also revealed the importance of sector dependence. The along wind and horizontal cross wind velocity spectra exhibit noticeable features such as large amplitude, spectral plateau, and double spectral peak in the low frequency section. In the vertical velocity spectrum, surface layer scaling may be applicable to both short-fetch and long-fetch winds, similar to examples of flat terrain. In addition, as compared to the flat terrain counterpart, the vertical spectra have a much higher spectral peak. Furthermore, the influence of terrain on flow was evident in the cross-spectrum study, with the co-spectrum and quad-spectrum having similar magnitudes, which is not the case with flat and homogeneous terrain. These common features found in the along wind, cross wind, and vertical wind spectra could have a big impact on the dynamic load estimates for the proposed bridges.

Vertical coherence was analyzed to assess the Davenport similarity, which is generally assumed in flat and homogeneous terrain. The results revealed that at large vertical separations, an alternative model incorporating separation distance and height agrees with the co-coherence estimate. This suggests that the Davenport similarity may be limited for substantial vertical separation in complex topography. The average Davenport coefficient, on the other hand, was found to be consistent with the suggested values in the Norwegian bridge design handbook (N400).

Since a thorough characterization of turbulence for bridge design necessitates the analysis of flow conditions over the bridge span, a nested numerical simulation was established using the macroscale model AROME developed by Météo-France and the microscale model SIMRA developed by SINTEF. The study's initial part concentrated on the validation of the results obtained by estimating the correlation between measurement and numerical simulation. The validation was based on mean turbulent characteristics because the turbulence closure is based on two equations. If the mast is not placed downstream of a steep mountain, the results showed reasonable agreement for wind speed and direction on the fjord's shore. Sector dependence is also apparent when it comes to the correlation of angle of attack, as it was previously observed in the case of the study of integral and spectral characteristics. Furthermore, the angle of attack validation revealed a dependence on the mast location and anemometer height, highlighting the main issue associated with the numerical prediction of vertical velocity in sheltered locations. To adequately establish the source of disparities between observation and numerical simulation when it comes to estimating angle of attack and wind direction at severely sheltered locations, more research is needed.

Contents

Notation

This thesis follows the following general notation conventions.

General notation

C_D	Drag coefficient
C_m	Added mass coefficient
C^i	Davenport coefficient
D	Diameter
F_t	Instantaneous wind force
k	Wavenumber
n_r	Natural frequency
$S(k)$	Wavenumber dependant spectrum of turbulence
S_u	Along wind turbulence spectrum
S_v	Horizontal cross wind turbulence spectrum
S_w	Vertical wind spectrum
S_q	Spectrum of shear force
S_y	Spectrum of deflection
u_t	Instantaneous wind velocity
u_*	Friction velocity
u_{*C}	Friction velocity computed using the classical method
u_{*R}	Friction velocity computed using Klipp method
u_{*M}	Friction velocity computed using flux method
$\bar{u}(z_{)}$	Mean velocity at height z
z	Elevation above ground
ρ	Fluid density
ψ	Mode shape
σ_y	Variance of the deflection
α	Kolmogorov constant
ϵ	Dissipation of turbulence
ϕ_e	Non-dimensional dissipation of turbulence

κ	von Karman constant
λ_1	First Eigen value of the Reynolds stress tensor
λ_3	Third Eigen value of the Reynolds stress tensor
γ_i	Correlation of turbulence

Notation for paper I

a^2_{uw}	Statistical uncertainties in the momentum flux (uw)
a^2_{vw}	Statistical uncertainties in the momentum fluxes (vw)
u	Along wind velocity
v	Horizontal cross wind velocity
w	Vertical wind velocity
x	Along wind direction
y	Horizontal cross wind direction
z	Vertical wind direction
$\overline{u}$	Along wind mean velocity
$\overline{v}$	Cross wind mean velocity
$\overline{w}$	Vertical mean velocity
u'	Along wind fluctuating velocity
u'	Cross wind fluctuating velocity
u'	Vertical wind fluctuating velocity
u_*	Friction velocity computed using the classical method
N	Number of samples
I_u	Along wind turbulence intensity
I_v	Cross wind turbulence intensity
I_w	Vertical wind turbulence intensity
λ_1	First Eigen value of the Reynolds stress tensor
λ_2	Second Eigen value of the Reynolds stress tensor
λ_3	Third Eigen value of the Reynolds stress tensor
$\varLambda_1$	First Eigen vector of the Reynolds stress tensor
$\varLambda_2$	Second Eigen vector of the Reynolds stress tensor
$\varLambda_3$	Third Eigen vector of the Reynolds stress tensor
τ	Time series length
α	Shear coefficient
κ_u	Along wind kurtosis
κ_v	Cross wind kurtosis
κ_w	Vertical wind kurtosis
γ_u	Along wind skewness
γ_v	Cross wind skewness
γ_w	Vertical wind skewness
σ_u	Along wind standard deviation

σ_v	Horizontal cross wind standard deviation
σ_w	Vertical wind standard deviation

Notation for paper II

$\overline{u}$	Along wind mean velocity
$\overline{v}$	Cross wind mean velocity
$\overline{w}$	Vertical mean velocity
u'	Along wind fluctuating velocity
u'	Cross wind fluctuating velocity
u'	Vertical wind fluctuating velocity
u	Along wind velocity
v	Horizontal cross wind velocity
w	Vertical wind velocity
x	Along wind direction
y	Horizontal cross wind direction
z	Vertical wind direction
C^i	Coherence decay coefficient
C_z^u	Along wind Davenport decay coefficient
C_z^v	Cross wind Davenport decay coefficient
C_z^w	Vertical wind Davenport decay coefficient
f_r	Reduced frequency
u_*	Friction velocity computed using the classical method
L_u^x	Along wind integral length scale
S_u	Along wind spectrum of turbulence
S_v	Cross wind spectrum of turbulence
S_w	Vertical wind spectrum of turbulence
S_i	Cross spectrum of turbulence
γ_i	Normalized cross spectrum of turbulence
$\mathrm{Re}(S_{uw}(f))$	Real part of the cross spectrum
$\mathrm{Im}(S_{uw}(f))$	Imaginary part of the cross spectrum
z_{ref}	Reference height

Notation for paper III

r_x	Lateral displacement
r_z	Vertical displacement
r_θ	Torsional displacement
$C_{\mathrm{D}}(\alpha, \beta)$	Drag coefficient function of yaw and attack angle
$C_{\mathrm{L}}(\alpha, \beta)$	Lift coefficient function of yaw and attack angle

$C_{\mathrm{M}}(\alpha, \beta)$	Moment coefficient function of yaw and attack angle
M	Mass matrix
K	Stiffness matrix
F	Wind laod
$\mathbf{u}$	Mean velocity
p	Pressure
θ	Potential temperature
ρ	Fluid density
f	Source term for coriolis force
R_i	Grandiant Richardson number
k	Turbulent kinetic energy
ϵ	Turbulent dissipation
γ_{T}	Turbulent thermal diffusivity
σ_{T}	Turbulent Prandtl number
ν_{T}	Turbulent viscosity
$\mathbf{g}_{\mathrm{D}}$	Dirichlet boundary conditions
$\mathbf{g}_{\mathrm{N}}$	Neumann boundary conditions
$\delta\mathbf{u}$	Test function for velocity
δp	Test function for pressure
$\mathbf{u}_{\mathrm{H}}$	Trial function for velocity
$\mathbf{u}_{\mathrm{D}}$	Velocity lifting function
$\boldsymbol{u}_{\mathrm{H}}^{h}$	Basis function for velocity
p^{h}	Basis function for pressure
$\phi(\mathbf{X_i}, t^*)$	Temporal interpolation of the initial field
$\phi(\mathbf{X_i}, t_k)$	Field values at time t_k from AROME
$\phi(x, y)$	Spacial field values from AROME
$\sigma^*(\boldsymbol{x})$	Recovered velocity gradiant
p^*	Recovered pressure field
U^+	Non-dimensional velocity
y^+	Non-dimensional wall distance
E'	Constant modified for roughness

Introduction

Introduction

1. Motivation

In recent years, there has been a significant rise in demand for road infrastructure, primarily due to increased economic activity [1], as noted in a market survey conducted by [2]. Beam bridges, truss bridges, cantilever bridges, arch bridges, tied arch bridges, suspension and cable stayed bridges are among the various types of bridges in demand, depending on the location or purpose of the bridge. Suspension, or to a lesser extent cable-stayed, bridges have become increasingly popular in recent decades, owing to their ability to accommodate longer spans [3, 4]. As shown in Table 1, a growing number of long span bridges have been found in specific regions with complex topography in recent decades.

The Norwegian Public Road Administration (NPRA) has launched a major infrastructure project called Ferjefri E39, which aims to replace ferries crossing straits of various lengths with bridges of various shapes, sizes, and types between Kristiansand and Trondheim on Norway's western coast in order to boost economic activity and interaction between different regions [6]. An overview of the fjords concerned are shown in Table 2 [3, 7]. The west coast of Norway is characterized by a collision of two erosion surfaces that were elevated during the tertiary [8]. As a result, the topography is often rather complex. Long and deep inlets of the sea surrounded by steep mountain sides formed by glaciation are very common, in addition to rough coastlines with numerous islands. Following the landform classification done in [9], the west coast of Norway is dominated by; Alpine relief, steep slopes, glacially scoured low mountains and valleys, accentuated relief with moderate slopes. Some of these topographic aspects are illustrated in fig. 1. The complexity of the topography, the depth of the fjord, coupled with long crossings in the Norwegian west coast suggest that a new type of long span bridges will be considered in the Ferjefri E39 project. The proposed innovative bridge concepts will be particularly vulnerable to local flow excitation.

Norway is mainly located in the northern latitudes, although it reaches far beyond the arctic circle. On a synoptic scale, the westerlies aloft and recurrent extra-tropical cyclones dominate the atmospheric flow. At the mesoscale level, the

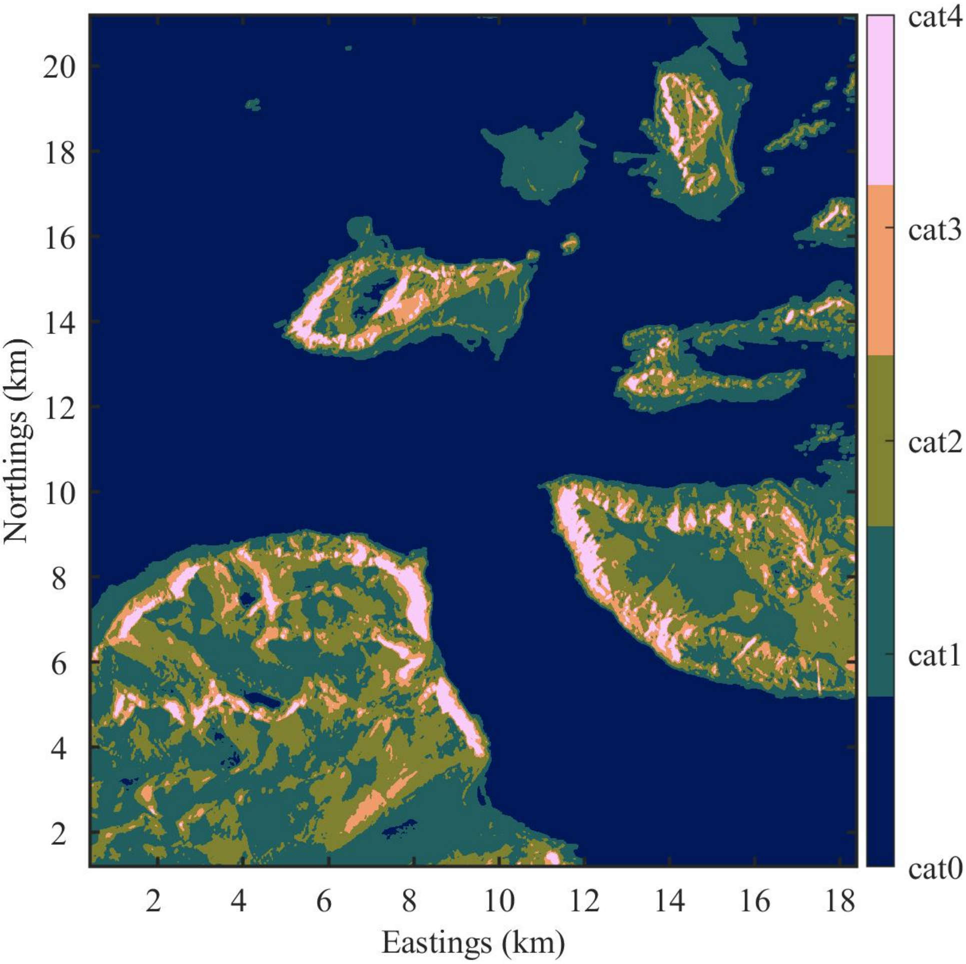

Figure 1: Illustration of Sulafjord topography along with a roughness classification.

Table 1: Long-span cable-suspended bridges built in mountainous terrain (main span larger than 600 m) [5].

Year	Name	Main span (m)	Location
2020	Jinshajiang Hutiaoxia Bridge	766	China
2020	Honghe Jianyuan Bridge	700	China
2020	Jin’an Bridge	1386	China
2018	Xingkang Bridge	1100	China
2018	Chajiaotan Bridge	1200	China
2018	Hålogaland Bridge	1145	Norway
2018	Sunxihe Bridge	660	China
2016	Longjiang River Bridge	1196	China
2016	Yachi Bridge	800	China
2016	Duge Bridge	720	China
2015	Qingshui River Bridge	1130	China
2015	Puli Bridge	628	China
2013	Hardanger Bridge	1310	Norway
2013	Lishui River Bridge	856	China
2012	Aizhai Bridge	1176	China
2009	Sidu River Bridge	900	China
2009	Baling River Bridge	1088	China
2009	Beipanjiang River Bridge	636	China
1992	Gjemnessund Bridge	623	Norway

Table 2: List of fjords involved in the Ferjefri E39 [3, 7]

Fjords	Straight length (m)	Water depth (m)	Mountain height (m)
Sulafjorden	4000	500	660
Vartdalsfjorden	2100	600	1226
Halsafjorden	2000	600	450
Julsundet	1600	600	660
Nordfjorden	1500	500	200
Sognefjorden	3700	1250	510
Bjørnafjorden	5000	600	380
Langenuen	1300	500	720

interaction between the large-scale flows and local topography produces complex flow conditions characterized by large variation in wind speed and direction over small scales. In Figure 2, an example of flow channeling in Sulafjord, Halsafjord, and Julsundet is shown. The relationship between large scale flow, mesoscale, and the local flow scale has been studied by [10]. The study depicts the highly complex flow structure that exists around Norway’s west coast, which is defined by the interaction of offshore, coastal, inland, and mountainous regions.

The design of bridges is based on the characterization of turbulent air flow conditions that are critical in estimating wind loads [11, 12]. In a complex flow

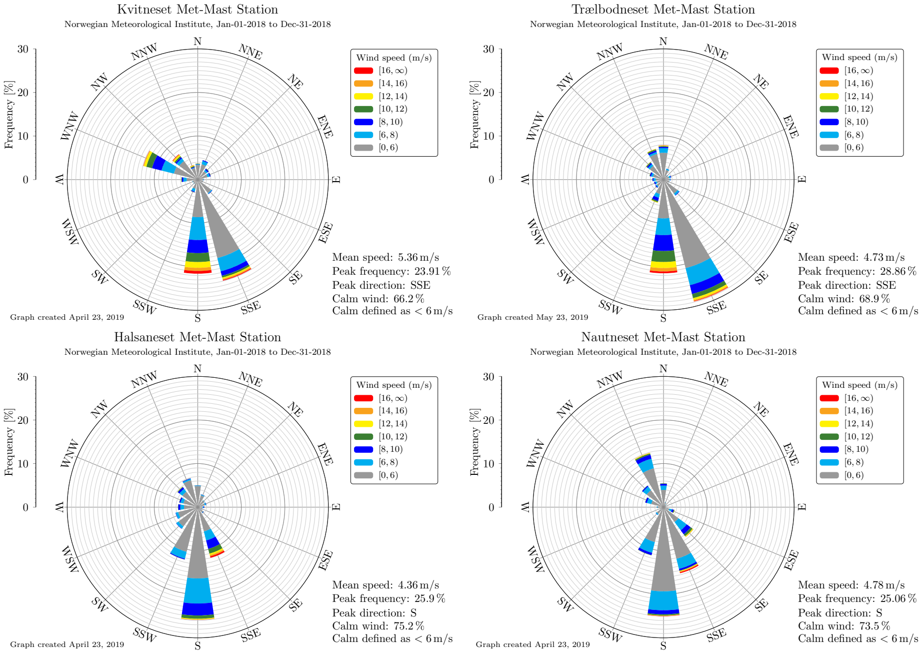

Figure 2: Wind rose measured in Kvitneset, Traelboneset, Halsaneset and Nautneset located in Sulafjord, Halsafjord and Julsundet recorded between 01-01-2018 and 31-12-2019.

and topography environment, the turbulent loading becomes a major concern as the bridge span lengthens [3]. Therefore, the study of turbulence, in the context of bridge design, in regions characterized by complex flow and topography, constitute the main motivation of this research.

2. Research questions

Turbulent loading for bridge design relies heavily on codes and standards where the terrain is assumed flat and uniform. For the design of multiple long span bridges in the west coast of Norway, these assumptions are unlikely to be valid. This is because turbulent spatiotemporal fluctuations on flat and homogenous terrain are expected to differ from those in Norwegian fjord-like topography. Failure to re-evaluate the general assumptions that characterize turbulence loading for the proposed bridges on Norway's west coast could have disastrous consequences. Therefore, it is legitimate to raise the following question: *How can we systematically quantify the differences between the flow characteristics in a Norwegian fjord and those in a traditional flat and homogeneous terrain?*

To the author's knowledge, hardly any systematic analysis of turbulence, for bridge design, using measurements across multiple fjords exists. *The thesis further addresses the existence of common flow characteristics in Norwegian fjord, in terms of one-point and two-point power spectral densities of the wind velocity fluctuations.* Furthermore, multiple studies have demonstrated that measurements made on the fjord's shore cannot be extrapolated to the fjord's interior. Alternative approaches, such as the use of numerical simulations, must be studied to compensate for the lack of relevant measurements for bridge design at sites such as the mid span, which is, of course, crucial for its design. As a result, *the study investigates the application of numerical simulation in the quantification of flow condition in areas where measurements are not available.*

References

[1] T. Kitada, Considerations on recent trends in, and future prospects of, steel bridge construction in japan, *Journal of Constructional Steel Research*, 62:1192–1198 (2006).

[2] Allied-Market-Research, Bridge construction market by type, material, and application: Global opportunity analysis and industry forecast, 2020-2027.

[3] A. Fenerci, Full-scale investigation of the effects of wind turbulence characteristics on dynamic behavior of long-span cable-supported bridges in complex terrain, PhD dissertation, Department of Structural Engineering, Norwegian University of Science and Technology (2017).

[4] J. De Maria, C. Caprani, D. Guo, Long span bridges database.

[5] Z. Midjiyawa, E. Cheynet, J. Reuder, H. Ágústsson, T. Kvamsdal, Potential and challenges of wind measurements using met-masts in complex topography for bridge design: Part ii–spectral flow characteristics, *Journal of Wind Engineering and Industrial Aerodynamics*, 211:104585 (2021).

[6] Samferdselsdepartementet, National Transport Plan 2014 - 2023 (English version), Tech. Rep. Meld. St. 26 (2012 - 2013) Report to the Storting (White Paper)., Norwegian Ministry of transport and communications, Oslo, Norway (2013).

[7] B. R. Furevik, H. Ágústson, A. Lauen Borg, M. Zakari, F. Nyhammer, M. Gausen, Meteorological observations in tall masts for mapping of atmospheric flow in Norwegian fjords, *Earth System Science Data Discussions*, pp. 1–28 (2020).

[8] K. M. Strom, The geomorphology of norway, *The Geographical Journal*, 112:19–23 (1948).

[9] B. Etzelmüller, B. Romstad, J. Fjellanger, Automatic regional classification of topography in norway, *Norwegian Journal of Geology/Norsk Geologisk Forening*, 87 (2007).

[10] M. O. Jonassen, H. Ólafsson, J. Reuder, J. Olseth, Multi-scale variability of winds in the complex topography of southwestern norway, *Tellus A: Dynamic Meteorology and Oceanography*, 64:11962 (2012).

[11] A. G. Davenport, The spectrum of horizontal gustiness near the ground in high winds, *Quarterly Journal of the Royal Meteorological Society*, 87:194–211 (1961).

[12] R. H. Scanlan, The action of flexible bridges under wind, II: Buffeting theory, *Journal of Sound and Vibration*, 60:201–211 (1978).

Theory

Theoretical background

1. Structural load estimation

The theoretical context associated with the static and dynamic study of long span bridges discussed in [1–5] is hereby summarized for completeness' sake. The aim of this section is to clarify the importance of atmospheric turbulence on the design of long span brides.

The equation of motion whose solution gives the dynamic response of a mechanical system is given by

$$\mathbf{M}\ddot{\mathbf{r}} + \mathbf{C}\dot{\mathbf{r}} + \mathbf{K}\mathbf{r} = \mathbf{F} \tag{1}$$

Where $\mathbf{M}$ is the mass matrix, $\mathbf{C}$ the damping matrix, and $\mathbf{K}$ the stiffness matrix associated with the dynamic response of the mechanical system. The solution of Eq. (1) is $\mathbf{r} = [r_x,\ r_z,\ r_\theta]^T$. Where r_x, r_z and r_θ are the lateral, vertical, and torsional displacement, respectively. The wind load $\mathbf{F}$ is expressed in terms of the instantaneous relative wind velocity v_{rel}, instantaneous wind incidence angle α_f, and the aerodynamics coefficients C_{D}, C_{L}, and C_{M} (Drag, lift and moment coefficient) [4].

$$\mathbf{F} = \begin{bmatrix} F_x \\ F_z \\ F_\theta \end{bmatrix} = \frac{1}{2}\rho v_{\mathrm{rel}}^2 B \begin{bmatrix} \frac{D}{B} C_{\mathrm{D}} \cos(\alpha_f - r_\theta) - C_{\mathrm{L}} \sin(\alpha_f - r_\theta) \\ \frac{D}{B} C_{\mathrm{D}} \sin(\alpha_f - r_\theta) + C_{\mathrm{L}} \cos(\alpha_f - r_\theta) \\ B C_{\mathrm{M}} \end{bmatrix} \tag{2}$$

The wind load $\mathbf{F}$ can be rewritten as shown in Eq. (3). Where $\mathbf{A_0}$, $\mathbf{A_1}$, $\mathbf{C}_{\mathrm{ae}}$, and $\mathbf{K}_{\mathrm{ae}}$ are the static load, buffeting load, aerodynamic damping , and aerodynamic stiffness matrices, respectively [4].

$$\mathbf{F} = \mathbf{A_0}\begin{bmatrix} u \end{bmatrix} + \mathbf{A_1}\begin{bmatrix} v_x \\ v_z \end{bmatrix} - \mathbf{C}_{\mathrm{ae}}\begin{bmatrix} \dot{r_x} \\ \dot{r_z} \\ \dot{r_\theta} \end{bmatrix} + \mathbf{K}_{\mathrm{ae}}\begin{bmatrix} r_x \\ r_z \\ r_\theta \end{bmatrix} \tag{3}$$

where u, v_x, and v_z are the along wind, across-bridge, and vertical mean wind speeds, respectively. Combining Eq. (1) and Eq. (3) gives

$$\mathbf{M}\ddot{\mathbf{r}} + \Big[\mathbf{C} + \mathbf{C}_{\mathrm{ae}}\Big]\dot{\mathbf{r}} + \Big[\mathbf{K} + \mathbf{K}_{\mathrm{ae}}\Big]\mathbf{r} = \mathbf{A_0}\Big[u\Big] + \mathbf{A_1}\begin{bmatrix} v_x \\ v_z \end{bmatrix} \tag{4}$$

The dynamic response in frequency domain can therefore be estimated following the relationship between the power spectral density of the response and the buffeting load as shown in Eq. (5) and detailed in [4, 6].

$$\mathbf{S}_\eta(f) = \mathbf{H}(f)\mathbf{S}_{\mathrm{Q}}(f)\mathbf{H}^T(f) \tag{5}$$

with $\mathbf{H}(f)$ given by

$$\mathbf{H}(f) = \Big[-w^2\widetilde{\mathbf{M}} + iw(\widetilde{\mathbf{C}} + \widetilde{\mathbf{C}_{\mathrm{ae}}}) + (\widetilde{\mathbf{K}} + \widetilde{\mathbf{K}_{\mathrm{ae}}})\Big]^{-1} \tag{6}$$

For the definition of $\widetilde{\mathbf{M}}$, $\widetilde{\mathbf{C}}$, $\widetilde{\mathbf{C}_{\mathrm{ae}}}$, $\widetilde{\mathbf{K}}$, and $\widetilde{\mathbf{K}_{\mathrm{ae}}}$ the reader is refered to [4]. The spectrum of the modal wind load $\mathbf{S}_{\mathrm{Q}}$ given in Eq. (5) is shown in Eq. (7) where $\boldsymbol{\psi}$ is the matrix of mode shapes.

$$\mathbf{S}_{\mathrm{Q}} = \int_0^L \int_0^L \boldsymbol{\psi}(y_1)\mathbf{S}_{\mathrm{q}}(y_1, y_2, f)\boldsymbol{\psi}(y_2)d_{y_1}d_{y_2} \tag{7}$$

with the cross spectrum of wind velocities given by

$$\mathbf{S}_{\mathrm{q}}(y_1, y_2, f) = \mathbf{A_1}\begin{bmatrix} S_1(\delta_y, f) & 0 \\ 0 & S_2(\delta_y, f) \end{bmatrix}\mathbf{A_1^T} \tag{8}$$

The real parts of the cross spectral density at two points given in terms of the single point spectra S_{v_x} and S_{v_z} and co-coherence γ_{v_x} and γ_{v_z} function in Eq. (8) are given by [7]

$$S_1(\delta_y, f) = \sqrt{S_{v_x}(y_i, f) \cdot S_{v_x}(y_j, f)} \cdot \gamma_{v_x}(\delta_y, f) \tag{9}$$

$$S_2(\delta_y, f) = \sqrt{S_{v_z}(y_i, f) \cdot S_{v_z}(y_j, f)} \cdot \gamma_{v_z}(\delta_y, f) \tag{10}$$

where $\delta_y = |y_i - y_j|$. Finally at a given abscissa y_r, the power spectral density of the bridge response is given by [7]

$$\mathbf{S}_{y_r}(f) = \boldsymbol{\psi}(y_r)\mathbf{S}_\eta(f)\boldsymbol{\psi}^T(y_r) \tag{11}$$

In the buffeting response study of the suspension bridge, accurate representation of S_{v_x}, S_{v_z}, γ_{v_x}, and γ_{v_z} is critical. The single point spectrum, cross-spectrum of turbulence (spectra of horizontal and vertical incoming velocities at points across the span of the structure), aerodynamic and damping properties are all needed for the structural analysis briefly mentioned above. The conventional modelling approach of the single and cross spectrum of turbulence in bridge design is described in the following section.

2. Spectrum and coherence of turbulence

2.1. Spectrum of turbulence

The spectrum of turbulence is defined as the energy content of turbulence in the frequency domain [8]. The spectrum is subdivided into three main categories: the low frequency part characterized by high energy content, the inertial sub-range characterized by energy cascading down to smaller scales without energy production or consumption, and finally the dissipation range characterized by energy dissipation [8]. Kolmogorov stated that the structure of the smallest eddies, and thus their energy, depends only on the rate of energy dissipation and the viscosity of the fluid [9]. For the intermediate size, known as inertial sub-range, the energy depends only on the dissipation [9]. Using dimensional analysis, the inertial sub-range is described as follow [10]

$$S(k) \approx \alpha k^{-\frac{5}{3}} \epsilon^{\frac{2}{3}} \tag{12}$$

Where $S(k)$ is the enery spectrum of turbulence, k is the wavenumber, and ϵ the dissipation rate. With α being the Kolmogorov constant which usually varies between 0.5 and 0.6. The non-dimensional surface layer spectra derived in [11] is summarized hereby. The non-dimensional dissipation is given by

$$\phi_e \approx \frac{\kappa z \epsilon}{u_*^3} \tag{13}$$

The along wind spectrum in non-dimensional form can be rewritten as

$$\frac{fS_u(f)}{u_*^2} \approx \frac{\alpha}{(2\pi\kappa)^{\frac{2}{3}}} \phi_e^{\frac{2}{3}} \left(\frac{fz}{\bar{u}}\right)^{-\frac{2}{3}} \tag{14}$$

with $f_z = \frac{fz}{\bar{u}}$ the dimensionless frequency, $\bar{u}$ the along wind mean velocity, z the height above ground, f the frequency, $\alpha = 0.55$ the Kolmogorov constant, and $\kappa = 0.4$ the von Karman constant. [12] derived the following spectra of the along wind, horizontal cross wind and vertical wind spectra

$$\frac{fS_u(f)}{u_*^2 \phi_e^{\frac{2}{3}}} \approx 0.3 f_r^{-\frac{2}{3}} \tag{15}$$

$$\frac{fS_v(f)}{u_*^2 \phi_e^{\frac{2}{3}}} \approx 0.4 f_r^{-\frac{2}{3}} \tag{16}$$

$$\frac{fS_w(f)}{u_*^2 \phi_e^{\frac{2}{3}}} \approx 0.4 f_r^{-\frac{2}{3}} \tag{17}$$

Under near neutral condition whereby there is a balance between shear production and viscous dissipation $\phi_e = 1$.

The spectrum of turbulent energy widely used in the field of structural dynamic has been generalized in the form given in Eq. (18) [12–15]

$$\frac{fS_u(f)}{u_*^2} = \frac{Af_r}{(1 + Bf_r^{\alpha})^{\beta}} \tag{18}$$

The spectrum calculated from the measurements is compared to the model proposed by [12], which is used to better understand how topography affects the measured spectrum. The general flat terrain spectra satisfying the assumption of local isotropy in the inertial sub-range are given in Eqs. (19) to (22).

$$\frac{fS_u}{u_*^2} = \frac{102 \cdot f_r}{(1 + 33 \cdot f_r)^{5/3}} \tag{19}$$

$$\frac{fS_v}{u_*^2} = \frac{17 \cdot f_r}{(1 + 9.5 \cdot f_r)^{5/3}} \tag{20}$$

$$\frac{f \cdot Re(S_{uw})}{u_*^2} = \frac{14 \cdot f_r}{(1 + 9.6 \cdot f_r)^{7/3}} \tag{21}$$

$$\frac{fS_w}{u_*^2} = \frac{2 \cdot f_r}{1 + 5 \cdot f_r^{7/3}} \tag{22}$$

where $f_r = \frac{f \cdot z}{U}$, the reduced frequency.

In this thesis, the velocity spectra of point measurements located at the shore of fjords are analyzed. The spectral characteristics of wind turbulence are studied in three Norwegian fjords and compared with the traditional flat terrain spectra given in Eqs. (19) to (22). The local topographic effects are, therefore, quantified at various frequencies of fluctuations. This will help assess the extent of turbulence loading on the future bridges crossing in the fjords of interest.

For the time domain analysis, a wind field simulation must be performed to specified instantaneous wind velocities at different finite element nodes on the line like structure. The simulation requires the mean velocity, the roughness length, a reference height, the friction velocity and the velocity spectra in form given in Eqs. (19), (20) and (22). For the description of the method used in wind field simulation the reader is referred to [16–18].

2.2. ***Normalisation of turbulence spectrum***

Following [19] similarity, the normalization of the spectra illustrated in Eqs. (19) to (22) is based on the friction velocity (u_*) and the anemometer height (z). However, the quantification of the friction velocity results in considerable discrepancies among the different methods considered. Three methods of computation

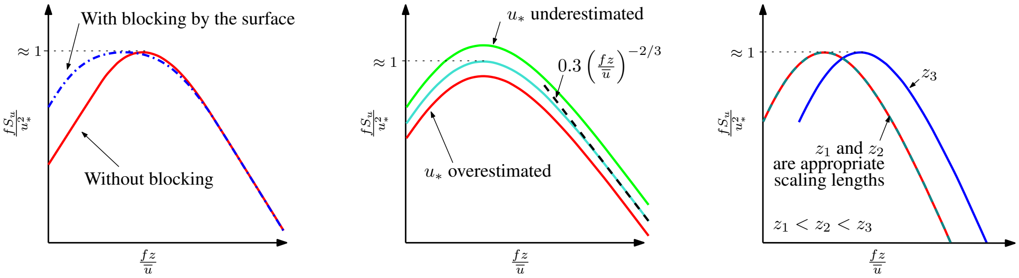

Figure 1: Illustration of the effect of topography (left figure), the friction velocity (middle figure), and the scaling length on the along wind velocity spectrum [25].

of the friction velocity are investigated in this thesis. The method by [20] given in Eq. (23) has been used in numerous studies. However, in complex topography, it requires a coordinate transformation so as to align the flow with streamline coordinates [21–23]. Additional data processing such as double rotation, triple rotation or planar fit are therefore required. The method by [24] offers the advantage of simplicity as it requires just the Eigenvalue and Eigenvector of the Reynolds stress tensor. The third method investigated includes all the horizontal covariance term of the Reynolds stress tensor as shown in Eq. (25). A detail comparison of these different methods has not been established yet. And the considerable amount of data, available in this project, gives an opportunity to assess the different computational methods of the friction velocity.

$$u_{*_\mathrm{C}} = \left[\left(\overline{u'w'}\right)^2 + \left(\overline{v'w'}\right)^2\right]^{1/4} \tag{23}$$

$$u_{*_\mathrm{R}} = \left[(\lambda_1 - \lambda_3)\cos(\beta)\sin(\beta)\right]^{1/2} \tag{24}$$

$$u_{*_\mathrm{M}} = \left[\left(\overline{u'v'}\right)^2 + \left(\overline{u'w'}\right)^2 + \left(\overline{v'w'}\right)^2\right]^{1/4} \tag{25}$$

where u_{*_C}, u_{*_R}, and u_{*_M} are the friction velocity computed using the classical method, the method by [24], and the method including all the horizontal covariance term of the Reynolds stress tensor, respectively. In Eq. (24), λ_1 and λ_3 represent the largest and smallest principal components of the Reynolds stress tensor, respectively. For the definition of β, the reader is referred to [24]. The effect of the choice of the scaling velocity and scaling length in the velocity spectra normalization in the surface layer is illustrated in Figure 1.

2.3. ***Coherence of turbulence***

The correlation of turbulence in frequency space is represented by γ_{v_x}, and γ_{v_z} in equation Eq. (9) and Eq. (10). It comes as a result of the normalization of the cross spectrum measured at two distinct location z_1 and z_2 on the line like structure. The correlation of turbulence, often called co-coherence, is modelled as an exponentially decaying function given by [26]

$$\gamma_i(z_1, z_2, f) = \exp\Big(-C^i f_\mathrm{d}\Big) \tag{26}$$

$$f_\mathrm{d} = \frac{f \mid z_1 - z_2 \mid}{\bar{u}(z_1, z_2)} \tag{27}$$

$$\bar{u}(z_1, z_2) = \frac{\bar{u}(z_1) + \bar{u}(z_2)}{2} \tag{28}$$

where $i = \{u, v, w\}$ and C^i is an empirical decay coefficient. The so-called Davenport model was established in flat and homogeneous terrain and relatively short separation [1, 2]. In structural dynamics, the exponential decay function by [1] has the advantage of simplicity [25]. This form of modelling coherence is adopted by [27] and subsequently in the Handbook N400 [28]. The Davenport coherence model reduces to a single curve when all the coherence functions are expressed as a function of $fd_z/\overline{u}$ ($d_z =\mid z_1 - z_2 \mid$) which is the so-called Davenport similarity.

The Davenport similarity is in good agreement with the measurement for $0.1 \leqslant \gamma_{ii}(z_1, z_2, f) \leqslant 1$, which is luckily the range of interest in engineering applications [23]. The Davenport similarity, however, is not always applicable in complex topography. This may be attributed to wide separation distances, for example. Additional models, such as the one suggested by [29] and shown in Eq. (29) for the modeling of turbulence correlation in highly irregular terrain, have been proposed. The models shown in Eq. (26) and Eq. (29) are compared in terms of modeling coherence for large separation distances in complex topography.

$$\gamma_i(z_1, z_2, f) = A(z_1, z_2, f) \cdot \exp\left(-\frac{2C_2^i f \mid z_1 - z_2 \mid^2}{(z_1 + z_2)\bar{u}(z_1, z_2)}\right) \tag{29}$$

$$A(z_1, z_2, f) = \exp\left(-\frac{\mid z_1 - z_2 \mid}{\bar{u}(z_1, z_2)}\sqrt{(C_1^i f)^2 + (C_3^i)^2}\right) \tag{30}$$

The parameters relevant to buffeting response study, illustrated in this chapter, are analyzed based on met-mast measurements taken on fjord shores. Installation of measurement instruments in remote locations, such as the middle of the fjord, is prohibitively expensive for new infrastructures, such as the case of the E39 project. As a result, numerical modeling is required to investigate the flow condition along the span of the proposed bridge location.

3. Flow modelling in complex topography

This section provides an overview of the equation describing the motion of fluid as well as the various parameterizations used in turbulence modeling. For a detailed description of turbulence modeling relevant to engineering interest, the reader is referred to [30–32].

3.1. ***Governing equations and mathematical models***

Fluid motion is well described using the conservation laws of physics. These are the continuity equation, the momentum equation (Navier-Stokes equations), and the energy equation. These equations are derived from the application of mass balance, Newton's second law of motion, and the laws of thermodynamic to an infinitesimal fluid particle [31].

$$\frac{\partial u_i}{\partial x_i} = 0 \tag{31}$$

$$\rho\frac{\partial u_i}{\partial t} + \rho\frac{\partial u_i u_j}{\partial x_j} = -\frac{\partial p}{\partial x_i} + \mu\frac{\partial^2 u_i}{\partial x_j \partial x_j} + F_{\mathrm{b}} \tag{32}$$

$$\frac{\partial \theta}{\partial t} + \frac{\partial u_i \theta}{\partial x_j} = \alpha\frac{\partial^2 \theta}{\partial x_i \partial x_i} + S_{\mathrm{b}} \tag{33}$$

where u is the instantaneous wind velocity, θ is the instantaneous temperature, and indices $i = (1, 2, 3)$ represents the three cartesian coordinates. F_{b} is the general body force source term and S_{b} is the general heating or cooling source term in the computation domain. The Einstein summation notation is used in the preceding equation. The notation, in general, is defined as follows [30]:

$$\nabla \cdot \mathbf{U} = \frac{\partial u_i}{\partial x_i} = \sum \frac{\partial u_i}{\partial x_i} = \frac{\partial u_1}{\partial x_1} + \frac{\partial u_2}{\partial x_2} + \frac{\partial u_3}{\partial x_3} = \frac{\partial u}{\partial x} + \frac{\partial v}{\partial y} + \frac{\partial w}{\partial z} \tag{34}$$

The differential equations of fluid motion given in Eq. (31), Eq. (32), and Eq. (33) embodied the different characteristics of turbulent motion that are randomness, non-repeatability, sensitivity to initial condition, large range of length scales, enhanced diffusion, three-dimensionality, time dependency, rotationality, and intermittency in both space and time, provided the continuum hypothesis holds [32]. The analytical solution to these equations is still under investigation [33]. However, for very low Reynolds numbers, a direct numerical solution of the Navier-Stokes equations (NS) has been done with prohibitive cost when it comes to flow of engineering interest [34]. Stabilization strategies have been incorporated into the solution of the NS equations for high Reynolds' numbers, which are, typically, flows of engineering interest. These stabilization techniques are commonly referred to as turbulence modeling, and they enable the research and engineering communities to solve various complex flows with a high degree of accuracy. Turbulence modeling in general can be divided into two categories. These are determined by the type of averaging applied to the NS equation. The sections that follow provide an overview of the most used turbulence closures available in the literature.

3.2. ***Time averaging and RANS turbulence modelling***

The Reynolds decomposition of the atmospheric wind can be expressed as $u_i = \overline{u_i} + u_i^{'}$. Where u_i represents the instantaneous velocity given in Eq. (31) and Eq. (32). The velocity vector u_i is divided into a mean velocity $\overline{u_i}$ defined in Eq. (35) and a fluctuating velocity $u_i^{'}$ around the mean value. It is possible to derive the so-called Reynolds Average Navier-Stokes equations (RANS) provided $\overline{u_i^{'}} = 0$ and $\overline{\overline{u_i}} = \overline{u_i}$. A similar decomposition is also applied on the pressure $p = \overline{p} + p^{'}$ and temperature $\theta = \overline{\theta} + \theta^{'}$.

$$\overline{u_i} = \frac{1}{2T} \int_{-T}^{T} u_i dt \tag{35}$$

The RANS equations are given as follow

$$\frac{\partial \overline{u_i}}{\partial x_i} = 0 \tag{36}$$

$$\rho_0 \frac{\partial \overline{u_i}}{\partial t} + \rho_0 \frac{\partial \overline{u_i u_j}}{\partial x_j} = -\frac{\partial \overline{p}}{\partial x_i} + \mu \frac{\partial^2 \overline{u_i}}{\partial x_j \partial x_j} - \frac{\partial \tau_{ij}}{\partial x_j} + F_{\mathrm{b}} \tag{37}$$

$$\frac{\partial \overline{\theta}}{\partial t} + \frac{\partial \overline{u_i} \overline{\theta}}{\partial x_j} = \alpha \frac{\partial^2 \overline{\theta}}{\partial x_i \partial x_i} - \frac{\overline{u_i^{'} \theta^{'}}}{\partial x_i} + S_{\mathrm{b}} \tag{38}$$

with $\alpha = k/\rho c_p$ the thermal diffusivity (c_p is here being the specific heat at constant pressure), ρ_0 is the reference fluid density, $\overline{p}$ is the hydrodynamic pressure. F_{b} is present only in the vertical momentum equation to simulate rising and sinking due to buoyancy effect [35]. The tensor of turbulent shear stress is defined as

$$\tau_{ij} = \rho_0 \overline{u_i^{'} u_j^{'}} \tag{39}$$

The equations Eq. (36), Eq. (37), and Eq. (38), along with the definition of turbulence stress given in Eq. (39), describe the mean or averaged quantities of a turbulent flow field under moderate stratification and small temperature variation [36]. The three velocities (u_1,u_2, and u_3), the pressure, and the six Reynolds' stresses due to the symmetry of the Reynolds' stress tensor ($\overline{u_i^{'}u_j^{'}}$) are the ten unknowns in these equations. In the case of thermal stratification, the temperature θ and turbulent heat fluxes $\overline{u_i^{'}\theta^{'}}$ are additional unknowns. However, the number of equations does not equal the number of unknowns. This is referred to as the turbulence closure problem. Modeling of turbulence quantities $\overline{u_i^{'}u_j^{'}}$ and $\overline{u_i^{'}\theta^{'}}$ must be introduced.

In a broad sense, an exact equation for Reynolds' stresses can be derived [30, 37]. Using Einstein's notation, the prognostic equation for the six components of the Reynolds' stress tensor is given below

$$
\begin{aligned}
\frac{\partial \overline{u_i^{'}u_j^{'}}}{\partial t} + \overline{u_k^{'}}\frac{\partial \overline{u_i^{'}u_j^{'}}}{\partial x_k} = & -\left(\overline{u_i^{'}u_k^{'}}\frac{\partial \overline{u_j^{'}}}{\partial x_k} + \overline{u_j^{'}u_k^{'}}\frac{\partial \overline{u_i^{'}}}{\partial x_k}\right) + \overline{\frac{p^{'}}{\rho}\left(\frac{\partial u_i^{'}}{\partial x_j} + \frac{\partial u_j^{'}}{\partial x_i}\right)} \\
& - \frac{\partial}{\partial x_k}\left(\overline{u_i^{'}u_j^{'}u_k^{'}} + \frac{\overline{p^{'}u_j^{'}}}{\rho}\delta_{ik} + \frac{\overline{p^{'}u_i^{'}}}{\rho}\delta_{jk}\right) \\
& + \nu\frac{\partial^2 \overline{u_i^{'}u_j^{'}}}{\partial x_k \partial x_k} - g_i\beta\overline{u_j^{'}\theta^{'}} - g_i\beta\overline{u_i^{'}\theta^{'}} - 2\nu\overline{\frac{\partial u_i^{'}}{\partial x_k}\frac{\partial u_j^{'}}{\partial x_k}}
\end{aligned}
\tag{40}
$$

where δ_{jk} is the Kronecker delta. The first term in the left-hand side of Eq. (40) is the decay of turbulent stress, the second is the turbulent transport by convection. On the right-hand side, the first term is the turbulent production, the second term is the pressure strain, the third and fourth term are the turbulent diffusion, and the fifth term is the production of turbulence due to buoyancy. The final term is the turbulent dissipation usually denoted as ϵ_{ij}.

The turbulence model that includes the solution of the six transport equations for the computation of turbulence stresses shown in Eq. (40) is known as the Reynolds Stress Model (RSM). The RSM is valid for most engineering flows. However, the model is computationally expensive, and it also necessitates modeling for the triple correlation and pressure diffusion contained in the diffusion term ($\overline{u_i^{'}u_j^{'}u_k^{'}}$, $\overline{p^{'}u_j^{'}}\delta_{ik}$, $\overline{p^{'}u_i^{'}}\delta_{jk}$), the pressure strain, and the dissipation tensor ϵ_{ij} [30, 37]. Additional modelling is therefore included for these terms in the solution of the six transport equations for turbulence stresses in the RSM. Eddy viscosity models, on the other hand, are a class of reasonably inexpensive turbulence closure models with a high level of accuracy [38] that are frequently utilized in the research community and are summarized in the following.

The Boussinesq assumption [39, 40] models the turbulent stresses (τ_{ij}) present in the momentum equation by introducing an eddy viscosity. The assumption is analogous with the Newton's law of viscosity for Newtonian fluids [41]. As illustrated in Eq. (41) ν_T is called turbulence viscosity. These are known as linear eddy viscosity models. However, if the non-linear terms of the strain rates are included, the outcome is a different class of turbulence model called non-linear eddy viscosity model detailed in [42–45] and not discussed in this thesis.

$$\tau_{ij} = \nu_\mathrm{T}\left(\frac{\partial \overline{u_i}}{\partial x_j} + \frac{\partial \overline{u_j}}{\partial x_i}\right) \tag{41}$$

In a more general form, meaning the equation remain consistent when $(i = j)$, the turbulent stresses are rewritten as

$$\tau_{ij} = \nu_\mathrm{T}\left(\frac{\partial \overline{u_i}}{\partial x_j} + \frac{\partial \overline{u_j}}{\partial x_i}\right) - \frac{2}{3}k\delta_{jk} \tag{42}$$

Re-writing the general Reynolds Average Equation using the Eddy Viscosity Concept introduced in Eq. (42) gives

$$\rho_0\frac{\partial \overline{u_i}}{\partial t} + \rho_0\frac{\partial \overline{u_i}\overline{u_j}}{\partial x_j} = -\frac{\partial \overline{P}}{\partial x_i} + \frac{\partial}{\partial x_j}\left[(\nu + \nu_\mathrm{T})\left(\frac{\partial \overline{u_i}}{\partial x_j} + \frac{\partial \overline{u_j}}{\partial x_i}\right)\right] + F_\mathrm{b} \tag{43}$$

with $\overline{P} = \overline{p} + \frac{2}{3}k$ and k being the turbulence kinetic energy. For the temperature equation, a similar approximation is introduced for the heat fluxes

$$\overline{u_i'\theta'} = -\alpha_\mathrm{T}\frac{\partial \overline{\theta}}{\partial x_i} \tag{44}$$

where the turbulent thermal diffusivity is given by

$$\alpha_\mathrm{T} = \frac{\mu_\mathrm{T}}{\sigma_\theta} \tag{45}$$

with σ_θ the turbulent Prandtl number. The Temperature equation can therefore be written as follow

$$\frac{\partial \overline{\theta}}{\partial t} + \frac{\partial \overline{u_i}\overline{\theta}}{\partial x_j} = \alpha\frac{\partial^2 \overline{\theta}}{\partial x_i \partial x_i} - \frac{\partial}{\partial x_j}\left(\alpha_t\frac{\partial \overline{\theta}}{\partial x_j}\right) + S_\mathrm{b} \tag{46}$$

Using the same principle, it is possible to construct a similar transport equation for species or pollutant transport in the fluid [31]. The eddy viscosity is assumed to be proportional to a velocity scale and a length scale. The number of equations required for eddy viscosity estimate determines the classification of eddy viscosity models (EVM).

Zero equation turbulence modelling

Often called the mixing length model, the eddy viscosity is modelled following the dimensional analysis based on an analogy with the molecular viscosity. The eddy viscosity, whose unit is m^2/s, can be assumed proportional to a velocity scale and length scale. It can be written as follows if the velocity scale is additionally assumed to be proportional to a length scale and velocity gradient.

$$\nu_{\mathrm{T}} = l_{\mathrm{m}}^2 \frac{\partial \bar{u}}{\partial x} \tag{47}$$

where l_{m} is the mixing length. This is the earliest turbulence model developed by Prandtl [46] and is commonly referred to as the Prandtl mixing length model. There are algebraic expressions for the mixing length in channel and pipe flows [47–51]. However, in complex topography, where there are several turbulent length scales, estimating the mixing length becomes challenging.

One equation turbulence modelling

To improve the zero-equation turbulence model further, a conservation equation for the eddy viscosity is solved, as shown in Eq. (48). The Spalart-Allmaras model is the most widely used one equation turbulence model [52]. The model, which was developed specifically for the aerospace industry, is computationally inexpensive for attached wall bounded flows and flows with mild separation and recirculation [53]. When it comes to predicting flows with rotation and streamline curvature, the use of one equation is limited [54].

$$\frac{\partial \nu_{\mathrm{T}}}{\partial t} + \overline{u_i}\frac{\partial \nu_{\mathrm{T}}}{\partial x_i} = \frac{1}{\sigma}\left[\nabla \cdot ((\nu + \nu_{\mathrm{T}})\nabla \nu_{\mathrm{T}}) + C_{b2}(\nabla \nu_{\mathrm{T}})^2\right] + P(\nu_{\mathrm{T}}) - D(\nu_{\mathrm{T}}) \tag{48}$$

where σ and C_{b2} are the coefficient for the Spalart-Allmaras model. $P(\nu_{\mathrm{T}})$ and $D(\nu_{\mathrm{T}})$ are the production and dissipation term of the model. Additional model such as Baldwin-Barth model [55], Rahman-Agarwal-Siikonen Model [56], Wray-Agarwal Model [57], and Shuai-Agarwal [58] are available in the literature but their use is limited when it comes to modelling flow related to complex topography.

Two equations turbulence modelling

In the field of micrometeorology, this is the most used class of turbulence model [59]. Following the proportionality between the eddy viscosity and the velocity and length scales, the models solve one equation for estimating the velocity scale and another equation for estimating the length scale. A transport equation for the turbulence kinetic energy defined in Eq. (49) is solved, and a second transport equation for the length scale is solved. Turbulent dissipation, shown in Eq. (50), and specific dissipation defined in Eq. (51), are two of the most used equations for length scale estimation.

$$k = \frac{1}{2}\overline{u_i^{'}u_i^{'}} \tag{49}$$

$$\epsilon = \nu\overline{\frac{\partial u_i^{'}}{\partial x_j}\frac{\partial u_i^{'}}{\partial x_j}} \tag{50}$$

$$\omega = \frac{\epsilon}{C_\mu k} \tag{51}$$

One of the most widely used two-equation turbulence closure is the $k-\epsilon$ model. In its general form, the velocity scale is defined as $k^{1/2}$ and the length scale is given by $k^{\frac{3}{2}}/\epsilon$. The transport equation for the turbulence kinetic energy (TKE) and dissipation are, therefore, given by

$$\nu_t = C_\mu f_\mu \frac{k^2}{\epsilon} \tag{52}$$

$$\frac{\partial k}{\partial t} + \frac{\partial (k u_j)}{\partial x_j} = \frac{\partial}{\partial x_j}\left[\frac{1}{\rho}\left(\mu + \frac{\mu_t}{\sigma_k}\right)\frac{\partial k}{\partial x_j}\right] + \frac{\mu_t}{\rho}S^2 - \epsilon \tag{53}$$

$$\frac{\partial \epsilon}{\partial t} + \frac{\partial (\epsilon u_j)}{\partial x_j} = \frac{\partial}{\partial x_j}\left[\frac{1}{\rho}\left(\mu + \frac{\mu_t}{\sigma_e}\right)\frac{\partial \epsilon}{\partial x_j}\right] + \frac{\epsilon}{k}\left(C_{1\epsilon}f_{\epsilon 1}\frac{\mu_t}{\rho}S^2 - C_{2\epsilon}f_{\epsilon 2}\epsilon\right) - \epsilon \tag{54}$$

These represent a family of two equation $k-\epsilon$ turbulence models. The coefficients C_μ, $C_{1\epsilon}$, and $C_{2\epsilon}$ are semi-empirically determined from experimental data. There is a wide variety of two equation models. The main features distinguishing them are the treatment of the equation at the wall and the form of turbulence dissipation equation [60]. Furthermore, these models can be classified as high and low Reynolds number. The use of which is determined by the nature of the problem at hand. The high Reynolds number are characterized by the fact that the damping function $f_{\epsilon 1}, f_{\epsilon 1}, f_{\mu}$ are all set to 1. This requires the use of wall functions, which necessitates the first grid being in the logarithmic layer. The standard high Reynolds number model has coefficient $C_{\mu} = 0.09, C_{1\epsilon} = 1.44, C_{2\epsilon} = 1.92$ with the turbulent Schmidt number σ_k and σ_{ϵ} equal to 1.0 and 1.3 respectively [61]. The standard model has the advantage simplicity and stability but with the disadvantage of poor prediction in swirling, rotating, and flows with strong separation [62, 63].

Further improvements have been attempted which result in other high Reynolds number variant [64]. Most common examples are the Renormalization Group $k-\epsilon$ (RNG) [65] or the realizable $k-\epsilon$ model [66–68]. The RNG model uses the RNG approach which is a mathematical technique used to derive the k equation. This results in the modification of the ϵ equation. Along with different model constant, the model has shown improved accuracy in rotating flows. The realizable, on the other hand, uses a variable C_{μ} constant as shown in Eq. (55) along with an improve equation for ϵ [66].

$$C_{\mu} = \frac{1}{A_0 + A_{\mathrm{S}} \frac{u^* k}{\epsilon}} \tag{55}$$

where A_0, A_{S}, and u^* are function of velocity gradient in the flow field. The model has shown improved performance for boundary layer flow under strong pressure gradient or separation, rotation, recirculation, and streamline curvature [59]. This makes it a good trade-of model of turbulence in term of simplicity and accuracy.

Models using damping functions $f_{\epsilon 1}$, $f_{\epsilon 1}$, f_{μ} different than 1 are referred to as low Reynolds number turbulence models. As a result, the model can be integrated into the wall [69]. The basic goal of the damping function is to generate a viscous effect near the wall. This necessitates placing the initial grid close to the wall, which involves having the first grid in the viscous sublayer. The literature contains a wide range of these models, each with its own set of damping functions and turbulence model coefficients [70–73].

In the case of atmospheric flow, using a low Reynolds number in the traditional sense will necessitate an excessive number of grid cells to fulfill the model grid requirement. However, a LRN model combined with a wall function modification can still be used to account for the influence of wall roughness [74–76]. The HRN $k-\omega$ by Wilcox [77, 78] is a separate kind of model that does not require damping function to effectively recreate asymptotic behavior in the near wall. Menter proposed a blending of these models, resulting in the commonly used shear stress transport (SST) $k-\omega$, by taking advantage of the near wall prediction of the $k-\omega$ and the far field capabilities of the $k-\epsilon$ [79, 80].

RANS models summarized in this section, classified as EVM or models in which an algebraic or differential equation is solved for the Reynolds Stress tensor $(\overline{u_i^{'} u_j^{'}})$

have the advantage of simplicity and computational cost effectiveness. When correctly validated, the RANS turbulence model based on eddy viscosity can provide useful information in the context of bridge design. They can be used to estimate mean quantities such as mean wind velocity, mean wind direction, mean angle of attack, and mean shear coefficient. The theory of bridge aerodynamics, on the other hand, is based on assumptions such as flow Gaussianity, which can only be verified by modeling instantaneous wind velocities using turbulence modeling based on space averaging rather than time averaging. If the instantaneous velocities can be predicted, turbulence spectra, coherence, and the assumption of flow Gaussianity may be examined along the fjord to better understand their variations over the bridge span.

3.3. ***Space averaging and LES turbulence modelling***

Large Eddy Simulation (LES) is a type of turbulence modeling that is a compromise between full turbulence modeling (as shown in the EDV model) and direct numerical simulation (DNS). DNS, which does not require any modeling, resolves all turbulence scales up to the dissipation scales. RANS, on the other hand, models all turbulence scales from the integral to the dissipation range, as shown in the previous sections. Modeling of only a portion of the inertial sub-range up to the beginning of the dissipation range is required for LES, which is a trade-off between RANS and DNS [32]. Additional LES grid refinement eventually leads to DNS.

In RANS, temporal averaging is used to obtain the RANS equation, and subsequent turbulent stresses are modeled, as shown in section subsection 3.2. The NS equation in LES is filtered to provide a volume average NS equation. The instantaneous variable ϕ is decomposed as $\phi(x,t) = \widetilde{\phi(x,t)} + \phi^{'}(x,t)$. $\widetilde{\phi(x,t)}$ is the space filtered variable defined as

$$\widetilde{\phi(x,t)} = \frac{1}{\Delta x} \int_{x-\frac{1}{2}}^{x+\frac{1}{2}} \phi(\xi,t) d\xi \tag{56}$$

In LES, the filtered variable is a function of both space and time. In contrast to RANS where time average of the fluctuating component is zero, the subgrid quantity and the filtered quantities are characterized by $\widetilde{u_i^{'}} \neq 0$ and $\widetilde{\widetilde{u}}_i \neq \widetilde{u}_i$. The resulting filtered NS equation are given as

$$\frac{\partial \widetilde{u}_i}{\partial x_i} = 0 \tag{57}$$

$$\frac{\partial \widetilde{u}_i}{\partial t} + \frac{\partial \widetilde{u}_i \widetilde{u_j}}{\partial x_j} = -\frac{1}{\rho}\frac{\partial \widetilde{p}}{\partial x_i} + \nu \frac{\partial^2 \widetilde{u}_i}{\partial x_j \partial x_j} - \frac{\partial \tau_{ij}}{\partial x_j} \tag{58}$$

with τ_{ij} given by

$$\tau_{ij} = \widetilde{u_i u_j} - \widetilde{u}_i \widetilde{u}_j \tag{59}$$

The subgrid stresses given in Eq. (59) can also be re-arranged as a sum of Leonard stresses ($L_{ij} = \widetilde{\widetilde{u}_i \widetilde{u}_j} - \widetilde{u}_i \widetilde{u}_j$), cross stresses ($C_{ij} = \widetilde{\widetilde{u}_i u_j^{'}} + \widetilde{\widetilde{u}_j u_i^{'}}$) and Reynolds stresses ($R_{ij} = \widetilde{u_i^{'} u_j^{'}}$). The modelling of the subgrid stresses τ_{ij}, in the context of finite volume method that uses the grid size as filter width, represent the different models available in the LES technique.

The first and simplest method is the Smagorinsky LES closure [81] which uses a formulation like the Boussinesq assumption used in RANS.

$$\tau_{ij} = -\nu_{\mathrm{sgs}} \left(\frac{\partial \widetilde{u}_i}{\partial x_j} + \frac{\partial \widetilde{u}_j}{\partial x_i} \right) \tag{60}$$

$$\nu_{\mathrm{sgs}} = (C_{\mathrm{S}} \mathit{\Delta})^2 S \tag{61}$$

where S is the general three-dimensional velocity gradient and C_{S} is the Smagorinsky constant. Similar to the mixing length, the Smagorinsky constant C_{S} is flow dependent. This represents a limitation of the Smagorinsky LES turbulence closure. Several improvements have been done such as the Deardoff [82] subgrid model available in PALM [83]. The dynamic model, on the other hand, requires an additional equation which is solved in order to estimate C_{S} in the flow field [84, 85]. Additional class of LES model includes scale-similarity model (SSM) where the SGS stresses are not modelled following the eddy viscosity formulation. An example of this model is the Bardina model [86] whereby the Leonard stresses are computed but the cross and Reynolds stresses are modeled.

A model based on the eddy viscosity idea, or a scale similarity model is referred to as pure LES. Some of the earlier work involving LES in the boundary layer can be found in [87, 88]. Hybrid models, on the other hand, have gained popularity in recent decades among scientists. The first of these is known as detached eddy simulations, and it employs a single equation, URANS, in the attached area of the flow and LES in the detached region, or region of massively separated flow [89]. Depending on the turbulent length scale and grid spacing, the model switches from URANS to LES.

In Eq. (62), an illustration of the k equation for the SST $k - \omega$ - IDDES (Improved Delayed Detached Eddy Simulation) is shown. The model transitions from URANS to LES based on the length scaled l_{IDDES}, using the same equation as the SST $k - \omega$ URANS turbulence model. Due to the introduction of the shield function, which delays the switch to LES mode until the flow is outside the turbulent boundary layer, the delayed improved model is obtained based on the original DES model [90].

$$\frac{\partial \rho k}{\partial t} + \nabla(\rho u_i k) = \nabla\left[\left(\mu + \frac{\mu_\mathrm{T}}{\sigma_k}\right)\nabla k\right] + P_k - \rho\frac{k^{3/2}}{l_\mathrm{IDDES}} \tag{62}$$

$$l_\mathrm{IDDES} = \widetilde{f_\mathrm{d}}(1+f_\mathrm{e})l_\mathrm{RANS} + (1-\widetilde{f_\mathrm{d}})l_\mathrm{LES} \tag{63}$$

where $\widetilde{f_\mathrm{d}}$, f_e, l_RANS, l_LES are defined in [90]

The efficiency and computational cost of LES modeling will be improved by using the SST model in the near wall region and the LES model in the far field. Simulating flow in complex topography with variable roughness is costly since pure LES requires the first grid to be placed in the viscous sublayer. Modifications to the URANS model's wall function can be made to incorporate roughness characteristics of complex topography into a hybrid turbulence modeling. In the field of micrometeorology, the hybrid RANS-LES could be a viable option in terms of the trade-off between accuracy and computation cost [91].

*3.4. **Modelling approach for the E39 project***

When it comes to modeling flow phenomena in complex topography, the various turbulence closures mentioned in subsection 3.2 and subsection 3.3 provide a variety of alternatives. The capabilities of computing mean quantities pertinent to bridge design are provided by RANS turbulence closure. Fluctuating quantities, on the other hand, may be computed using LES. These can then be used to estimate the low frequency section of the velocity spectra as well as the coherence, both of which are important for line-like structure buffeting response analysis.

RANS has some limitations in wind engineering, despite its computational efficiency. The inlet boundary conditions and initial conditions, for example, must be suitably chosen in two equations $k-\epsilon$ turbulence. The inlet boundary condition is determined by the fact that the approach flow should be treated as a homogenous flow. This means that in the absence of any obstruction, any variable's streamwise gradient should be zero. The inlet velocity profile, turbulence profiles, ground shear stress, and turbulence model must all be in equilibrium to achieve this [92]. The profiles obtained from the solution of 2-dimensional momentum, ϵ, and k equations under the assumption of zero vertical velocity, constant pressure, and constant shear stress still result in turbulence decay in the absence of obstruction [93, 94]. To address the problem of flow homogeneity in ABL flows, several solutions have been explored. These are

- The application of constant shear stress at the top boundary in streamwise direction along with the modification of turbulence constant as suggested by [92]. This guarantees geostrophic flow by ensuring that the flow is driven by a shear stress at the upper boundary.

- The modification of the law of the wall, as well as the solution to the issue of turbulent kinetic energy overproduction near the wall as suggested by [93].
- In order for the profiles to satisfy the turbulence model equation, new and generic inlet velocity and turbulence profiles must be developed as given in [95, 96].
- The implementation of the wind source terms in the momentum equation so that the profiles of velocity, k, and ϵ remain homogeneous throughout the simulation domain as described in [97].
- Another option is to shrink the computational region to lessen the differences between the approach and incident flows. This alternative, however, is not practical due to the domain's size, which is in the range of 20 to 40 km, and the potential numerical errors such as flow reflection at the boundary that may be generated.

A numerical modeling setup using AROME nested to SIMRA (Semi Implicit Reynolds Averaged) developed by SINTEF is considered in this thesis [98]. The Norwegian Meteorological Institute uses AROME, a limited-area numerical weather forecast [99]. It gives wind, temperature, and precipitation forecasts for Norway. To cover the entire Nordic region, it used a 2500 m grid size. The ECMWF (European Center for Medium-Range Weather Forecasts) worldwide numerical weather prediction program is used to initialize AROME computations.

SIMRA, on the other hand, is a computational fluid dynamics tool that uses a modified $k - \epsilon$ turbulence closure. For the solution of the Boussinesq equation, it uses a finite element method with linear basis function. SIMRA has been used to predict turbulent conditions at several Norwegian airports [98].

The nested calculation ensures that the initial and inlet boundaries from AROME are used, which employed data assimilation and ensemble prediction to reduce modeling error associated with fluid flows' chaotic character [100]. Modified wall functions are utilized since the turbulence closure in SIMRA is based on the standard $k - \epsilon$. This ensures that computational costs are reduced, and that computation efficiency is improved.

Following the forecasting capabilities of AROME, the coupled AROME-SIMRA technique allowed for the forecasting, nowcasting or hindcasting of mean turbulent quantities crucial for buffeting response research. As a result, AROME-SIMRA is a unique opportunity for turbulence study for buffeting response characterization pertinent to bridge structural dynamics in complex terrain. A numerical setup can be established for the instantaneous quantities that utilizes the flow simulation from the nested AROME-SIMRA simulation as the initial condition for a large eddy simulation utilizing either pure LES or Hybrid RANS-LES simulation.

References

[1] A. G. Davenport, The application of statistical concepts to the wind loading of structures., *Proceedings of the Institution of Civil Engineers*, 19:449–472 (1961).

[2] A. G. Davenport, The response of slender, line-like structures to a gusty wind., *Proceedings of the Institution of Civil Engineers*, 23:389–408 (1962).

[3] R. H. Scanlan, The action of flexible bridges under wind, II: Buffeting theory, *Journal of Sound and Vibration*, 60:201–211 (1978).

[4] E. Cheynet, Wind-induced vibrations of a suspension bridge: A case study in full-scale, PhD dissertation, Department of Mechanical and Structural Engineering and Materials Science (2016).

[5] A. Fenerci, Full-scale investigation of the effects of wind turbulence characteristics on dynamic behavior of long-span cable-supported bridges in complex terrain, PhD dissertation, Department of Structural Engineering, Norwegian University of Science and Technology (2017).

[6] P. H. Wirsching, T. L. Paez, K. Ortiz, *Random vibrations: theory and practice*, Courier Corporation, 2006.

[7] E. Cheynet, J. B. Jakobsen, J. Snæbjörnsson, Flow distortion recorded by sonic anemometers on a long-span bridge: Towards a better modelling of the dynamic wind load in full-scale, *Journal of Sound and Vibration*, 450:214–230 (2019).

[8] S. B. Pope, S. B. Pope, *Turbulent flows*, Cambridge university press, 2000.

[9] A. N. Kolmogorov, The local structure of turbulence in incompressible viscous fluid for very large reynolds numbers, *Proceedings of the USSR Academy of Sciences*, 30:299–303 (1941).

[10] J. Jiménez, The contributions of an kolmogorov to the theory of turbulence, *Arbor*, 178:589–606 (2004).

[11] J. C. Kaimal, J. J. Finnigan, *Atmospheric Boundary Layer Flows: Their Structure and Measurement*, Oxford University Press, 1994.

[12] J. C. Kaimal, J. C. Wyngaard, Y. Izumi, O. R. Coté, Spectral characteristics of surface-layer turbulence, *Quarterly Journal of the Royal Meteorological Society*, 98:563–589 (1972).

[13] N. E. Busch, H. A. Panofsky, Recent spectra of atmospheric turbulence, *Quarterly Journal of the Royal Meteorological Society*, 94:132–148 (1968).

[14] H. W. Tieleman, Universality of velocity spectra, *Journal of Wind Engineering and Industrial Aerodynamics*, 56:55–69 (1995).

[15] J. L. Lumley, H. A. Panofsky, *The structure of atmospheric turbulence*, vol. 12, Interscience publishers New York, 1964.

[16] Y. Cao, H. Xiang, Y. Zhou, Simulation of stochastic wind velocity field on long-span bridges, *Journal of Engineering Mechanics*, 126:1–6 (2000).

[17] Z. Xu, H. Wang, H. Zhang, K. Zhao, H. Gao, Q. Zhu, Non-stationary turbulent wind field simulation of long-span bridges using the updated non-negative matrix factorization-based spectral representation method, *Applied Sciences*, 9:5506 (2019).

[18] H. Wang, Z. Xu, D. Feng, T. Tao, Non-stationary turbulent wind field simulation of bridge deck using non-negative matrix factorization, *Journal of Wind Engineering and Industrial Aerodynamics*, 188:235–246 (2019).

[19] A. S. Monin, A. M. Obukhov, Basic laws of turbulent mixing in the surface layer of the atmosphere, *Proceedings of the Geophysical Institute USSR Academy of Sciences*, 24:163–187 (1954).

[20] R. O. Weber, Remarks on the definition and estimation of friction velocity, *Boundary-Layer Meteorology*, 93:197–209 (1999).

[21] I. Stiperski, M. W. Rotach, On the Measurement of Turbulence Over Complex Mountainous Terrain, *Boundary-Layer Meteorology*, 159:97–121 (2016).

[22] A. Golzio, I. M. Bollati, S. Ferrarese, An assessment of coordinate rotation methods in sonic anemometer measurements of turbulent fluxes over complex mountainous terrain, *Atmosphere*, 10:324 (2019).

[23] L. Kristensen, N. O. Jensen, Lateral coherence in isotropic turbulence and in the natural wind, *Boundary-Layer Meteorology*, 17:353–373 (1979).

[24] C. Klipp, Turbulent friction velocity calculated from the Reynolds stress Tensor, *Journal of the Atmospheric Sciences*, 75:1029–1043 (2018).

[25] Z. Midjiyawa, E. Cheynet, J. Reuder, H. Ágústsson, T. Kvamsdal, Potential and challenges of wind measurements using met-masts in complex topography for bridge design: Part ii–spectral flow characteristics, *Journal of Wind Engineering and Industrial Aerodynamics*, 211:104585 (2021).

[26] A. G. Davenport, The spectrum of horizontal gustiness near the ground in high winds, *Quarterly Journal of the Royal Meteorological Society*, 87:194–211 (1961).

[27] EN 1991-1-4, Eurocode 1. Actions on structures – Part 1-4: General actions – Wind actions., Tech. rep., [Authority: The European Union Per Regulation 305/2011, Directive 98/34/EC, Directive 2004/18/EC] (2005).

[28] Norwegian Public Road Administration, *N400 Handbook for Bridge Design*, Directorate of Public Roads (2015).

[29] A. J. Bowen, R. G. Flay, H. A. Panofsky, Vertical coherence and phase delay between wind components in strong winds below 20 m, *Boundary-Layer Meteorology*, 26:313–324 (1983).

[30] L. Davidson, Fluid mechanics, turbulent flow and turbulence modeling (2017).

[31] H. K. Versteeg, W. Malalasekera, *An introduction to computational fluid dynamics: the finite volume method*, Pearson education, 2007.

[32] J. M. McDonough, Introductory lectures on turbulence (2007).

[33] J. Scheffel, On analytical solution of the navier-stokes equations (2001).

[34] P. Moin, K. Mahesh, Direct numerical simulation: a tool in turbulence research, *Annual review of fluid mechanics*, 30:539–578 (1998).

[35] J. Boussinesq, *Théorie de l'écoulement tourbillonnant et tumultueux des liquides dans les lits rectilignes a grande section*, vol. 1, Gauthier-Villars, 1897.

[36] A. A. Shirgaonkar, S. K. Lele, On the extension of the boussinesq approximation for inertia dominated flows, *Physics of Fluids*, 18:066601 (2006).

[37] B. Perot, P. Moin, A new approach to turbulence modeling, in *Proceedings of the Summer Program*, Citeseer, 1996, p. 1.

[38] N. Jiang, W. Layton, M. McLaughlin, Y. Rong, H. Zhao, On the foundations of eddy viscosity models of turbulence, *Fluids*, 5:167 (2020).

[39] J. Boussinesq, Essai sur la thèorie des eaux courantes [essay on the theory of flowing waters], *Mem Acadèmie des Sciences*, 23:252–260 (1877).

[40] F. G. Schmitt, About boussinesq's turbulent viscosity hypothesis: historical remarks and a direct evaluation of its validity, *Comptes Rendus Mécanique*, 335:617–627 (2007).

[41] J. M. Franco, P. Partal, The newtonian fluid, *Rheology*, 1:74–95 (2010).

[42] N. G. Wright, G. Easom, Non-linear k–ε turbulence model results for flow over a building at full-scale, *Applied Mathematical Modelling*, 27:1013–1033 (2003).

[43] K. Suga, K. Abe, Nonlinear eddy viscosity modelling for turbulence and heat transfer near wall and shear-free boundaries, *International journal of heat and fluid flow*, 21:37–48 (2000).

[44] P. A. Durbin, Separated flow computations with the k-epsilon-v-squared model, *AIAA journal*, 33:659–664 (1995).

[45] D. Laurence, J. Uribe, S. Utyuzhnikov, A robust formulation of the v2-f model, *Flow, Turbulence and Combustion*, 73:169–185 (2005).

[46] L. Prandtl, 7. bericht über untersuchungen zur ausgebildeten turbulenz, *ZAMM-Journal of Applied Mathematics and Mechanics/Zeitschrift für Angewandte Mathematik und Mechanik*, 5:136–139 (1925).

[47] E. R. Van Driest, On turbulent flow near a wall, *Journal of the aeronautical sciences*, 23:1007–1011 (1956).

[48] F. H. Clauser, The turbulent boundary layer, in *Advances in applied mechanics*, vol. 4, Elsevier, 1956, pp. 1–51.

[49] P. Klebanoff, Characteristics of turbulence in a boundary layer with zero pressure gradient, Tech. rep., National bureau of standards, Gaithersburg MD (1955).

[50] T. Cebeci, *Analysis of turbulent boundary layers*, Elsevier, 2012.

[51] M. Escudier, The distribution of the mixing length in turbulent flows near walls. rept, Tech. rep., TWF/TN/I, Imperial College, London (1965).

[52] P. Spalart, S. Allmaras, A one-equation turbulence model for aerodynamic flows, in *30th aerospace sciences meeting and exhibit*, 1992, p. 439.

[53] J. Gatsis, Investigating the spalart-allmaras turbulence model, *NASA* (2000).

[54] A. Narjisse, K. Abdellatif, Assessment of rans turbulence closure models for predicting airflow in neutral abl over hilly terrain, *International Review of Applied Sciences and Engineering* (2021).

[55] B. Baldwin, T. Barth, A one-equation turbulence transport model for high reynolds number wall-bounded flows, in *29th aerospace sciences meeting*, 1991, p. 610.

[56] M. Rahman, T. Siikonen, R. Agarwal, Improved low-reynolds-number one-equation turbulence model, *AIAA journal*, 49:735–747 (2011).

[57] X. Zhang, R. K. Agarwal, Applications of a des model based on wray-agarwal turbulence model with rotation and curvature correction, in *AIAA Scitech 2019 Forum*, 2019, p. 0082.

[58] S. Shuai, R. K. Agarwal, A new improved one-equation turbulence model based on k-kl closure, in *AIAA Scitech 2020 Forum*, 2020, p. 1075.

[59] E. Cheynet, S. Liu, M. C. Ong, J. B. Jakobsen, J. Snæbjörnsson, I. Gatin, The influence of terrain on the mean wind flow characteristics in a fjord, *Journal of Wind Engineering and Industrial Aerodynamics*, 205:104331 (2020).

[60] R. H. Nichols, Turbulence models and their application to complex flows.

[61] B. Launder, D. Spalding, The numerical computation of turbulent flows, *Computer Methods in Applied Mechanics and Engineering*, 3:269 – 289 (1974).

[62] S. Poroseva, G. Iaccarino, Simulation of separated flows with the k-epsilon model, in *APS Division of Fluid Dynamics Meeting Abstracts*, vol. 54, 2001, pp. EE–007.

[63] Q. Hou, Z. Zou, Comparison between standard and renormalization group k-ε models in numerical simulation of swirling flow tundish, *ISIJ international*, 45:325–330 (2005).

[64] M. Balogh, A. Parente, C. Benocci, Rans simulation of abl flow over complex terrains applying an enhanced k-ε model and wall function formulation: Implementation and comparison for fluent and openfoam, *Journal of Wind Engineering and Industrial Aerodynamics*, 104:360–368 (2012).

[65] V. Yakhot, S. Orszag, S. Thangam, T. Gatski, C. Speziale, Development of turbulence models for shear flows by a double expansion technique, *Physics of Fluids A: Fluid Dynamics*, 4:1510–1520 (1992).

[66] T.-H. Shih, W. W. Liou, A. Shabbir, Z. Yang, J. Zhu, A new k- eddy viscosity model for high reynolds number turbulent flows, *Computers & fluids*, 24:227–238 (1995).

[67] W. Reynolds, Fundamentals of turbulence for turbulence modeling and simulation, Tech. rep., Stanford Univ Ca Dept of Mechanical Engineering (1987).

[68] T.-H. Shih, G. Zhu, J. L. Lumley, *A new Reynolds stress algebraic equation model*, vol. 106644, Lewis Research Center, 1994.

[69] J. Bredberg, On the wall boundary condition for turbulence models (2000).

[70] K.-Y. Chien, Predictions of channel and boundary-layer flows with a low-reynolds-number turbulence model, *AIAA journal*, 20:33–38 (1982).

[71] B. E. Launder, B. I. Sharma, Application of the energy-dissipation model of turbulence to the calculation of flow near a spinning disc, *Letters in heat and mass transfer*, 1:131–137 (1974).

[72] V. C. Patel, W. Rodi, G. Scheuerer, Turbulence models for near-wall and low reynolds number flows-a review, *AIAA journal*, 23:1308–1319 (1985).

[73] Y. Nagano, M. Tagawa, An improved k-ε model for boundary layer flows (1990).

[74] P. Grover, A. F. da Silva, Application of rough-wall corrections for the k-ω sst model for the simulation of flow over fluvial dunes, in *8th International Conference on Fluvial Hydraulics, St. Louis University*, 2016, pp. 1092–1097.

[75] G. Kalitzin, G. Medic, G. Iaccarino, P. Durbin, Near-wall behavior of rans turbulence models and implications for wall functions, *Journal of Computational Physics*, 204:265–291 (2005).

[76] F. Liu, A thorough description of how wall functions are implemented in openfoam, *Proceedings of CFD with OpenSource Software*, pp. 1–33 (2016).

[77] D. C. Wilcox, Reassessment of the scale-determining equation for advanced turbulence models, *AIAA journal*, 26:1299–1310 (1988).

[78] D. Wilcox, Turbulence modeling for cfd, isbn 1-928729-10-x (2004).

[79] F. Menter, Zonal two equation kw turbulence models for aerodynamic flows, in *23rd fluid dynamics, plasmadynamics, and lasers conference*, 1993, p. 2906.

[80] F. R. Menter, Two-equation eddy-viscosity turbulence models for engineering applications, *AIAA journal*, 32:1598–1605 (1994).

[81] J. Smagorinsky, General circulation experiments with the primitive equations: I. the basic experiment, *Monthly weather review*, 91:99–164 (1963).

[82] J. W. Deardorff, Stratocumulus-capped mixed layers derived from a three-dimensional model, *Boundary-Layer Meteorology*, 18:495–527 (1980).

[83] B. Maronga, M. Gryschka, R. Heinze, F. Hoffmann, F. Kanani-Sühring, M. Keck, K. Ketelsen, M. O. Letzel, M. Sühring, S. Raasch, The parallelized large-eddy simulation model (palm) version 4.0 for atmospheric and oceanic

flows: model formulation, recent developments, and future perspectives, *Geoscientific Model Development*, 8:2515–2551 (2015).

[84] M. Germano, U. Piomelli, P. Moin, W. H. Cabot, A dynamic subgrid-scale eddy viscosity model, *Physics of Fluids A*, 3:1760–1765 (1991).

[85] D. K. Lilly, A proposed modification of the germano subgrid-scale closure method, *Physics of Fluids A: Fluid Dynamics*, 4:633–635 (1992).

[86] J. Bardina, J. H. Ferziger, W. C. Reynolds, Improved subgrid-scale models for large-eddy simulation., AIAA, 1980.

[87] J. Berg, N. Troldborg, R. Menke, E. Patton, P. Sullivan, J. Mann, N. Sørensen, Flow in complex terrain-a large eddy simulation comparison study, in *Journal of Physics: Conference Series*, vol. 1037, IOP Publishing, 2018, p. 072015.

[88] A. Stieren, R. J. A. M. Stevens, Evaluating wind farm wakes in large eddy simulations and engineering models, *Journal of Physics: Conference Series*, 1934:012018 (2021).

[89] P. Spalart, Comments on the feasibility of les for wings, and on hybrid rans/les approach, advances in dns/les, in *Proceedings of 1st AFOSR International Conference on DNS/LES, 1997*, 1997.

[90] M. S. Gritskevich, A. V. Garbaruk, J. Schütze, F. R. Menter, Development of ddes and iddes formulations for the k-ω shear stress transport model, *Flow, turbulence and combustion*, 88:431–449 (2012).

[91] A. Bechmann, Large-eddy simulation of atmospheric flow over complex terrain (2006).

[92] P. Richards, R. Hoxey, Appropriate boundary conditions for computational wind engineering models using the k–ϵ turbulence model, *Journal of wind engineering and industrial aerodynamics*, 46:145–153 (1993).

[93] D. Hargreaves, N. G. Wright, On the use of the k–ϵ model in commercial cfd software to model the neutral atmospheric boundary layer, *Journal of wind engineering and industrial aerodynamics*, 95:355–369 (2007).

[94] B. Blocken, T. Stathopoulos, J. Carmeliet, Cfd simulation of the atmospheric boundary layer: wall function problems, *Atmospheric environment*, 41:238–252 (2007).

[95] Y. Yang, M. Gu, S. Chen, X. Jin, New inflow boundary conditions for modelling the neutral equilibrium atmospheric boundary layer in computational wind engineering, *Journal of Wind Engineering and Industrial Aerodynamics*, 97:88–95 (2009).

[96] Y. Yang, Z. Xie, M. Gu, Consistent inflow boundary conditions for modelling the neutral equilibrium atmospheric boundary layer for the sst k-ω model, *Wind & structures*, 24:465–480 (2017).

[97] M. Cindori, F. Juretić, H. Kozmar, I. Džijan, Steady rans model of the homogeneous atmospheric boundary layer, *Journal of Wind Engineering and Industrial Aerodynamics*, 173:289–301 (2018).

[98] A. Rasheed, K. Sørli, A multiscale turbulence prediction and alert system for airports in hilly regions, in *2014 IEEE Aerospace Conference*, IEEE, 2014, pp. 1–10.

[99] Y. Seity, P. Brousseau, S. Malardel, G. Hello, P. Bénard, F. Bouttier, C. Lac, V. Masson, The arome-france convective-scale operational model, *Monthly Weather Review*, 139:976–991 (2011).

[100] M. Müller, M. Homleid, K.-I. Ivarsson, M. A. Køltzow, M. Lindskog, K. H. Midtbø, U. Andrae, T. Aspelien, L. Berggren, D. Bjørge, et al., Arome-metcoop: A nordic convective-scale operational weather prediction model, *Weather and Forecasting*, 32:609–627 (2017).

Summary

Summary of papers

1. Summary of Paper I

1.1. *Paper I: Potential and challenges of wind measurements using met-masts in complex topography for bridge design: Part I – Integral flow characteristics*

The first paper investigates the deviations of the mean and turbulent flow characteristics from the traditional case of flat and homogeneous terrain. Two years of measurements are analyzed, using data from 25 three-dimensional sonic anemometers mounted at heights from 12 m to 95 m above the ground. The data are decimated from 20 to 10 hz and organized into 30 mn segments. Records below 12 m/s are eliminated prior to analysis due to the importance of higher wind speed in buffeting response study. The anemometer tilt is corrected using a double rotation approach. Linear trends, non-physical signals, non-stationary samples, and signals with substantial statistical uncertainty are all eliminated.

The key results are:

1. Wind measurement on the shores of fjords on Norway's west coast is characterized by a high incidence angle and sector-dependent turbulence intensity.
2. Deviations from Gaussian flow assumptions was examined using the skewness and excess coefficient. High values of skewness and excess coefficient were obtained specially on the vertical velocity component. This suggest that non-Gaussianity is a common characteristic of the recorded wind at the various locations. Furthermore, the findings show that, a horizontal flow does not imply a Gaussian fluctuation on the shore of fjords.
3. The normalized standard deviation of the velocity fluctuations was examined for all the wind records. σ_u, σ_v, and σ_w are the standard deviation of the along wind, cross wind, and vertical velocity fluctuations, respectively. the values of σ_w/σ_u and σ_v/σ_u significantly differ from the recommended ones in the Norwegian handbook of bridge design (N400). Furthermore, the ratio

of the vertical standard deviation to the friction velocity clearly shows sector dependence on the shore of fjords.

4. The friction velocity, an important scaling parameter in the surface layer, is estimated using different approaches. The results reveal that the different methods agree with each other depending on the influence of topography on the momentum fluxes. In general, it was found that the momentum fluxes $u'v'$ and $v'w'$ on the shore of fjords are significantly different from zero.

2. Summary of Paper II

2.1. ***Paper II: Potential and challenges of wind measurements using met-masts in complex topography for bridge design: Part II – Integral flow characteristics***

The second paper examines turbulence's spectral characteristics. In the fjords' shores, velocity spectra and coherence are investigated in relation to various upstream fetches. The spectra and coherence are compared to the literature-available flat terrain counterpart. The study's main finding is that upstream fetch may be used to categorize spectral characteristics on the shores of fjords. These are divided into two categories: long fetch over smooth topography and rough heterogeneous terrain upstream of the masts.

The key results are:

1. Surface-layer scaling maybe applicable in Norwegian fjords, at least under near-neutral conditions, if the velocity spectra are normalized by an appropriate estimate of the friction velocity.

2. The dynamic wind-induced response of long-span bridges is governed by the low-frequency turbulent wind fluctuations. Therefore, the study of power spectra, showed that, for long-fetch winds, the power spectral density of the along and cross winds have higher amplitude at low-frequency compared to the short fetch counterpart. For the vertical spectra, however, the upstream characteristic has no meaningful influence on the low-frequency section.

3. The vertical spectra follow surface-layer scaling as they superpose on each other at $fr < 0.1$ for both short-fetch and long-fetch winds. In comparison to horizontal components, vertical spectra have a spectral peak located at higher frequency. This agrees with flat terrain characteristic.

4. In the fjords studied, spectral plateau and double spectral peak are prominent features of turbulence spectra mainly on long-fetch winds. The study did not link the double spectral peak and spectral plateau with topographic feature

as these have been observed in previous study of turbulence in offshore environment. The use of semi-empirical spectrum of turbulence, in the design of bridges, should be reassessed in the design of long span bridge as these do not usually account for double spectral peak and spectral plateau.

5. The real and imaginary part of the cross-spectrum called co-spectrum and quad-spectrum are of similar magnitude. Compared to flat terrain, the quad-spectrum is significantly high. Terrain roughness classification can possibly be studied using the quad-spectrum.

6. The co-coherence is modelled in wind engineering as an exponentially decaying function ($\gamma_i(z_1, z_2, f) = \exp(-C^i f_D)$). C^i is the so-called Davenport decay coefficient. The vertical decay coefficient was estimated for all the met-mast. The vertical decay coefficient's average values are found to be compatible with the values provided in the handbook of bridge design (N400). In addition, the Davenport decay coefficients do not differ considerably depending on the upstream fetch characteristics.

7. The co-coherences, when expressed as a function of f_D ($f_D = f\varDelta z/\bar{u}(z_1, z_2)$) should collapse to a single curve. The calculated vertical co-coherences do not collapse to a single curve, as expected by Davenport's co-coherence model. Vertical co-coherence estimates at various locations demonstrate a reasonable agreement with models of co-coherence that include the dependency on height and separation distance.

3. Summary of Paper III

3.1. ***Paper III: Nested computational fluid dynamic modelling of mean turbulent quantities estimation in complex topography using AROME-SIMRA***

The conclusion acquired from point measurement cannot be extrapolated along the bridge span. As a result, numerical simulations are performed to compensate for the lack of measurement along the fjord's width. Validation is the initial stage in using numerical simulation. The validation of AROME-SIMRA, a nested macroscale-microscale computational fluid dynamic model, is the subject of the third study. The correlation coefficient between simulation and measurements is calculated as part of the validation process.

The key results are:

1. In complex topography, the use of a nested mesoscale-microscale model outperforms using a macroscale model alone.

2. The wind speed and direction were found to be in reasonable agreement with observation on the fjord shores. Except in region considerably sheltered by the topography.
3. The angle of attack, on the other hand, is determined by the mast location, incoming wind, and anemometer height.
4. Along the fjord span, the flow is largely undisturbed and horizontal depending on the upstream fetch topographic characteristics and inlet flow direction.

Perspective

Perspective and outlook

In the context of bridge design, the study in this thesis provided insight into the validity of the general assumption utilized in turbulence characterization.

The effects of the wind sector on flow horizontality, Gaussianity, turbulence intensity, and momentum fluxes were studied. Furthermore, the along wind spectra, cross wind spectra, vertical wind spectra, cross spectra, and coherence of turbulence have been explored with respect to wind direction and upstream characteristics. The influence of topography on turbulence characteristics on the shores of fjords has been quantified, and similarities and differences with cases of flat and homogeneous terrain have been identified.

In addition to wind measurement analysis, the study has validated a numerical simulation tool used for analyzing flow conditions in regions with limited measurement.

Regardless of the study's findings. The results suggest that more research into turbulence analysis in complex terrain is needed. The following is a summary of the suggested future work:

- Buffeting response analysis for non-Gaussian and non-horizontal flow, which are common flow conditions in complex topography, should be investigated.

- An in-depth look at the effects of topography on momentum fluxes, which could help with friction velocity estimation in complex topography.

- A re-evaluation of the semi-empirical spectra, available in the literature and used in the buffeting responsible analysis, in order to include the effect of double spectral peak and spectral plateau.

- The computation of the joint-acceptance functions, which quantifies the contribution of the various co-coherence models on the modal load.

- A thorough investigation of the source of flow non-stationarity in the met-mast's location. Non-stationarity has a significant impact on turbulence parameters estimation, such as the integral length scale.

- Validation of a large eddy simulation CFD tool for analyzing turbulence spectra and coherence along a bridge span.
- In the context of complex topography, the domain extend in the range of 20 to 40 km. Therefore, hybrid RANS-LES such as the SST-$k-\omega$ IDDES (Improved delayed detached eddy simulation) may be used to soften the requirement of grid resolution while improving the prediction accuracy.

Paper I

Part I – Integral flow characteristics

Zakari Midjiyawa, Etienne Cheynet, Joachim Reuder, Hálfdán Ágústsson, and Trond Kvamsdal

Published in *Journal of Wind Engineering and Industrial Aerodynamic* (2021) **211**:104584

Potential and challenges of wind measurements using met-masts in complex topography for bridge design: Part I – Integral flow characteristics

Zakari Midjiyawa[1,2,*], Etienne Cheynet[3], Joachim Reuder[3], Hálfdán Ágústsson[4], Trond Kvamsdal[2]

[1] *Norwegian Meteorological Institute, Henrik Mohns Plass 1, 0313 Oslo, Norway*
[2] *Department of Mathematical Sciences, Norwegian University of Science and Technology, Alfred Getz' vei 1, 7491 Trondheim, Norway*
[3] *Geophysical Institute and Bergen Offshore Wind Centre, University of Bergen, Allegaten 70, 5007 Bergen, Norway*
[4] *Kjeller Vindteknikk, Norconsult AS, Tærudgata 16, Lillestrøm, Norway*

Abstract

The paper investigates the local topographic effect on the mean and integral flow characteristics recorded by sonic anemometers mounted on tall masts near the shoreline of three different Norwegian fjords. Two years of measurements are analysed, using data from 25 three-dimensional sonic anemometers mounted at heights from 12 m to 95 m above the ground. The goal is to explore the potential and challenges of using wind measurements from the masts located on the shores of the fjords in the design of planned bridge crossings. Therefore, the study explores the deviations of the mean and turbulent flow characteristics from the traditional case of flat and homogeneous terrain. Only records with mean wind speeds of $12\,\mathrm{m\,s^{-1}}$ and above at all elevations above the ground are considered due to their relevance in buffeting response, which led to the identification of a limited number of sectors representative of strong wind conditions. Mean incidence angles with absolute values above 6° and low mean wind shear are measured in several of the selected sectors. This highlights the major influence of the local terrain and vegetation around the masts on the wind conditions at the mast locations. Nevertheless, non-dimensional variance and covariance estimates of the velocity components are found to be consistent with values previously measured from bridge decks crossing narrow fjords. The paper explores also an alternative approach to compute the friction velocity, the estimation of which is challenging in a fjord-like topography. This first part of the paper focuses on integral flow characteristics, a second follow-on part will investigate in details which eddy wave-numbers are most affected by the local terrain, based on the analysis of the spectra of the velocity fluctuations.

---

1. Introduction

The topography of large parts of the Norwegian west coast is characterized by fjords, i.e. long, deep inlets of the sea, typically surrounded by steep mountainsides. The largest ones are several kilometres wide and reach up to 200 km inland. A few years ago, the Norwegian Public Road Administration (NPRA) started with the major infrastructure project Ferjefri E39, aiming to realize a 1000-km ferry-free highway route along the west coast of Norway [1]. The plans include several multi-kilometres fjord crossings by both bridges and tunnels.

The proposed bridges will be particularly sensitive to wind loading and the analysis of the flow conditions is therefore of crucial importance for their design [2, 3]. Among the different types of wind loading, those induced by turbulence, i.e. buffeting loads, are of major interest [4, 5]. The flow field over the fjord, in the vicinity of steep mountain slopes, will be strongly affected by topographic effects, such as channeling [6], downslope wind storms [7], and extreme gusts [8], e.g caused by turbulent eddies, either generated locally due to flow over or along complex terrain [9], or aloft in steep and possibly overturning gravity waves [10].

These fine-scale flow features challenge the identification of the flow characteristics used to model the wind load on slender structures such as long-span bridges. Earlier studies of relevance have been performed for the Saint-Nazaire bridge in western France [11, 12] for two distinctive winds directions with different upstream roughness, the Iroise cable-stayed bridge [4], also in western France, and the Stonecutters Bridge in Hong Kong [13, 14], to name a few. Detailed investigated bridges at the Norwegian west coast are the ones crossing the Lysefjord [5, 15], the Hardangerfjord [16–18] and the bridge connecting Bergen with the island of Sotra [19]. These studies are, however, very specific and focus on a single site. There exists only a limited number of studies discussing turbulence characterization from multiple Norwegian fjords [20, 21]. It is still an open question whether the wind conditions in fjords can be studied adequately by only using met-masts installed on the shore and if the wind flows in such locations share common turbulence characteristics. The present study uses wind measurements from eight masts in three different fjords, providing a unique opportunity to discuss this open question.

The paper aims at investigating the potential and limitations of using velocity data recorded on tall masts, located on the shore of fjords surrounded by steep mountains, for the computation of the dynamic wind load on long-span bridges. The fjords of interest in this work are Sulafjorden, Halsafjorden, and Julsundet. In each of them, two to four masts, each mast carrying three to four sonic anemometers, were installed on the seaside. The study, which is based on two years of wind measurements, is split into two parts. The first part, presented

---

[*] Corresponding author.

Email addresses: `midjiyawaz@met.no` (Z. Midjiyawa).

hereafter, focuses on assessing the influence of local topography on the mean flow and the integral turbulence characteristics. In particular, the mean incidence angle, the deviation from the assumption of Gaussian fluctuations, as well as the variance and covariances of the velocity components, are investigated. The so-called ”integral turbulence characteristics” represent here the characteristics that can be retrieved by integrating the spectral, and cross-power spectral densities of the velocity fluctuations over the frequencies. The second part, subject to a separate publication, investigates the influence of local topography on turbulence in the frequency space.

The present paper is organized as follows: Section 2 describes the topography surrounding the different met masts as well as the experimental setup. Section 3 summarises the data processing with focus on data reduction to isolate records relevant to bridge design. Section 4 quantifies the deviations of the flow characteristics from the assumptions of horizontal mean flow and Gaussian fluctuations. The impact of the local terrain on Reynolds stress tensor is also explored. Finally, Section 5 summarises the challenges associated with the measurement of turbulence close to mountainsides.

2. Measurement locations and observation setup

Figure 1 shows an overview of the topography at the fjords of interest, with markers indicating the position of the respective met-masts. The observation sites are located in the Møre and Romsdal county of western Norway; a mountainous region characterized by a large variability in surface roughness and land type (fig. 2).

Sulafjorden is more exposed to the open sea from its northwestern side, compared to Halsafjorden and Julsundet, which are located more inland with mountains on their east and west side. Sulafjorden is surrounded by mountains with heights up to 900 m. To the north and the south at SulaNW and SulaNE, the wind has a long fetch over open water. Towards the northwest and southeast at SulaNE, sectors associated with an onshore flow are typically characterized with high and variable roughness, due to a combination of steep and rough terrain as well as a varying vegetation cover.

Topography profiles across the relevant fjords, through the mast locations, are presented in fig. 3. All the masts are located near the shoreline, but local conditions dictate that many of them are located in steep terrain or on top of small headlands. Potential local topographic effects have, therefore, to be taken into account when analysing the observations [22].

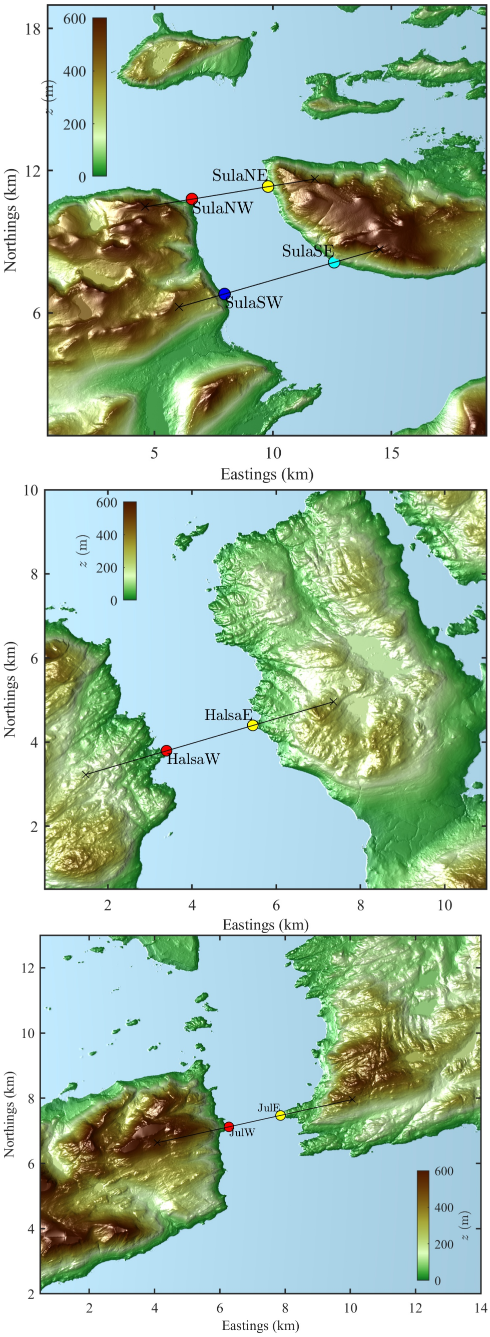

Figure 1: Digital terrain models with a horizontal resolution of 10 meters illustrating the location of the measurement masts and the surrounding topography for, from top to bottom, Sulafjorden, Halsafjorden and Julsundet.

Figure 2: Overview map showing the location of the three fjords under investigation in this study.

Since 2014, eleven met-masts have been installed on the seasides of Sulafjorden, Halsafjorden and Julsundet. Data from eight of these masts are explored in the present study. Two met-masts each were deployed on the western and eastern sides of Halsafjorden and Julsundet, in the following denoted as HalsaW/HalsaE and JulW/JulE, respectively (fig. 1). At Sulafjorden, four met masts were installed along two E-W transects, correspondingly labeled as SulaNW, SulaNE, SulaSW, and SulaSE (fig. 1). The distance between the two masts in each transect is approximately three and four kilometres, respectively.

A detailed description of the measurement setups, including instrumentation, sampling rate, local surface characteristics and topography is given in [23]. A summary is presented hereafter, for the sake of completeness. Five of the eight masts are lattice structures whereas the other three, at Julsundet and on the western shore of Halsafjorden, are guyed tubular masts (fig. 4). The coordinates, mast heights, boom orientation, measurement heights above the terrain, and observation periods are summarised in Table 1. The tubular masts are 250 mm to 300 mm in diameter, while the lattice towers horizontal dimensions vary from 60 mm to 2.6 m. Boom lengths and directions were chosen to minimize possible

Table 1: Overview of the met-masts: Mast acronym, mast location, mast height, mast type, sensor heights, boom orientation, boom length, and coordinate position. Reproduced from [23]

Mast acro.	Mast loc.	Mast h.(m)	Mast type	Sensor h. (m)	Boom orient. (Deg)	Boom l. (m)	Coord.(UTM32)
SulaNW	Kvitneset	100.5	Lattice	92.5, 71.5, 44.5	72, 74, 74	6.1	6924741 N, 345142 E
SulaNE	Trælbodneset	78.0	Lattice	76.8, 48.3, 27.3	289, 290, 290	6.1	6925267 N, 348347 E
SulaSW	Langeneset	97.0	Lattice	94.8, 75.0, 50.0, 27.0	81, 81, 81, 81	4.4	6920740 N, 346520 E
SulaSE	Kårsteinen	63.0	Lattice	62.8, 40.0, 13.4	223, 223, 223	3.6	6922074 N, 351140 E
HalsaW	Halsaneset	50	Tubular	50.3, 31.9, 12.7	106, 106, 104	1.8	6995095 N, 456472 E
HalsaE	Åkvik	50	Lattice	48.3, 31.9, 17.0	227, 227, 227	4	6995697 N, 458519 E
JulW	Nautneset	68	Lattice	68.3, 52.3, 32.7	239, 239, 239	5.1	6957381 N, 394634 E
JulE	Julbo	50	Tubular	50.3, 31.9, 12.7	234, 234, 234	1.8	6957730 N, 396210 E

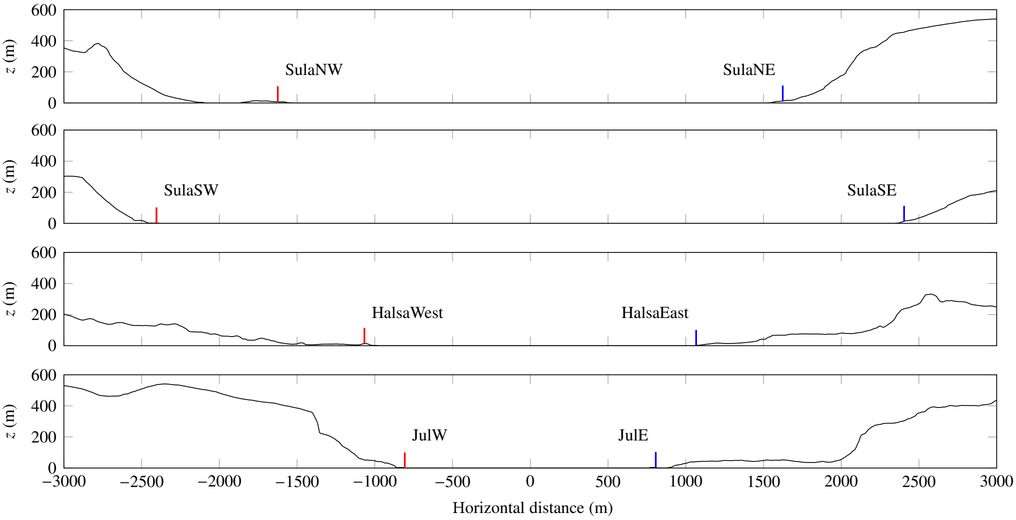

Figure 3: Overview of the mast positioning and height compared to surrounding topography

tower disturbances for the prevailing wind directions, estimated using numerical atmospheric simulations with the WRF model in a horizontal resolution of 500 m [24]. The velocity records from the masts show that wind directions perpendicular to the main fjord axes are relatively infrequent, and only a small amount of observations are associated with mast shadow. Each mast is instrumented with 3D sonic anemometers of the type Gill WindMaster Pro. Data were recorded by a Campbell CR 1000 logger and saved with a sampling frequency of 10 Hz. The measurements are quality checked, described and analysed in bi-annual technical reports, with the most recent ones being [25] and [26].

3. Theoretical background and data processing

3.1. Traditional assumptions in wind turbulence

The wind velocity is generally described as a tridimensional and trivariate random process in wind engineering and micro-meteorology. If the mean flow is horizontal, the along-wind, u, and cross-wind, v, components are also located in the horizontal plane. The vertical component is denoted by w. In flat terrain, the velocity components are studied in a Cartesian coordinate system $\{x, y, z\}$, where x, y and z are the along-wind, cross-wind and vertical directions, respectively. The cross-wind direction is sometimes also referred to as lateral direction to avoid any confusion with the vertical direction. In this context, u, v and w can be decomposed into a mean component, denoted by an overbar and a fluctuating

Figure 4: Examples of mast structures used. Rectangular lattice tower at Aakvik in Halsafjorden (upper left), Kvitneset in Sulafjorden (upper right), and Halsaneset in Halsafjorden (below), where one of the anemometer can also been seen. Photos: Kjeller Vindteknikk.

component, denoted by a prime

$$u = \overline{u} + u' \tag{1}$$

$$v = \overline{v} + v' \tag{2}$$

$$w = \overline{w} + w' \tag{3}$$

In the traditional description of atmospheric turbulence, u', v' and w' are stationary, ergodic, Gaussian random processes with a zero mean value. In particular, $\overline{v}$ and $\overline{w}$ are equal to zero, as the mean transport is assumed to occur along the mean wind direction only. Over gentle hills, the flow is no longer horizontal and $\overline{w} \neq 0$. If no flow separation occurs, the flow characteristics can be studied in the mean streamline coordinate system where $\overline{w}$ is zero, which is obtained after the rotation of the coordinate system $\{x, y, z\}$ [27]. In more complex terrains, there is no clear consensus on which coordinate transformation is best suited to study turbulence [28–30].

The assumption of Gaussian fluctuations implies that the description of wind turbulence can be limited to the second-order characteristics, i.e. variance and covariance of the velocity fluctuations. Variance and covariance estimate can be derived by integrating their auto and cross-power spectral density over the frequencies. This justifies the term integral turbulence characteristics used in the following. The variance and covariance of the velocity fluctuations, also called Reynolds stresses, can be represented by the symmetric Reynolds stress tensor.

$$R = \begin{bmatrix} \overline{u'u'} & \overline{u'v'} & \overline{u'w'} \\ \overline{u'v'} & \overline{v'v'} & \overline{v'w'} \\ \overline{u'w'} & \overline{v'w'} & \overline{w'w'} \end{bmatrix} \tag{4}$$

In flat and homogeneous terrain, it is generally assumed that the only non-zero off-diagonal term is $\overline{u'w'}$, i.e., the Reynolds stress is aligned with the horizontal mean wind vector. However, the term $\overline{v'w'}$ is not always negligible, e.g. above the ocean [31] or in complex terrain [32]. Similarly, on the sides of a fjord, the terms $\overline{u'v'}$ and $\overline{v'w'}$ may no longer be negligible compared to $\overline{u'w'}$, because the vicinity of the mountain slopes can be a source of additional shear stresses.

Deviations from the assumption of Gaussian flow may be observed on the shore of a fjord. Such deviations can be assessed using the skewness γ an excess kurtosis κ, which is defined as the kurtosis minus three. If the flow is Gaussian, both γ and κ are zero.

The time-average, used in the following, can be considered as equal to the true average if the assumption of ergodicity holds and if the time-averaging interval is long enough. Therefore, longer records will reduce the random error associated with the time-averaging operator. In the wind engineering community, the time-averaging interval is typically chosen to be 10 min or, more rarely, as one hour [33]. In the field of boundary layer meteorology, the time-averaging interval is typically in the range of half an hour to one hour [34]. One reason for this difference is that, in boundary layer meteorology, there is high interest in the momentum flux between the atmosphere and the surface, expressed by the covariance between the horizontal and vertical velocity components. Those fluxes require longer time-averaging intervals for sufficient accuracy compared to the variances [35]. Time-averaging intervals beyond one hour are seldom used as they are typically linked to non-stationary fluctuations, for which many of the tools used in descriptive statistics are no longer valid.

3.2. ***Friction velocity***

The friction velocity is the fundamental scaling velocity in the surface layer [35] and can conveniently replace the variance of the velocity components to model the dynamic wind load. However, the estimation of the friction velocity can be challenging in complex terrain. Following [36], the friction velocity can be estimated after the application of the double rotation technique as

$$u_* = \left[\left(\overline{u'w'} \right)^2 + \left(\overline{v'w'} \right)^2 \right]^{1/4} \tag{5}$$

Unless explicitly stated, u_* is computed in the following as in Eq. (5) because directional shear is expected to play a non-negligible role in complex terrain [37, 38]. If the horizontal shear stress $\overline{u'v'}$ is non-negligible, the friction velocity might be computed using the invariant of the Reynolds stress tensor [30, 39]. The method by [30] is an elegant approach to compute the friction velocity without using any tilt correction algorithm. Even though it was developed using a dataset collected in flat terrain, Klipp's method may become a valuable tool to study the friction velocity in complex terrain. Klipp's method is adapted to strong wind speeds and neutral atmospheric stratification. The method is summarized hereafter for the sake of completeness. First, the eigenvalue decomposition of the Reynolds stress tensor (Eq. (4)) is applied, leading to the three eigenvalues, i.e., principal components of the Reynolds stress tensor, $\lambda_1 > \lambda_2 > \lambda_3$ and their associated eigenvectors $\mathit{\Lambda}_1$, $\mathit{\Lambda}_2$, and $\mathit{\Lambda}_3$ (denoted $\mathit{\Lambda}_b$, $\mathit{\Lambda}_m$, and $\mathit{\Lambda}_s$ in [30]). Then, the friction velocity is computed as

$$u_{*_R} = \left[(\lambda_1 - \lambda_3) \cos(\beta) \sin(\beta) \right]^{1/2} \tag{6}$$

where β is the complement of the angle between the mean wind speed vector U and the vector $\mathit{\Lambda}_3$

$$\beta = 90 - \arccos\left(\frac{U \cdot \mathit{\Lambda}_3}{|U|\,|\mathit{\Lambda}_3|} \right) \tag{7}$$

The discrepancies between u_{*_R} and u_* are investigated in Section 4.5.

3.3. ***Data selection***

In the following, a subset of the complete dataset is used, i.e. observations of 2018 and 2019. The data are freely available for every met-mast [23, 40]. Further data-processing performed for this study is described below

- The anemometer records were grouped into time series of 30 minutes. This ensured that a sufficiently high number of turbulent eddies is included in the calculation of the turbulence characteristics. A 30-minute time-averaging is long enough to reduce the random error associated with the calculation of the Reynolds stress tensor but, at the same time, short enough to limit the number of non-stationary wind records.

- Samples with mean wind speed values lower than $12\,\mathrm{m\,s^{-1}}$ were removed. For bridge design purposes, the turbulence intensity (TI) of the along-wind component, denoted I_u, is independent on the mean wind speed [41]. Therefore, the same I_u is valid for a wide range of mean wind speeds. In full-scale, the TI is defined as $I_j = \sigma_j/u$, where $j = \{u, v, w\}$ and σ_j denotes the standard deviation of the fluctuating component j. The TI is inversely proportional to u, leading to overestimated TI values at low wind speed. Furthermore, the buffeting response analysis is generally done under neutral conditions [42], which are dominant under strong wind conditions [43–45]. In heterogeneous terrain, where multiple internal boundary layers exist, the atmospheric stability is preferably studied locally using sonic anemometer data and the eddy-covariance method. The sonic temperature data were stored by the sensor on each mast and available at a sampling frequency of 2 Hz. To obtain a reliable estimate of the temperature fluxes, a sampling frequency of at least 10 Hz and ideally 25 Hz is required [35]. Therefore, no reliable estimate of the Obukhov length could be obtained in the present case. This further motivates the dismissal of low-wind speed records.

- The double rotation technique was used to compensate for the tilt in the flow [46, 47], as sectorial planar fit may not be appropriate in terrains with steep slopes, such as on the west coast of Norway near the masts [30].

- Turbulence characteristics were analysed after the removal of linear trends. Trends come from low-frequency fluctuations not captured by the records due to their finite duration. Both linear and non-linear trends can lead to poorly estimated turbulence characteristics. To avoid over-processing of the data, only linear trends were removed in the following.

- Signals characterized by high skewness and kurtosis were removed. The maximum accepted value of skewness was set to 2 and of kurtosis to 8, following the suggestions by [29] and [48]. This step is called Gaussianity test in the following.

- Non-stationary samples were removed. The moving mean and standard deviation were calculated for every time series segment using a window length of 10 minutes. A maximum deviation of 20% is allowed for the moving mean and of 40% for the moving standard deviation [21].

- The statistical uncertainties in the momentum fluxes were calculated following [49] and [29], as

$$a_{uw}^2 = \frac{z}{\tau \bar{U}} \left[\frac{\overline{(u'w')^2}}{u_*^4} - 1 \right] \tag{8}$$

$$a_{vw}^2 = \frac{z}{\tau \bar{U}} \left[\frac{\overline{(v'w')^2}}{u_*^4} - 1 \right] \tag{9}$$

where τ and z are the length of the time series and the measurement height, respectively. A limit of 50% for the statistical uncertainty was chosen [29]. Eqs. (8) and (9) show that long record duration results in reducing uncertainties associated with the calculation of the momentum flux. A shorter time-averaging interval has the advantage of providing more time series for the analysis. However, reducing the averaging time increases both the random error and the measurement bias, both of which increases the statistical uncertainties.

4. Results

*4.1. **Data availability***

Table 2 shows the number and percentage ratio of available 30-min times series fulfilling the requirements for data analysis described in Section 3.3. For each met-mast, the available data are summed up for all the anemometers. This gives a general overview of the available data obtained after each filtering step.

The data processing filters out more than 90 % of the velocity records. The criterion causing the largest data reduction is the minimum mean wind speed threshold, which in the present case is $12\,\mathrm{m\,s^{-1}}$. The Norwegian fjords are typically sheltered by mountains, although, under certain conditions, flow acceleration may be locally observed. Nevertheless, it is unknown whether such speed-up events are commonly observed near the measurement sites. Although interesting, this topic is out of the scope of the present work.

The other criteria, namely the Gaussianity, statistical uncertainty, first and second-order stationarity are only filtering out a small portion of the remaining time series. After the filtering process, the highest amount of data is found to be

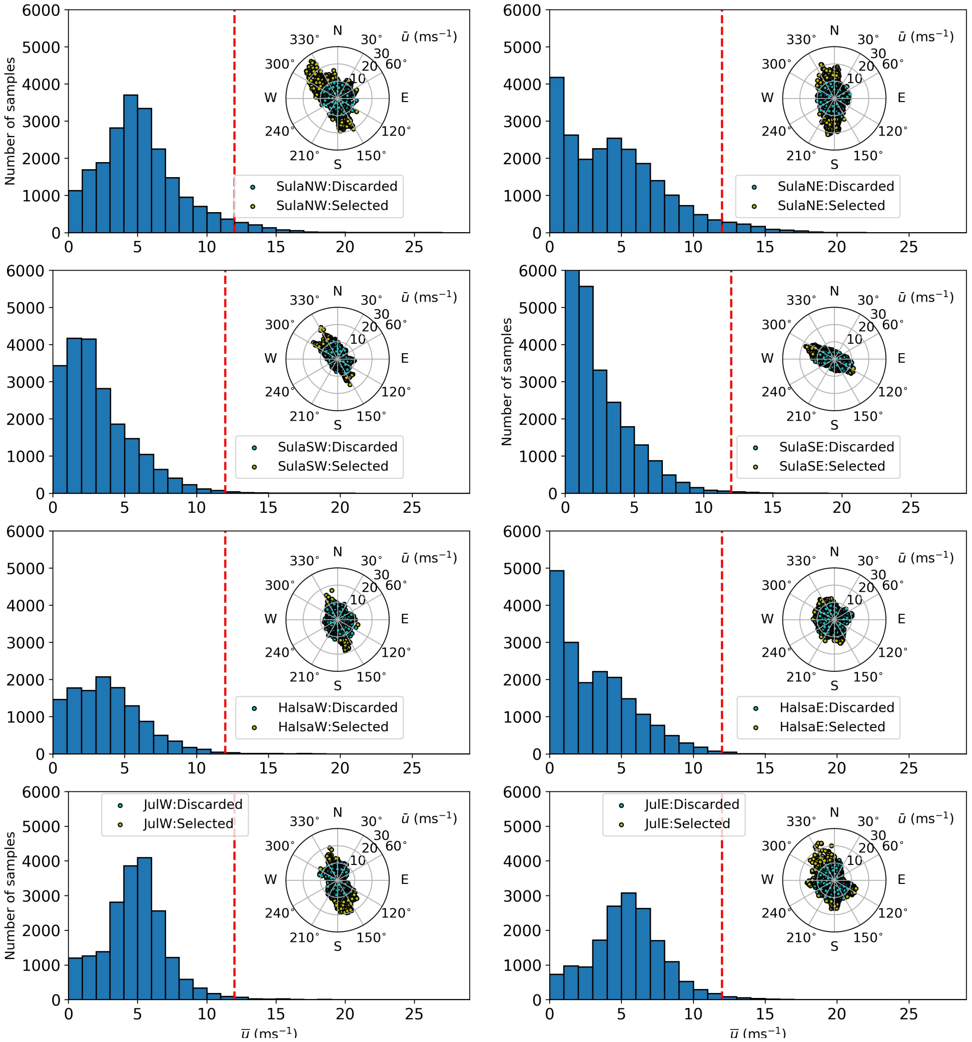

Figure 5: Histogram and wind roses of the 30min velocity records by the anemometer nearest to 50 m above ground level from the 01-01-2018 to 31-12-2019. The red dashed line shows the mean wind speed threshold ($\overline{u} \geqslant 12\,\mathrm{m\,s^{-1}}$) chosen in the data processing.

at SulaNW and SulaNE, which highlights the higher exposure of the northern side of Sulafjorden compared to the other locations studied here.

Figure 5 displays histograms of the wind speed, as well as the corresponding wind roses for the anemometer nearest to 50 m above the ground level. The distributions are in general, positively skewed with a maximum in the probability density of $6\,\mathrm{m\,s^{-1}}$ or below. Most of the sites show a clear deviation from a Weibull

Table 2: Cumulated absolute number N and relative number of samples, including those with $\overline{u} \geqslant 12\,\mathrm{m\,s^{-1}}$, those which passed the Gaussianity test, those with low statistical uncertainties test and those stationary up to the second order, for every met-mast from the 01-01-2018 to 31-12-2019. Note that the number of samples are summed for all available anemometers.

Mast		N	Above or equal to $12\,\mathrm{m\,s^{-1}}$	After Gauss. test	Low stat. uncert.	Stationary
SulaNW	Samples	65014	3890	3888	3445	2547
		100 %	5.98 %	5.98 %	5.30 %	3.92 %
SulaNE	Samples	67659	3351	3347	3089	2134
		100 %	4.95 %	4.95 %	4.57 %	3.15 %
SulaSW	Samples	82102	1258	1258	1214	831
		100 %	1.53 %	1.53 %	1.48 %	1.01 %
SulaSE	Samples	67862	616	616	607	338
		100 %	0.91 %	0.91 %	0.89 %	0.50 %
HalsaW	Samples	36696	764	758	723	537
		100 %	2.08 %	2.07 %	1.97 %	1.46 %
HalsaE	Samples	55651	738	737	724	547
		100 %	1.33 %	1.32 %	1.30 %	0.98 %
JulE	Samples	59215	1336	1329	1266	722
		100 %	2.26 %	2.24 %	2.14 %	1.22 %
JulE	Samples	50391	1455	1454	1377	832
		100 %	2.89 %	2.89 %	2.73 %	1.65 %

type distribution typically observed in open and flat terrain. One typical feature is the strong over-representation of low wind speeds, in particular, visible for SulaNE, SulaSE, and HalsaE, indicating a reduction of wind speed by the influence of terrain and surrounding vegetation. Furthermore, the uneven directional distribution of the flow channelled inside the fjord might also lead to a deviation from the Weibull distribution.

The wind roses show, for $\overline{u} \geqslant 12\,\mathrm{m\,s^{-1}}$, a limited number of directional sectors, emphasizing the channelling effect by the surrounding topography. These roses document also the complexity of the measurement setup by distinct and systematic differences across the different fjords and with different position inside the same fjord. For the three fjords investigated, the general flow pattern in 2018 and 2019 tends to be dominated by a wind from south and southeast to north and northwest. This is largely due to flow channelling caused by mountains on the east and west side of the respective fjords. At SulaNW and SulaNE, the most dominant wind directions correspond to a south-southeasterly and north-northwesterly flow. At SulaSE, the strongest winds come from the west-north-west whereas, at SulaSW, large velocities are recorded either for a north-westerly or southerly flow. The wind roses for Halsafjorden show that the flow is dominated by southerly winds at HalsaW while on the other side of the fjord, at HalsaE, there is a distinctly larger spread in the directional distribution. Also, the wind roses on both sides of Julsundet display clear discrepancies, with a southerly dominance of wind flow at JulW and a more homogeneous directional distribution for JulE.

As shown in figs. 1 and 2, the lower mean wind speed values observed at JulW and JulE may be linked to the orientation of the fjord with respect to the direction of the strongest wind, which is from west to north-west, and the proximity of the masts to the flank of the surrounding mountains. However, the middle part of Julsundet is still fairly exposed to northern wind blowing from the sea. Complementary studies using wind tunnel tests or computational fluid dynamic simulations may help to assess the vulnerability of Julsundet to strong northern wind, but these are beyond the scope of this study.

The detailed data analysis is done hereafter for the sectors associated with the strong wind conditions only, i.e. one to three specific sectors per mast and that is because the flow characteristics vary significantly with the wind direction.

4.2. ***Flow horizontality***

A major source of uncertainty in the design of a long-span bridge in complex terrain comes from the aerodynamic characteristics of the deck, which are functions of the incidence angle [2, 50]. Measuring incidence angles from in-situ sensors is also valuable to assess to what degree the terrain slopes affect the measurements by the sonic anemometers. Besides, strongly non-horizontal flows may be associated with flow separation phenomena, which challenge the traditional modelling of

Table 3: Incidence angle (IA): Location of met-mast, wind direction, median, 5^{th} and 95^{th} percentile. The results reported are given for the anemometer closest to 50 m above the ground.

Mast	Sector (°)	Median IA	5^{th} percentile	95^{th} percentile
SulaNW	135-165	-2.26	-3.60	-1.05
	165-185	-5.51	-6.77	-4.44
	300-330	3.45	2.54	4.34
SulaNE	300-20	1.59	-2.33	5.59
	150-210	5.11	2.60	6.99
SulaSW	135-165	-3.93	-6.63	-0.81
	285-315	-9.46	-11.21	-5.26
	315-345	0.92	-2.07	6.31
SulaSE	270-330	4.06	-0.61	7.80
HalsaW	150-180	3.53	2.54	4.26
	285-360	3.10	-3.39	8.63
HalsaE	150-180	3.54	2.52	4.41
	210-285	6.19	5.38	8.40
	300-360	7.70	5.70	8.46
JulW	120-195	3.15	0.06	5.68
	330-360	-0.41	-1.90	1.22
JulE	120-195	0.58	-0.71	1.59
	210-285	1.29	0.21	2.92
	300-360	3.79	3.18	4.70

atmospheric boundary-layer turbulence.

Figure 6 shows the mean incidence angle (IA) as a function of the wind direction while table 3 summarises the mean IA recorded in terms of median and percentile values. The met-masts at JulW and JulE show flow conditions closest to horizontality compared to Sulafjorden and Halsafjorden. This is presumably due to the long fjord-fetch at these masts and the exposed locations on low headlands protruding into the water. As observed in [51], the flow follows the terrain slopes: positive IA indicates positive slopes upwind of the sensor whereas a negative IA reflects negative slopes.

The median values for Sulafjorden and Halsafjorden, range from $-9.5°$ (SulaSW, sector 285°-315°) to $+7.7°$ (HalsaE, sector 300°-360°) while some sectors show an almost horizontal flow (JulW, sector 330°-360°). The large variability observed in table 3 reflects the diversity of the topographic elements around each mast.

At some of the stations, such as SulaNW or SulaSE, the wind roses indicate two different flow regimes within one relatively narrow sector. The local terrain around the masts is characterized by hills, trees, ridges or escarpments which have

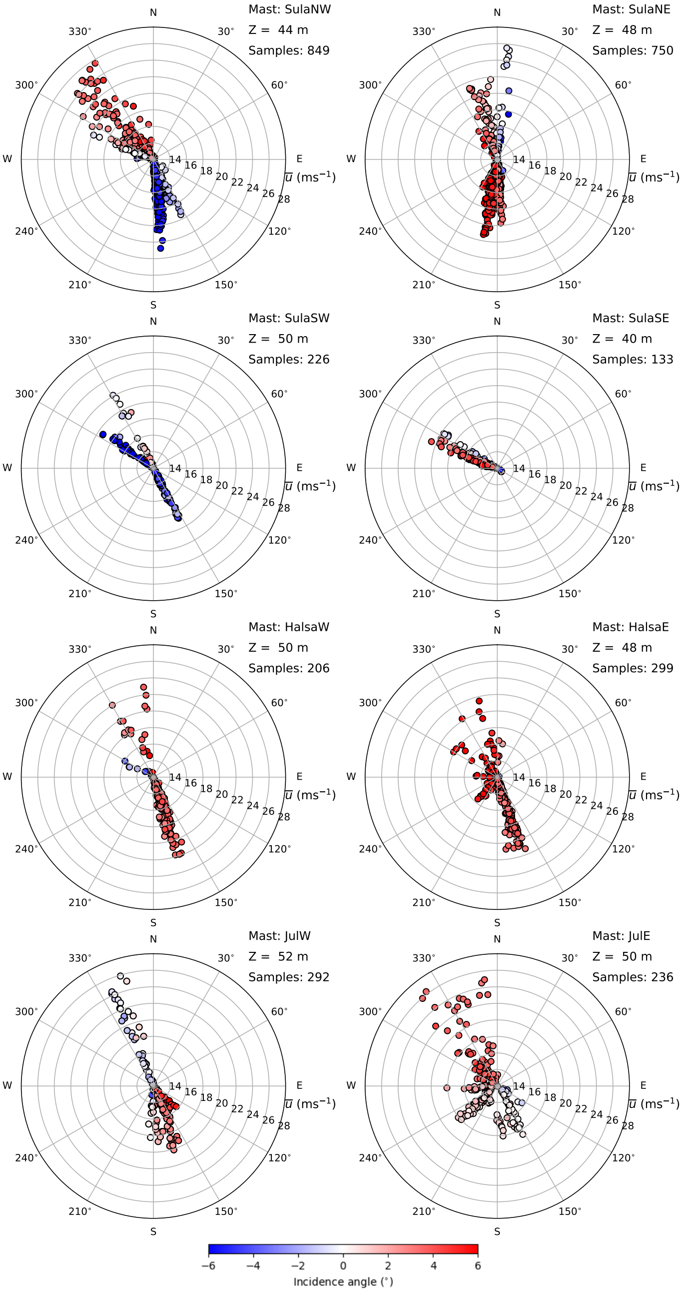

Figure 6: Wind roses showing the mean wind velocity ($\bar{u}$) and incidence angles (IA) recorded on the anemometers installed closest to 50 meters above the ground at Sulafjorden, Halsajorden and Julsundet for the period 01-01-2018 to 31-12-2019.

a three-dimensional effect on the flow and has likely a major influence on the abrupt change of flow conditions. At SulaSW, the mast is located downstream of a gentle hill and a ridge, when the wind direction is 150° and 180°, respectively. The slopes of the ridge are much steeper than the slope of the hill, resulting in strongly negative mean incidence angles with values below -4°. On the other hand, the wind blowing from 150° is associated with an incidence angle around -2° or lower at a height of 44 m above the surface. A similar situation is observed at SulaSW for the sector 300°-330°.

At SulaNE, the northern sector reflects an up-slope flow coming from the sea when the wind direction is 330°, whereas the wind direction around 0° is associated with a downslope flow brushing against the mountain's flank. Although a wind direction around 300° at SulaSE corresponds to a limited number of storms in 2018-2019, similar observations were done at lower wind speeds. The strongly positive incidence angles are likely due to the presence of an escarpment, ca. 110 m to the northwest to the mast, followed by a positive slope. The southern side of the escarpment is free from any vegetation and limited by the sea, whereas the northern side is covered by bushes and small trees. The larger turbulence intensity in Figure 7 at SulaSE for a wind direction slightly larger than 300° can be attributed to this vegetation, which locally increases the roughness length. [52] showed that a forest edge can also significantly affect the mean incidence angle. Therefore, it is possible that the nearly horizontal flow observed at SulaSE for a mean wind direction slightly above 300° is a consequence of the flow passing over the trees located on the northern side of the ridge.

At Sulafjorden and Halsafjorden, a mean absolute incident angle up to 9° is recorded (table 3), which is substantively larger than values reported from anemometers mounted above the deck of suspension bridges [21, 53]. [46] measured an incidence angle up to 7° on the Sotra bridge, but their measurements were affected by deck-induced flow distortion [21, 46]. Sonic anemometer measurements from masts installed in Bjørnafjorden [51] showed angles of attack that were also up to 6° at $u > 12\,\mathrm{m\,s^{-1}}$.

While the flow is expected to be more horizontal near the middle of the fjord than on its sides, the measured incidence angles are still valuable as they could be used to validate CFD models, which would aim to quantify the incidence angles along the deck of a fjord-crossing bridge. It should also be noted that a large incidence angle leads to a non-linear dynamic response that can be significant [54–56]. Therefore, overestimating the incidence angle is not desirable from a design perspective.

4.3. ***Mean wind shear***

The local terrain does not only affect the incidence angle but also the mean wind shear, which is quantified hereafter, for each selected sector, using the power-law

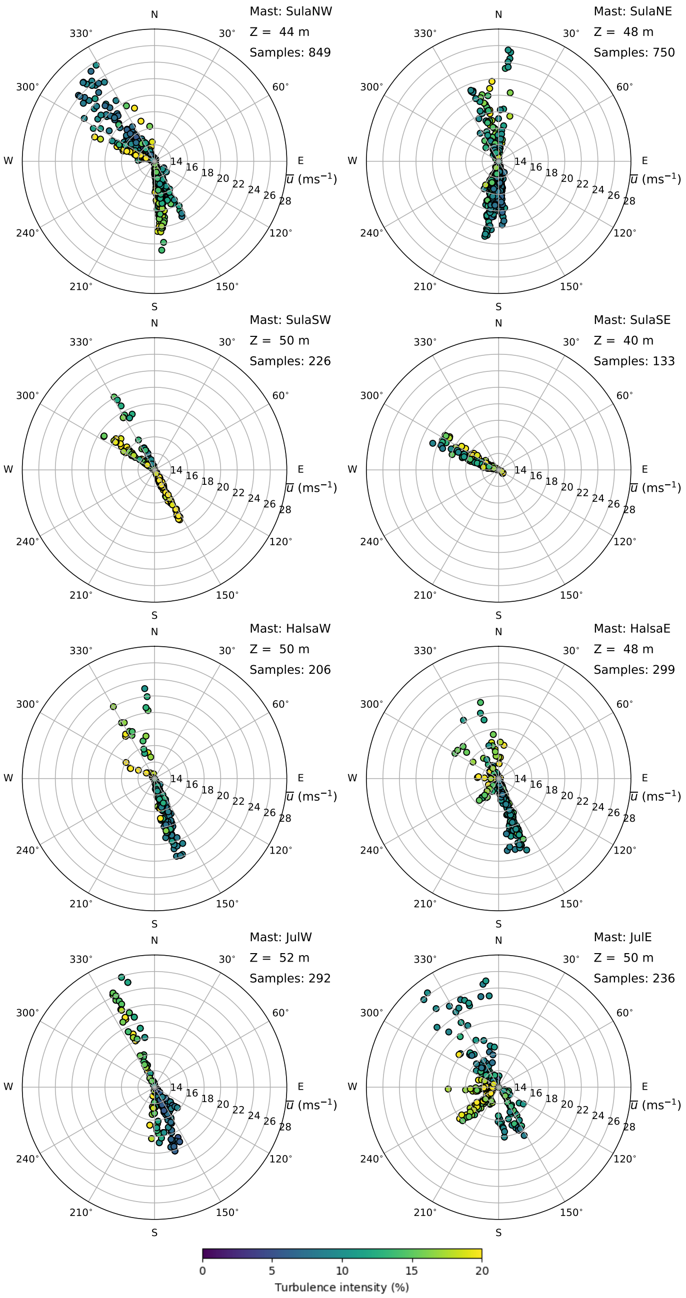

Figure 7: Wind roses showing the mean wind velocity ($\bar{u}$) and turbulence intensity (I_u) recorded on the anemometer installed closest to 50 m above the ground at Sulafjorden, Halsafjorden and Julsundet for the period 01-01-2018 to 31-12-2019.

coefficient [57] also called shear coefficient in the following. This coefficient is estimated by fitting the wind profile power law to the mean wind speed profile estimated on each mast using three or four sensors, when available. The power coefficient α is here used to supplement the incidence angle to describe the local topographic effects on the estimated flow characteristics. The calculated shear coefficients are shown in table 4, which includes the root mean square error between the fitted and measured mean wind speed values. Cases in which the wind speed at all elevations is lower than $12\,\mathrm{m\,s^{-1}}$ have been ignored which resulted in no computation of the shear coefficient for HalsaE as well as for the winds coming from the south at JulE.

The wind speed profile depends on the terrain and the thermal stratification of the atmosphere [58–60]. Selecting high wind speeds does not guarantee neutral stability conditions but reduces the occurrence of records characterized by a stable and unstable thermal stratification of the atmosphere. Thus, the shear coefficient for a given wind sector will mainly be determined by the local topography.

The shear coefficients are ensemble-averaged for each of the directional sectors selected. For every sector at SulaNW, SulaNE, HalsaW, JulW, and JulE, a small mean shear is obtained, with $\alpha \leqslant 0.09$. The largest shear coefficients are obtained at SulaSW and SulaSE with values of 0.12 and 0.15, respectively. The standard deviation associated with these shear coefficients shows that the α values found may not be significantly different in most of the masts and sectors considered. [61] reports an average shear coefficient of 0.11 for wind over the ocean, whereas [62] measured 0.10 for wind from sea and 0.20 to 0.30 for wind over land for wind speed between $12\,\mathrm{m\,s^{-1}}$ and $16\,\mathrm{m\,s^{-1}}$. The low values of the shear coefficients observed suggest possible speed-up of the flow by hills immediately upstream of the masts or at the mast location itself [22, 63]. Accordingly, the values $\alpha \geqslant 0.12$ observed at SulaSE and SulaSW are linked to the wind blowing over a long fetch above the sea with limited disturbance from the terrain upstream of the masts.

4.4. ***Flow Gaussianity***

The peak response of a structure to a non-Gaussian dynamic load can be much larger than in the case of a Gaussian distribution [64, 65]. Therefore, assessing the flow Gaussianity is valuable to model properly the extreme wind load [66]. Besides, if a random process is Gaussian, it can be described using the first two statistical moments only, which is attractive for modelling purposes.

For the sectors selected, fig. 8 shows that the along-wind component is generally Gaussian while it is not the case for the vertical component. However for the case of HalsaW sector 285°-360° and JulE sector 210°-285°, at measurement height located below 15 m above the ground and near the vegetation cover, the skewness of the along-wind component is considerable indicating non-Gaussian characteristics. Similar observations were done by [67, 68]. The skewness of the u component is

Table 4: Mean shear coefficient α and associated root-mean square value (RMSE), which were ensemble-averaged over N samples. Only wind velocity above $12\,\mathrm{m\,s^{-1}}$ at every height were considered. Data outside the 1^{st} and 99^{th} percentile were considered as outliers and removed.

Mast	Sector (°)	N	α	RMSE
SulaNW	135-165	125	0.02±0.04	0.0024±0.0028
	165-185	599	0.06±0.03	0.0034±0.0062
	300-330	275	0.02±0.03	0.0094±0.0163
SulaNE	330-20	203	0.04±0.03	0.0082±0.0131
	150-210	876	0.02±0.04	0.0132±0.0200
SulaSW	135-165	60	0.12±0.06	0.0150±0.0087
	285-315	40	0.08±0.03	0.0243±0.0085
	315-345	42	0.08±0.02	0.0142±0.0179
SulaSE	270-330	95	0.15±0.05	0.0312±0.0140
HalsaW	150-180	166	0.07±0.03	0.0029±0.0042
JulW	150-180	93	0.04±0.02	0.0111±0.0020
	330-360	84	0.08±0.03	0.0090±0.0034
JulE	210-270	60	0.09±0.05	0.0063±0.0066
	300-360	143	0.06±0.01	0.0067±0.0089

not expected to differ substantially between flat and complex terrain, whereas the excess coefficient may increase [38]. There are some few situations where the excess coefficient κ_u is significantly different from zero: At SulaSW for a wind direction between 135° and 165° and JulW for a wind direction between 330° and 360°. In both cases, the flow is associated with a slightly negative incidence angle (IA) with value down to $-2°$ and a wind direction almost parallel to the coast. This implies that multiple roughness changes are likely occurring, which could modify the distribution of the along-wind component u.

The distribution of the cross-wind component v is not always Gaussian and varies strongly with the sector selected. It can be noted that flow measurements at heights below 30 m in forested areas should be interpreted with care, as they may be affected by the vegetation. The cross-wind component v has an excess coefficient κ_v below 0.3 if the anemometers are not at the feet of a mountain and if the wind is blowing over a long fetch of water, for example at SulaNW, JulE, and HalsaE for a northwesterly flow and JulW for a northeasterly flow. In most of the other cases, the cross-wind component v has a non-negligible excess coefficient.

In the present case, a horizontal flow does not imply that the fluctuations are Gaussian. This is particularly visible for the vertical wind component w. At a height of 50 m above ground at SulaSW and JulW, the two sectors associated with a nearly horizontal flow correspond to a wind direction of ca. 330°. For both sectors, the excess coefficient of the vertical wind component w is above 0.7 whereas the skewness is close to zero. Sectors with IAs below $-4°$ (SulaNW, and SulaSW) shows the most Gaussian fluctuations for the vertical components with $\kappa_w < 0.5$ at most of the heights. Sectors with IAs above 4° (SulaNE, SulaSE, HalsaE, HalsaW, and JulW) shows in most of the cases $\kappa_w > 1$.

It cannot be deducted from the mast measurements on the seaside whether the vertical velocity component has a non-Gaussian distribution over the whole width of the fjord. Yet, this should be clarified as the vertical wind speed component governs the vertical and torsional buffeting response of long-span bridges.

4.5. ***Single point turbulence characteristics***

Turbulence intensity

The turbulence intensity here defined as the ratio of the standard deviation of the velocity component with mean wind speed is given in fig. 7, which shows the dependency of I_u on the wind direction for the different masts. The sector-averaged TI estimates, at various sensor heights, together with the corresponding standard deviations, are summarised in fig. 9. For sectors where the flow is relatively unaffected by the local terrain and has a long fetch over open water, e.g. the northwest of SulaNW and south of SulaNE, the average TIs ($I_u/I_v/I_w$) are 0.08/0.09/0.06 and 0.10/0.11/0.08, respectively. In Halsafjorden the average TIs for the southern sector of HalsaW and HalsaE are 0.10/0.09/0.05 and 0.11/0.10/0.06. At Julsundet, south of JulW, the TIs are 0.09/0.09/0.05 while the south and northwest of JulE the TIs are 0.11/0.11/0.07 and 0.10/0.10/0.05.

A turbulence intensity between 0.08 and 0.10 at a height of 50 m above ground is typically observed in coastal regions when the wind is blowing over a long fetch or offshore under strong wind conditions. In the Eurocode [41], if the turbulence factor and topography factor are both set equal to one, $I_u(z = 50\,\mathrm{m}) = 0.10$ corresponds to a terrain category 0, for which the roughness length z_0 is 0.003 m. It should be noted that the value $z_0 := 0.003\,\mathrm{m}$ is primarily used for the calculation of the design wind load, which is the reason it is much higher than the roughness length usually measured for calm sea, which is around 0.0002 m [69]. Interestingly, similar turbulence intensities were observed in Bjørnafjorden [51] and on the Sotra Bridge [46] for similar wind conditions and a long fetch, which confirms that turbulence characteristics in Norwegian fjords may share common features.

If the terrain upwind to the masts is more complex, e.g. for southerly flow at SulaNW, a southeasterly flow at SulaSW or a northwesterly flow at SulaSE, much higher TIs are measured. The corresponding values ($I_u/I_v/I_w$) are 0.16/0.13/0.16, 0.22/0.17/0.20 and 0.14/0.12/0.11 at SulaNW, SulaSW and SulaSE, respectively. Similarly, for the northwesterly sector of HalsaW, western sector of HalsaE, northwest of JulW and west of JulE, the TIs are 0.18/0.16/0.11, 0.17/0.15/0.10,

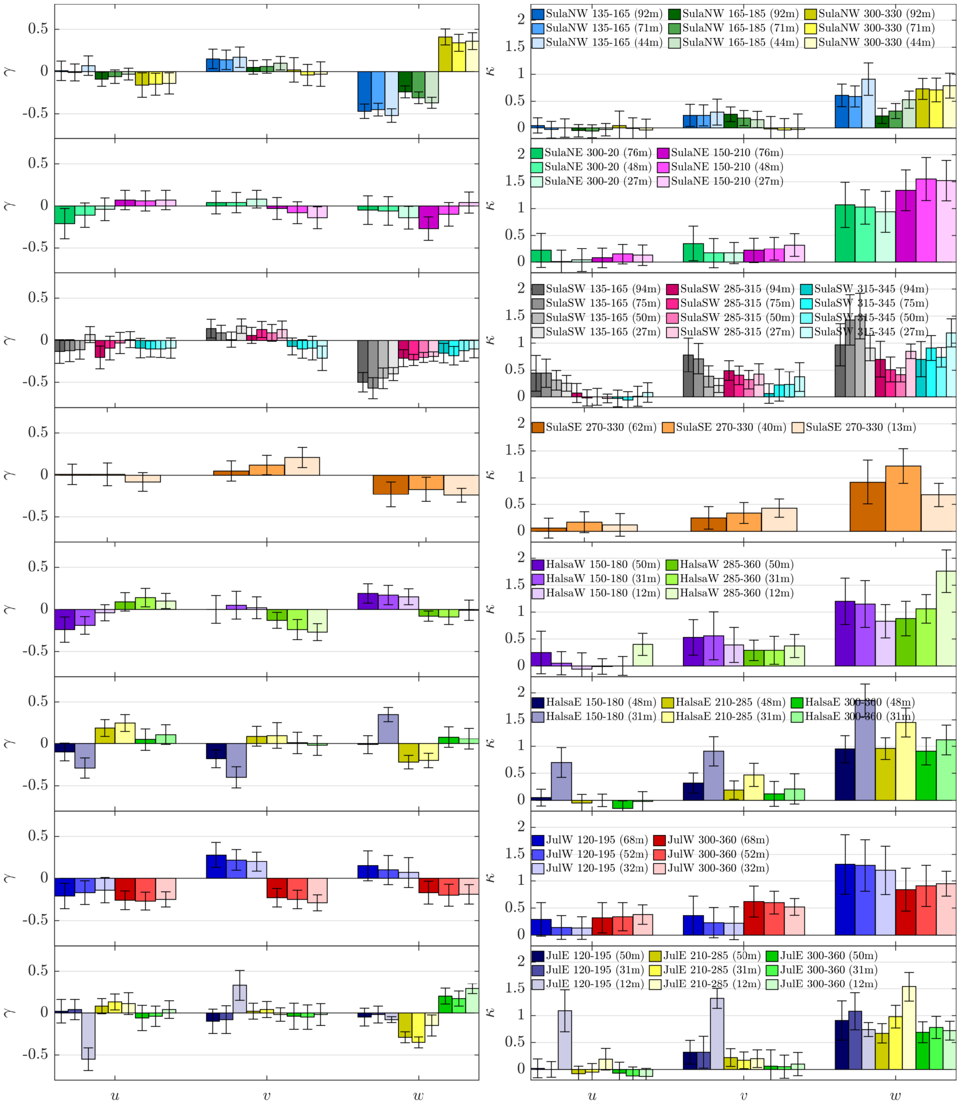

Figure 8: Skewness γ and excess coefficient κ at the met-masts at Sulafjorden, Halsafjorden and Julsundet with $\overline{u} \geqslant 12\,\mathrm{m\,s^{-1}}$ at all heights. Data outside the 1^{st} and 99^{th} percentile were considered as outliers and removed. The error bar represents one standard deviation.

0.15/0.12/0.10, and 0.18/0.16/0.12, respectively. The average values of TIs in these directions are consistent with those reported by [20]. The large values of I_u, between 0.14 and 0.22, observed when the flow is passing over irregular terrains, is also expected and is remarkably close to values observed from the Hardanger

Bridge [70] and the Lysefjord Bridge [21]. Although the wind measurements in Sulafjorden, Halsafjorden and Julsundet are strongly affected by the local topography, the similarities of the values of the turbulence intensities among the three locations as well as with previous studies confirm the relevance of the measurement data for the design of the planned fjord crossings.

Normalized standard deviation

The sector-averaged single-point turbulence statistics and their associated standard deviation are reported for two different cases: (a) For winds coming from directions considered to have long fjord fetch upstream, denoted herein as long-fetch winds (table 5); (b) for winds coming from directions considered to have an irregular topography upstream of the mast referred to as short-fetch winds (table 6). The values of σ_w/u_* are typically in the range of 1.2 to 1.3 for flat and uniform terrain under neutral conditions [35] but can significantly differ from these values in mountainous environment [71]. On the Sotra Bridge, [19] estimated $\sigma_w/u_* \approx 1.5$, whereas values ranging from 1.4 to 1.8 were recorded on the Lysefjord Bridge [21]. The values of σ_w/u_* found in the present studies range also from 1.2 to 1.8 when the wind is blowing over a long fetch. However, for short-fetch winds σ_w/u_* ranges from 1.5 to 2.0. The large scatter observed for the ratio σ_w/u_* is, therefore, linked to the different terrain characteristics at the masts.

The values of σ_u/u_* and σ_v/u_* are challenging to interpret because of the scatter observed. The horizontal turbulence components are more affected by topographical features than the vertical component. Under neutral conditions, the horizontal velocity spectrum contains low-frequency eddies with more energy than the vertical velocity spectrum [72]. This low-frequency range is more easily disturbed by hills and roughness changes than the high-frequency range [73, 74]. Therefore, σ_u/u_* and σ_v/u_* are expected to show an increasing range of values in rough terrain compared to the case of flat terrain. For examples, $\sigma_u/u_* > 2.6$ and $\sigma_v/u_* > 2.0$ are expected in rolling terrain [71]. In the present case, tables 13 to 16 shows values consistent with those recorded at the inlet of a narrow fjord [21]. However, lower-than-expected values of σ_u/u_* are also found in fig. 10. These might be associated with flow along the mountain slopes.

In flat and homogeneous terrain, a ratio $\sigma_w/\sigma_u \approx 0.5$ is expected [75]. This value is also used in the Handbook N400 [76], which is used for the design of suspension-bridges in Norway. The turbulence model by [77], with correction in the inertial sub-range, leads to a ratio $\sigma_w/\sigma_u = 0.57$ [35]. Offshore wind measurements conducted 80 m above the surface for neutral conditions provided $\sigma_w/\sigma_u = 0.53$ [78]. In the present study, the ratio σ_w/σ_u is around or above 0.6 for every anemometer at a height close or equal to 50 m above the ground. Such values are consistent with previous records from fjord-crossing bridges [19, 21] or masts on the shores of Bjørnafjorden [79]. [21] argued that the failure to account for the

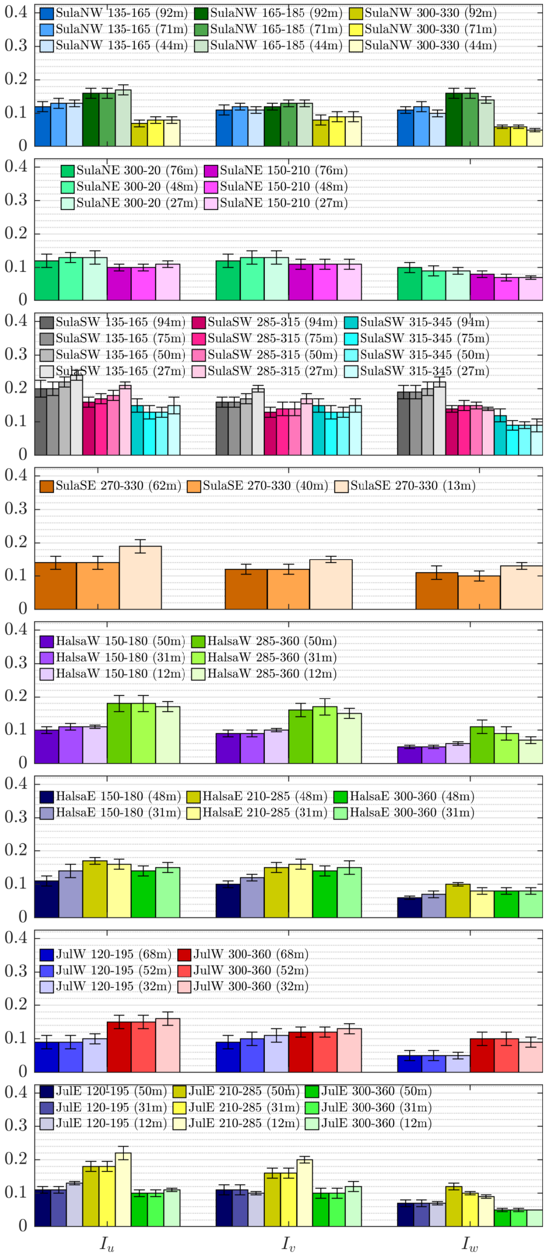

Figure 9: Turbulence intensity of the three velocity components at the met-masts in Sulafjorden, Halsafjorden and Julsundet with $\overline{u} \geqslant 12\,\mathrm{m\,s^{-1}}$ at every height. Data outside the 1^{st} and 99^{th} percentile were considered as outliers and removed. The error bar represents one standard deviation.

Table 5: Normalized standard deviation at Sulafjorden, Halsafjorden and Julsundet, for $\overline{u} > 12\,\mathrm{m\,s^{-1}}$ at every height and at a sector with a long-fetch winds. The anemometers closest to 50 m above ground is chosen.

Mast	Sector (°)	σ_w/u_*	σ_v/u_*	σ_u/u_*	σ_w/σ_u	σ_v/σ_u
SulaNW	300-330	1.41±0.19	2.39±0.56	2.09±0.38	0.68±0.10	1.15±0.24
	135-165	1.97±0.34	2.37±0.42	2.62±0.51	0.76±0.09	0.92±0.14
SulaNE	150-210	1.76±0.30	2.81±0.56	2.65±0.51	0.67±0.09	1.07±0.17
	300-20	1.71±0.33	2.35±0.71	2.40±0.52	0.72±0.10	0.97±0.17
HalsaW	150-180	1.42±0.20	2.32±0.42	2.64±0.43	0.54±0.06	0.88±0.12
HalsaE	150-180	1.57±0.29	2.61±0.52	2.91±0.62	0.55±0.05	0.91±0.11
	300-360	1.39±0.27	2.45±0.48	2.55±0.58	0.56±0.08	0.98±0.16
JulW	120-195	1.46±0.29	2.76±0.53	2.62±0.65	0.57±0.10	1.08±0.20
JulE	120-195	1.65±0.27	2.65±0.68	2.74±0.55	0.61±0.11	0.97±0.17
	300-360	1.21±0.13	2.32±0.59	2.25±0.40	0.55±0.08	1.04±0.22

Table 6: Normalized standard deviation at Sulafjorden, Halsafjorden and Julsundet, for $\overline{u} > 12\,\mathrm{m\,s^{-1}}$ at every height for short-fetch winds. The anemometers closest to 50 m above ground is chosen.

Mast	Sector (°)	σ_w/u_*	σ_v/u_*	σ_u/u_*	σ_w/σ_u	σ_v/σ_u
SulaNW	165-185	1.98±0.33	1.83±0.35	2.32±0.42	0.85±0.07	0.79±0.07
SulaSW	135-165	1.68±0.24	1.44±0.12	1.81±0.17	0.93±0.12	0.80±0.09
	285-315	1.77±0.24	1.72±0.33	2.19±0.27	0.81±0.07	0.79±0.15
SulaSE	270-330	1.47±0.23	1.96±0.42	2.16±0.38	0.69±0.09	0.92±0.18
HalsaW	285-360	1.52±0.26	2.43±0.70	2.74±0.74	0.57±0.08	0.89±0.12
HalsaE	210-285	1.52±0.17	2.41±0.31	2.61±0.27	0.59±0.05	0.93±0.10
JulW	330-360	1.58±0.23	2.04±0.48	2.51±0.35	0.63±0.08	0.81±0.12
JulE	210-285	1.80±0.32	2.44±0.47	2.84±0.49	0.64±0.05	0.86±0.09

unusually high value of σ_w/σ_u in a fjord leads to a substantial underestimation of the vertical buffeting response of a long-span suspension bridge.

A ratio $\sigma_w/\sigma_u > 0.8$ is unusually large but has been reported in some few case studies in fjords [79]. In the present case, $\sigma_w/\sigma_u > 0.8$ might be linked to specific wind directions combined with the proximity of the anemometers being at the flanks of mountains. Providing that the flow is following Sulafjorden, it is unlikely that the value σ_w/σ_u is above 0.8 in the middle of this fjord. In Halsafjorden, the ratio σ_w/σ_u is between 0.50 and 0.60 for the different sectors selected. This indicates that in this fjord, the flow characteristics on the shore might be closer to the case of a flat terrain than at Julsundet or Sulafjorden. In tables 13 to 16, the ratio σ_w/σ_u is below or equal to 0.5 when the anemometers are located 12 m above the ground, which testifies for local flow distortion by the surrounding trees. It should be noted that the ratio $\sigma_w/\sigma_u \approx 0.4$ recorded on the Hardanger bridge [18] is slightly lower than reported in the other Norwegian fjords. It is unsure whether it is due to flow-distortion by the deck, sensor calibration error [80, 81], or simply peculiar flow characteristics at the bridge location.

The ratio σ_v/σ_u is expected to range from 0.7 to 0.9 in flat terrain [75]. The ratio σ_v/σ_u in the Kaimal model is 0.76. In an offshore environment, 80 m above the surface, [21] reported a ratio equal to 0.77. In the present study, the ratio σ_v/σ_u ranges from 0.7 to 1.2 for the different fjords. It appears that ratios close to or larger than one occur when the mountain's flanks are close to the anemometers, which may have a blocking effect and important directional shear, visible in the Reynolds stress tensor. Overall, the values found on the seaside are consistent with the measurement from fjord-crossing bridges [19, 21, 79], except the Hardanger bridge [18], where $\sigma_v/\sigma_u \approx 0.15$, which might not be realistic.

Friction velocity

The reader is reminded that the friction velocity is the fundamental velocity in surface layer scaling [35]. Besides, it conveniently links the logarithmic wind speed profile with the velocity spectra for wind load modelling. The value of friction velocity depends also on the tilt correction algorithm used. As pointed out by [30] or [27], a sectoral planar fit method may not be appropriate in terrain where flow separation occurs, which is likely the case at the mast locations.

In fig. 11, the friction velocity computed using Eq. (5) is compared with the method by [30]. In flat terrain and neutral atmosphere, both approaches to compute u_* should yield similar results. On the other hand, discrepancies are expected in the presence of steep mountains slopes. To assess the influence of $\overline{v'w'}$ and $\overline{u'v'}$ on the friction velocity computed with Klipp's method, correlated wind velocity histories were simulated with non-zero covariance between the three velocity components. The simulated time series showed that $\overline{v'w'}$ and $\overline{u'v'}$ have some influence on the computation of the friction velocity, but these were more limited than observed in fig. 11. Therefore, $\overline{v'w'}$ and $\overline{u'v'}$ may not explain the observed discrepancies, alone, especially if the atmospheric stratification is non-neutral. Although velocity records above $12\,\mathrm{m\,s^{-1}}$ were used, the data set likely includes some samples representative for unstable or stable conditions, especially near the coastline.

As shown in fig. 11 and fig. 12, the friction velocity estimated at Halsafjorden using either Klipp's method or Eq. (5) are in good agreement, even though $\overline{u'v'}/u_*^2$

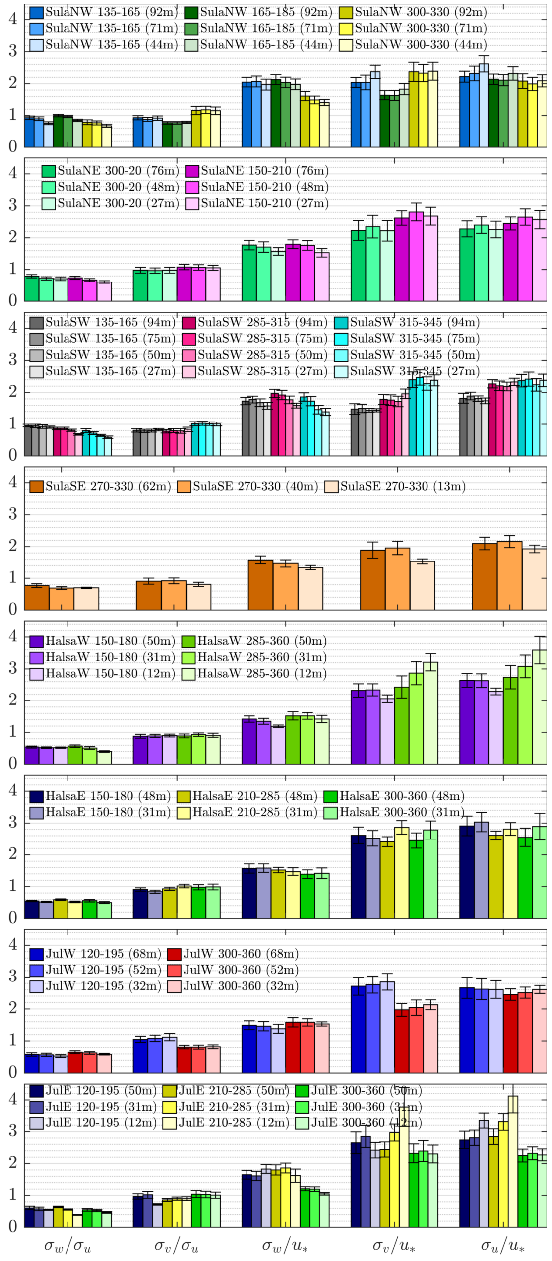

Figure 10: Normalized standard deviation of the three velocity components at the met-masts located in Sulafjorden, Halsafjorden and Julsundet with $\overline{u} \geqslant 12\,\mathrm{m\,s^{-1}}$ at every height. Data outside the 1^{st} and 99^{th} percentile were considered as outliers and removed. The error bar represents one standard deviation.

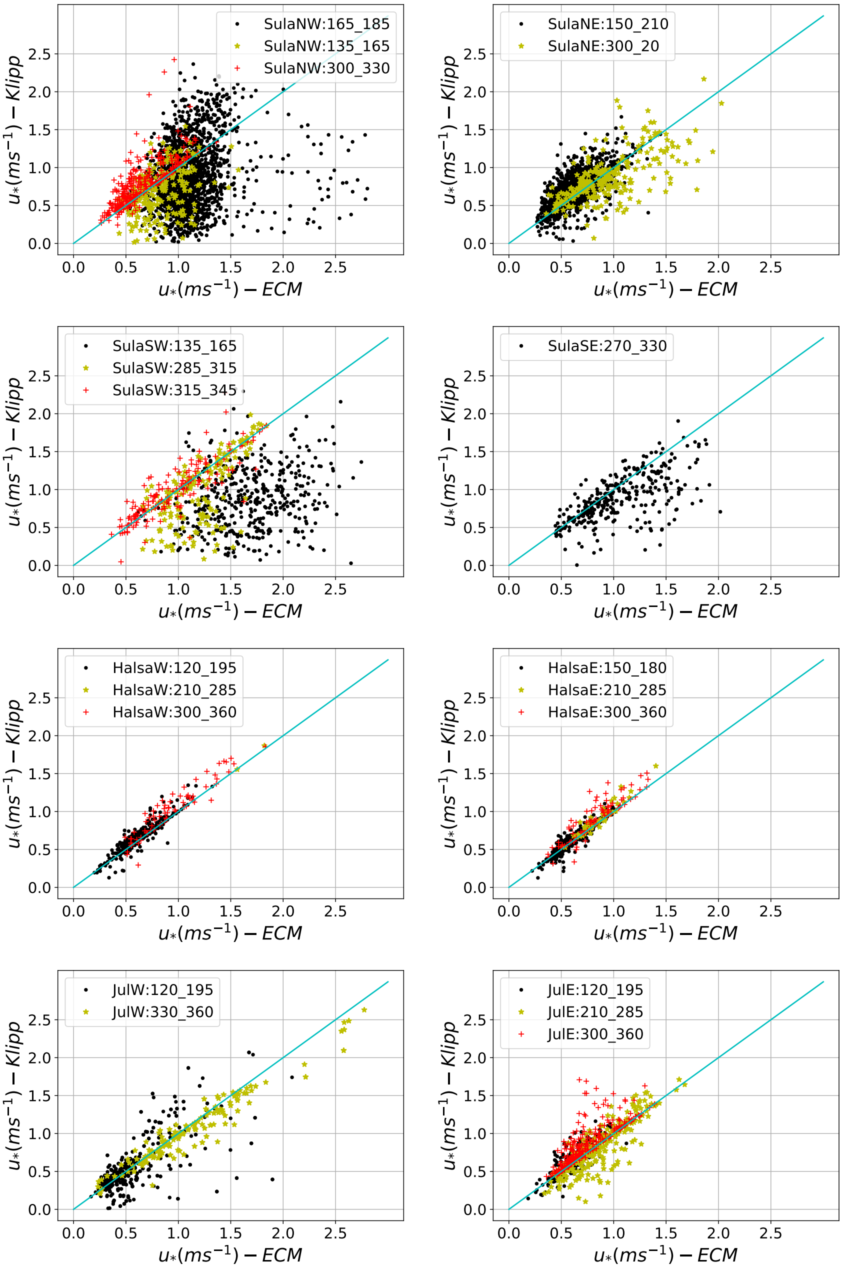

Figure 11: Friction velocity calculated with the eddy-covariance method (ECM, Eq. (5)) and Klipp's method using data collected by the anemometer closest to 50 m above the ground at each mast between the 01-01-2018 to 31-12-2019.

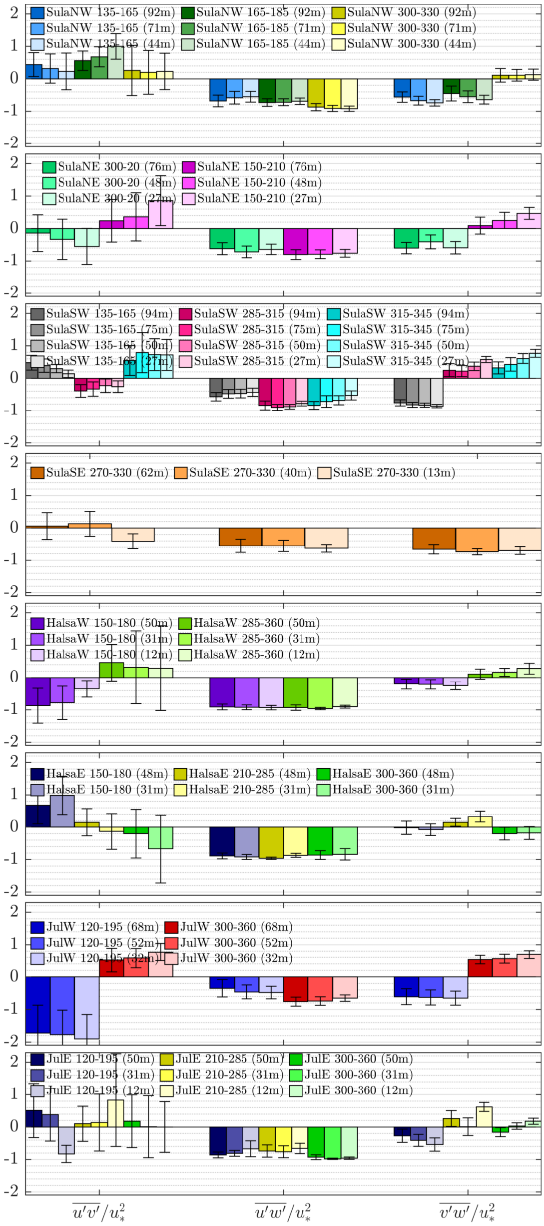

Figure 12: Turbulent momentum fluxes at the met-masts at Sulafjorden, Halsafjorden and Julsundet with $\overline{u} \geqslant 12\,\mathrm{m\,s^{-1}}$ at every height. Data outside the 1^{st} and 99^{th} percentile were considered as outliers and removed. The error bar represents one standard deviation.

can have the same magnitude as $\overline{u'w'}/u_*^2$. In Halsafjorden, the term $\overline{v'w'/u_*^2}$ is close to zero while this is not the case for the masts at Sulafjorden and Julsundet, where the mountains are steeper and higher than at Halsafjorden. One exception is observed at Sulafjorden, for which $\overline{v'w'}/u_*^2$ is small when the wind is blowing from northwest, the reason for this is, however, unclear. Nevertheless, the study of momentum fluxes helps to better understand the influence of topography on the measurements.

5. Conclusions

The paper explores a subset of a larger data set aiming to identify the wind conditions relevant for bridge design at three potential fjord-crossing sites, in complex coastal terrain, in western Norway. Two years of continuous wind measurements were analysed, at heights between 12 m and 95 m above the ground, in masts located on the shore of the three fjords Sulafjorden, Julsundet and Halsafjorden. Eight masts were considered for the analysis, each of them instrumented with three to four sonic anemometers, i.e., 25 sonic 3D anemometers in total.

To focus on strong wind conditions of particular relevance for bridge design, only samples with a mean wind speed above $12\,\mathrm{m\,s^{-1}}$ were selected. The goal was to quantify to what extend the local topography affects the flow conditions recorded at the shoreline by the anemometers and how met-masts can be used to collect and provide correspondingly filtered data valuable for bridge-design. The study highlighted also some challenges associated with flow characterization near mountain slopes, especially for the design of wind-sensitive structures. The main findings of the study are as follows

- Many of the masts are in sheltered locations where weak winds are predominant. Wind speeds above $12\,\mathrm{m\,s^{-1}}$ are uncommon at several of the sites during the period analysed. This implies that several years of data are required to capture a sufficient amount of strong wind conditions, critical for the relevant bridge design.

- The flow on the shore of the fjords is horizontal for a limited number of situations only. A median incidence angle up to -9.5° was measured at Sulafjorden. In Halsafjorden and Julsundet, values up to $+7.7^\circ$ and $+3.8^\circ$ were observed. For the majority of the directional sectors considered, the mean wind speed profiles fitted by the wind profile power law provided shear coefficients below 0.10. A low mean wind shear may reflect the flow speed-up above the hills. Such observations indicated that, at several occasions, the sensors were likely inside the internal boundary layers created by the rough terrain upstream of the masts.

- Significant deviations from the assumption of Gaussian fluctuations were observed. The non-Gaussianity was assessed using the skewness and excess kurtosis. Non-Gaussian fluctuations were particularly strong in the vertical velocity component whereas the along-wind component was generally Gaussian, except when the flow was distorted by the surrounding vegetation. The influence of the terrain upwind to the masts on the skewness and excess kurtosis was significant, especially for the lateral velocity component, at heights below 15 m and in the roughness sublayer. The skewness deviates significantly from zero, indicating non-Gaussian fluctuations. Finally, it was found that a horizontal flow does not imply Gaussian fluctuations on the shore of a fjord.

- The turbulence intensity showed a clear dependency on the sector selected. For sectors characterized by a large fjord fetch, the ensemble-averaged values for the turbulence intensities were up to 0.11 for the horizontal components and up to 0.08 for the vertical component. For the sector characterized by complex upstream topography, much larger values were measured with I_u, I_v and I_w up to 0.22, 0.17, and 0.20, respectively. These observations highlight the importance of studying sectorial differences of the wind conditions at the masts and for bridge design.

- The normalized standard deviation σ_w/σ_u and σ_v/σ_u were close to the values previously reported in the literature in Norwegian fjords. In the present case, σ_w/σ_u was around or above 0.6. While σ_v/σ_u ranged from 0.7 to 1.2. These values are larger than advised in the handbook N400, used for the design of long-span suspension bridges in Norway. The ratio of the vertical standard deviation with the friction velocity σ_w/u_* showed a clear dependency on the wind sector chosen, ranging from 1.2 to 1.8 for long-fetch winds and from 1.5 to 2.0 when approaching over complex terrain.

- Two methods to compute the friction velocity were assessed. Results suggested that at Halsafjorden, the turbulence measurements were less affected by the surrounding mountains than in Sulafjorden. Nevertheless, it is still unsure whether the friction velocity u_* computed with Klipp's method given in Eq. (6) or the traditional double-rotation technique and Eq. (5) should be used. Studies including an analysis of the Reynolds stress in complex terrain are scarce and often linked to boundary-layer micrometeorology. Therefore, it is legitimate to wonder if and how $\overline{u'v'}$ and $\overline{v'w'}$ should be accounted for in wind load modelling on structures.

The mast measurements near the shore of Sulafjorden, Halsafjorden and Julsundet provided valuable information on the local wind conditions. However, the aforementioned results suggest that the integral turbulence characteristics recorded on the seaside may not be representative of the flow conditions in the middle of the fjord. Therefore, to estimate the turbulent load acting on the deck of a fjord-crossing bridge with higher confidence, computational fluid dynamic (CFD) simulations or remote sensing observations of the flow field may be required to complement these anemometers records.

The integral flow characteristics provide only a partial understanding of the local flow conditions because turbulence covers a large range of wavenumbers or frequencies. The blocking by the surface distorts more easily large eddies, which are associated with low wavenumbers, than smaller eddies [82–84]. Also, the low-frequency range of the turbulence spectrum can be substantially affected by roughness changes and hills [73, 74]. The detailed assessment of the turbulence characteristics on the shores of fjords can be achieved through spectral analysis, providing that the velocity records can be described as stationary, ergodic random processes.

Therefore, the second part of the present study will focus on the spectral energy content of the velocity fluctuations. The one-point power spectral density can be used to indicate which frequency range is no-longer affected by the local topography and whether such a range has similar characteristics to traditional velocity spectra [77]. The adequacy of computation of the friction velocity with Klipp's method [30] will also be assessed in terms of normalization of the velocity spectra. This will help to investigate to what degree such a normalization follows surface-layer scaling in fjords. Two-point spectral densities will be studied through the coherence function. In particular, the blocking by the surface could substantially affect the vertical coherence such that Bowen's scaling [85, 86] may become more appropriate than Davenport's scaling [3] for the design and construction of the bridge towers.

6. Acknowledgements

This work and the measurement campaign is financed by the Norwegian Public Roads Administration as part of the Coastal Highway E39 project in Mid-Norway. We also want to thank Birgitte R. Furevik, Jørn Kristiansen and Knut Helge Midtbø (Norwegian Meteorological Institute), Konstantinos Christakos (University of Bergen), and Adil Rasheed (Norwegian University of Science and Technology) for providing resources and guidance necessary for this work.

7. Appendix

Table 7: Flow Gaussianity: Wind direction, height above terrain (H), number of samples (N), skewness γ, excess coefficient κ and associated standard deviation at the met-masts at Sulafjorden (SulaNW and SulaNE). Wind velocity above $12\,\mathrm{m\,s^{-1}}$ for all elevations. Data outside the 1^{st} and 99^{th} percentile were considered as outliers and removed.

Mast	Sector (°)	H	N	γ_u	γ_v	γ_w	κ_u	κ_v	κ_w
SulaNW	135-165	92	64	0.01±0.23	0.15±0.23	-0.47±0.17	0.05±0.29	0.24±0.41	0.61±0.42
		71	100	-0.01±0.20	0.14±0.23	-0.45±0.15	-0.03±0.32	0.24±0.39	0.59±0.39
		44	69	0.07±0.23	0.17±0.24	-0.52±0.16	0.00±0.35	0.30±0.48	0.91±0.60
	165-185	92	537	-0.09±0.17	0.05±0.16	-0.24±0.14	-0.05±0.24	0.26±0.27	0.23±0.28
		71	522	-0.06±0.16	0.06±0.16	-0.31±0.14	-0.06±0.25	0.19±0.28	0.32±0.28
		44	519	-0.03±0.14	0.10±0.16	-0.37±0.13	-0.03±0.24	0.16±0.31	0.53±0.32
	300-330	92	96	-0.16±0.29	0.02±0.29	0.41±0.19	0.05±0.54	-0.02±0.48	0.73±0.39
		71	87	-0.15±0.26	-0.04±0.25	0.34±0.20	-0.01±0.41	-0.04±0.44	0.71±0.44
		44	112	-0.14±0.25	-0.03±0.29	0.36±0.20	-0.04±0.42	-0.03±0.59	0.79±0.46
SulaNE	300-20	76	83	-0.21±0.36	0.04±0.27	-0.05±0.34	0.22±0.64	0.35±0.65	1.07±0.84
		48	97	-0.11±0.29	0.04±0.24	-0.06±0.34	0.01±0.42	0.17±0.55	1.03±0.64
		27	96	-0.04±0.27	0.08±0.21	-0.14±0.27	0.04±0.43	0.17±0.40	0.94±0.76
	150-210	76	533	0.07±0.23	-0.03±0.26	-0.27±0.28	0.08±0.37	0.22±0.46	1.34±0.76
		48	637	0.06±0.24	-0.08±0.26	-0.10±0.28	0.15±0.37	0.25±0.43	1.55±0.80
		27	637	0.07±0.23	-0.14±0.26	0.04±0.25	0.13±0.39	0.32±0.43	1.52±0.75

Table 8: Flow Gaussianity: Wind direction, height above terrain (H), number of samples (N), skewness γ, excess coefficient κ and associated standard deviation at the met-masts at Sulafjorden (SulaSW and SulaSE). Wind velocity above $12\,\mathrm{m\,s^{-1}}$ for all elevations. Data outside the 1^{st} and 99^{th} percentile were considered as outliers and removed.

SulaSW	135-165	94	92	-0.13±0.28	0.14±0.22	-0.50±0.23	0.44±0.67	0.78±0.63	0.97±0.78
		75	120	-0.12±0.26	0.09±0.18	-0.57±0.25	0.44±0.53	0.71±0.57	1.43±0.93
		50	131	-0.11±0.22	0.01±0.18	-0.45±0.25	0.31±0.37	0.38±0.40	1.50±0.84
		27	80	0.07±0.19	0.17±0.17	-0.40±0.16	0.25±0.29	0.21±0.26	0.91±0.47
	285-315	94	34	-0.20±0.27	0.06±0.19	-0.21±0.20	0.07±0.35	0.49±0.37	0.70±0.67
		75	48	-0.09±0.28	0.13±0.19	-0.23±0.13	-0.02±0.30	0.40±0.35	0.51±0.47
		50	52	-0.03±0.25	0.09±0.20	-0.20±0.12	-0.00±0.31	0.32±0.35	0.41±0.27
		27	31	0.01±0.19	0.13±0.20	-0.19±0.11	-0.03±0.16	0.42±0.40	0.85±0.27
	315-345	94	39	-0.09±0.23	-0.07±0.20	-0.15±0.23	-0.03±0.31	0.06±0.36	0.70±0.66
		75	37	-0.10±0.19	-0.10±0.22	-0.18±0.22	-0.06±0.31	0.22±0.60	0.91±0.46
		50	33	-0.10±0.20	-0.09±0.28	-0.12±0.25	0.01±0.37	0.23±0.47	0.74±0.36
		27	39	-0.09±0.24	-0.21±0.29	-0.10±0.21	0.08±0.36	0.37±0.54	1.19±0.52
SulaSE	270-330	62	128	0.01±0.24	0.05±0.24	-0.23±0.30	0.06±0.37	0.25±0.42	0.92±0.82
		40	121	0.01±0.27	0.12±0.23	-0.17±0.29	0.17±0.39	0.34±0.39	1.22±0.64
		13	59	-0.08±0.22	0.21±0.24	-0.24±0.17	0.12±0.42	0.43±0.34	0.68±0.44

Table 9: Flow Gaussianity: Wind direction, height above terrain (H), number of samples (N), skewness γ, excess coefficient κ and associated standard deviation at the met-masts at Halsafjorden. Wind velocity above $12\,\mathrm{m\,s^{-1}}$ for all elevations. Data outside the 1^{st} and 99^{th} percentile were considered as outliers and removed.

Mast	Sector (°)	H	N	γ_u	γ_v	γ_w	κ_u	κ_v	κ_w
HalsaW	150-180	50	170	-0.24±0.30	0.00±0.33	0.19±0.23	0.25±0.79	0.53±0.66	1.20±0.86
		31	155	-0.19±0.21	0.05±0.33	0.17±0.23	0.05±0.43	0.56±0.89	1.15±0.87
		12	114	-0.04±0.19	0.02±0.26	0.15±0.19	-0.06±0.61	0.39±0.65	0.83±0.62
	285-360	50	27	0.09±0.22	-0.13±0.19	-0.08±0.12	-0.01±0.29	0.29±0.38	0.88±0.64
		31	24	0.14±0.22	-0.24±0.24	-0.09±0.18	-0.00±0.35	0.29±0.52	1.06±0.53
		12	21	0.10±0.18	-0.27±0.20	-0.01±0.24	0.40±0.41	0.37±0.43	1.76±0.79
HalsaE	150-180	48	199	-0.10±0.21	-0.18±0.21	-0.01±0.22	0.05±0.31	0.32±0.37	0.95±0.51
		31	172	-0.29±0.24	-0.40±0.25	0.35±0.17	0.70±0.55	0.91±0.55	1.86±0.61
	210-285	48	33	0.19±0.20	0.09±0.24	-0.22±0.16	-0.05±0.32	0.19±0.34	0.96±0.41
		31	19	0.25±0.20	0.10±0.31	-0.20±0.17	-0.00±0.23	0.47±0.43	1.45±0.54
	300-360	48	43	0.05±0.26	0.01±0.26	0.08±0.25	-0.15±0.28	0.12±0.46	0.91±0.51
		31	31	0.11±0.24	-0.02±0.24	0.06±0.25	-0.02±0.36	0.21±0.56	1.12±0.56

Table 10: Flow Gaussianity: Wind direction, height above terrain (H), number of samples (N), skewness γ, excess coefficient κ and associated standard deviation at the met-masts at Julsundet. Wind velocity above $12\,\mathrm{m\,s^{-1}}$ for all elevations. Data outside the 1^{st} and 99^{th} percentile were considered as outliers and removed.

JulW	120-195	68	96	-0.21±0.30	0.28±0.30	0.15±0.36	0.29±0.62	0.36±0.72	1.31±1.11
		52	192	-0.17±0.28	0.22±0.25	0.10±0.35	0.14±0.44	0.23±0.56	1.29±0.96
		32	198	-0.14±0.30	0.20±0.23	0.07±0.36	0.13±0.42	0.22±0.61	1.20±0.90
	330-360	68	45	-0.26±0.22	-0.23±0.22	-0.17±0.27	0.32±0.56	0.62±0.57	0.84±0.79
		52	92	-0.27±0.21	-0.25±0.22	-0.20±0.26	0.34±0.52	0.60±0.42	0.91±0.76
		32	74	-0.25±0.18	-0.29±0.19	-0.19±0.23	0.38±0.36	0.52±0.31	0.95±0.46
JulE	120-195	50	97	0.02±0.28	-0.10±0.29	-0.05±0.21	0.02±0.35	0.32±0.44	0.91±0.73
		31	102	0.04±0.24	-0.08±0.33	-0.02±0.20	0.00±0.29	0.32±0.59	1.08±0.69
		12	5	-0.55±0.27	0.33±0.36	-0.08±0.07	1.09±0.78	1.32±0.37	0.74±0.26
	210-285	50	111	0.08±0.18	0.02±0.19	-0.29±0.13	-0.08±0.28	0.22±0.33	0.67±0.36
		31	110	0.13±0.19	0.04±0.19	-0.35±0.13	-0.05±0.32	0.17±0.31	0.98±0.42
		12	49	0.11±0.26	-0.02±0.16	-0.15±0.25	0.19±0.40	0.20±0.33	1.54±0.54
	300-360	50	91	-0.06±0.30	-0.04±0.31	0.20±0.19	-0.07±0.41	0.06±0.61	0.69±0.39
		31	91	-0.04±0.24	-0.05±0.29	0.17±0.18	-0.12±0.33	0.05±0.43	0.78±0.41
		12	75	0.04±0.21	-0.02±0.26	0.29±0.12	-0.13±0.30	0.10±0.43	0.72±0.35

Table 11: Turbulence intensity: Wind direction, height above terrain (H), number of samples (N) and the turbulence intensities (TI) and associated standard deviations at the met-masts at Sulafjorden with $\overline{u} \geqslant 12\,\mathrm{m\,s^{-1}}$ at every height. Data outside the 1^{st} and 99^{th} percentile were considered as outliers and removed.

Mast	Sector (°)	Sensor h. (H)	N	I_u	I_v	I_w
SulaNW	135-165	92	64	0.12±0.03	0.11±0.03	0.11±0.02
		71	100	0.13±0.03	0.12±0.02	0.12±0.03
		44	69	0.13±0.02	0.11±0.02	0.10±0.02
	165-185	92	537	0.16±0.03	0.12±0.02	0.16±0.03
		71	522	0.16±0.03	0.13±0.02	0.16±0.03
		44	519	0.17±0.03	0.13±0.02	0.14±0.02
	300-330	92	96	0.07±0.02	0.08±0.03	0.06±0.01
		71	87	0.08±0.02	0.09±0.03	0.06±0.01
		44	112	0.08±0.02	0.09±0.03	0.05±0.01
SulaNE	300-20	76	83	0.12±0.04	0.12±0.04	0.10±0.03
		48	97	0.13±0.03	0.13±0.04	0.09±0.03
		27	96	0.13±0.04	0.13±0.04	0.09±0.02
	150-210	76	533	0.10±0.02	0.11±0.03	0.08±0.02
		48	637	0.10±0.02	0.11±0.03	0.07±0.02
		27	637	0.11±0.02	0.11±0.03	0.07±0.01
SulaSW	135-165	94	92	0.20±0.05	0.16±0.03	0.19±0.04
		75	120	0.20±0.04	0.16±0.03	0.19±0.04
		50	131	0.22±0.03	0.17±0.03	0.20±0.04
		27	80	0.24±0.03	0.20±0.02	0.22±0.03
	285-315	94	34	0.16±0.03	0.13±0.03	0.14±0.02
		75	48	0.17±0.03	0.14±0.04	0.15±0.03
		50	52	0.18±0.03	0.14±0.04	0.15±0.02
		27	31	0.21±0.02	0.17±0.03	0.14±0.01
	315-345	94	39	0.15±0.04	0.15±0.04	0.12±0.04
		75	37	0.13±0.04	0.13±0.04	0.09±0.03
		50	33	0.13±0.03	0.13±0.03	0.09±0.02
		27	39	0.15±0.05	0.15±0.04	0.09±0.04
SulaSE	270-330	62	128	0.14±0.04	0.12±0.03	0.11±0.04
		40	121	0.14±0.04	0.12±0.03	0.10±0.03
		13	59	0.19±0.04	0.15±0.02	0.13±0.02

Table 12: Turbulence intensity: Wind direction, height above terrain (H), number of samples (N) and the turbulence intensities (TI) and associated standard deviations at the met-masts at Halsafjorden and Julsundet with $\overline{u} \geqslant 12\,\mathrm{m\,s^{-1}}$ at every height. Data outside the 1^{st} and 99^{th} percentile were considered as outliers and removed.

Mast	Sector (°)	Sensor h. (H)	N	I_u	I_v	I_w
HalsaW	150-180	50	170	0.10±0.02	0.09±0.02	0.05±0.01
		31	155	0.11±0.02	0.09±0.02	0.05±0.01
		12	114	0.11±0.01	0.10±0.01	0.06±0.01
	285-360	50	27	0.18±0.05	0.16±0.04	0.11±0.04
		31	24	0.18±0.05	0.17±0.05	0.09±0.04
		12	21	0.17±0.03	0.15±0.03	0.07±0.02
HalsaE	150-180	48	199	0.11±0.03	0.10±0.02	0.06±0.01
		31	172	0.14±0.04	0.12±0.02	0.07±0.02
	210-285	48	33	0.17±0.02	0.15±0.03	0.10±0.01
		31	19	0.16±0.03	0.16±0.03	0.08±0.02
	300-360	48	43	0.14±0.03	0.14±0.03	0.08±0.02
		31	31	0.15±0.03	0.15±0.04	0.08±0.02
JulW	120-195	68	96	0.09±0.04	0.09±0.04	0.05±0.03
		52	192	0.09±0.04	0.10±0.04	0.05±0.03
		32	198	0.10±0.03	0.11±0.04	0.05±0.02
	330-360	68	45	0.15±0.04	0.12±0.03	0.10±0.04
		52	92	0.15±0.04	0.12±0.03	0.10±0.04
		32	74	0.16±0.04	0.13±0.03	0.09±0.03
JulE	120-195	50	97	0.11±0.02	0.11±0.03	0.07±0.02
		31	102	0.11±0.02	0.11±0.03	0.07±0.02
		12	5	0.13±0.01	0.10±0.01	0.07±0.01
	210-285	50	111	0.18±0.03	0.16±0.03	0.12±0.02
		31	110	0.18±0.03	0.16±0.03	0.10±0.01
		12	49	0.22±0.04	0.20±0.02	0.09±0.01
	300-360	50	91	0.10±0.02	0.10±0.03	0.05±0.01
		31	91	0.10±0.02	0.10±0.03	0.05±0.01
		12	75	0.11±0.01	0.12±0.03	0.05±0.00

Table 13: Normalized standard deviation: Wind direction, height above terrain (H), number of samples (N), normalized standard deviation and associated standard deviation at the met-masts at Sulafjorden (SulaNW and SulaNE). Wind velocity above $12\,\mathrm{m\,s^{-1}}$ for all elevations. Data outside the 1^{st} and 99^{th} percentile were considered as outliers and removed.

Mast	Sector (°)	Sensor height (H)	N	σ_w/u_*	σ_v/u_*	σ_u/u_*	σ_w/σ_u	σ_v/σ_u
SulaNW	135-165	92	64	2.05±0.30	2.04±0.31	2.22±0.34	0.93±0.11	0.93±0.13
		71	100	2.07±0.34	2.04±0.46	2.32±0.46	0.90±0.12	0.88±0.12
		44	69	1.97±0.34	2.37±0.42	2.62±0.51	0.76±0.09	0.92±0.14
	165-185	92	537	2.13±0.31	1.64±0.28	2.14±0.32	1.00±0.08	0.77±0.08
		71	522	2.04±0.33	1.63±0.31	2.11±0.35	0.97±0.07	0.77±0.08
		44	519	1.98±0.33	1.83±0.35	2.32±0.42	0.85±0.07	0.79±0.07
	300-330	92	96	1.61±0.29	2.37±0.60	2.08±0.46	0.79±0.15	1.16±0.26
		71	87	1.49±0.24	2.33±0.54	1.99±0.42	0.77±0.13	1.18±0.23
		44	112	1.41±0.19	2.39±0.56	2.09±0.38	0.68±0.10	1.15±0.24
SulaNE	300-20	76	83	1.77±0.30	2.23±0.62	2.28±0.50	0.79±0.10	0.98±0.18
		48	97	1.71±0.33	2.35±0.71	2.40±0.52	0.72±0.10	0.97±0.17
		27	96	1.57±0.24	2.22±0.64	2.26±0.52	0.71±0.11	0.98±0.18
	150-210	76	533	1.80±0.27	2.62±0.45	2.45±0.41	0.74±0.10	1.08±0.17
		48	637	1.76±0.30	2.81±0.56	2.65±0.51	0.67±0.09	1.07±0.17
		27	637	1.53±0.27	2.68±0.56	2.57±0.57	0.61±0.08	1.06±0.16

Table 14: Normalized standard deviation: Wind direction, height above terrain (H), number of samples (N), normalized standard deviation and associated standard deviation at the met-masts at Sulafjorden (SulaSW and SulaSE). Wind velocity above 12 m s^{-1} for all elevations. Data outside the 1st and 99th percentile were considered as outliers and removed.

SulaSW	135-165	94	92	1.73±0.23	1.48±0.34	1.82±0.31	0.96±0.08	0.81±0.11
		75	120	1.78±0.21	1.50±0.26	1.89±0.24	0.95±0.10	0.79±0.10
		50	131	1.68±0.24	1.44±0.12	1.81±0.17	0.93±0.12	0.80±0.09
		27	80	1.58±0.21	1.44±0.10	1.74±0.18	0.91±0.07	0.83±0.08
	285-315	94	34	1.97±0.26	1.78±0.31	2.27±0.26	0.87±0.08	0.78±0.11
		75	48	1.92±0.29	1.76±0.33	2.21±0.30	0.87±0.08	0.80±0.12
		50	52	1.77±0.24	1.72±0.33	2.19±0.27	0.81±0.07	0.79±0.15
		27	31	1.59±0.15	1.96±0.30	2.33±0.23	0.68±0.05	0.84±0.14
	315-345	94	39	1.86±0.26	2.40±0.49	2.37±0.39	0.80±0.12	1.02±0.12
		75	37	1.73±0.29	2.47±0.48	2.42±0.44	0.72±0.09	1.03±0.12
		50	33	1.46±0.27	2.28±0.42	2.24±0.39	0.65±0.07	1.02±0.11
		27	39	1.39±0.22	2.38±0.34	2.38±0.39	0.59±0.08	1.01±0.12
SulaSE	270-330	62	130	1.58±0.25	1.89±0.51	2.10±0.39	0.77±0.12	0.91±0.19
		40	121	1.47±0.23	1.96±0.42	2.16±0.38	0.69±0.09	0.92±0.18
		13	59	1.34±0.13	1.53±0.16	1.93±0.24	0.70±0.04	0.81±0.13

Table 15: Normalized standard deviation: Wind direction, height above terrain (H), number of samples (N), normalized standard deviation and associated standard deviation at the met-masts at Halsafjorden. Wind velocity above 12 m s^{-1} for all elevations. Data outside the 1st and 99th percentile were considered as outliers and removed.

HalsaW	150-180	50	170	1.42±0.20	2.32±0.42	2.64±0.43	0.54±0.06	0.88±0.12
		31	155	1.35±0.19	2.34±0.38	2.63±0.43	0.52±0.05	0.89±0.10
		12	114	1.19±0.08	2.06±0.24	2.29±0.21	0.52±0.04	0.90±0.09
	285-360	50	27	1.52±0.26	2.43±0.70	2.74±0.74	0.57±0.08	0.89±0.12
		31	24	1.52±0.21	2.87±0.73	3.08±0.71	0.51±0.09	0.93±0.11
		12	21	1.42±0.23	3.21±0.54	3.59±0.86	0.40±0.05	0.91±0.13
HalsaE	150-180	48	199	1.57±0.29	2.61±0.52	2.91±0.62	0.55±0.05	0.91±0.11
		31	172	1.58±0.27	2.52±0.49	3.03±0.61	0.52±0.04	0.84±0.10
	210-285	48	33	1.52±0.17	2.41±0.31	2.61±0.27	0.59±0.05	0.93±0.10
		31	19	1.47±0.24	2.86±0.43	2.81±0.40	0.52±0.05	1.02±0.11
	300-360	48	43	1.39±0.27	2.45±0.48	2.55±0.58	0.56±0.08	0.98±0.16
		31	31	1.42±0.33	2.78±0.57	2.89±0.83	0.50±0.06	0.99±0.18

Table 16: Normalized standard deviation: Wind direction, height above terrain (H), number of samples (N), normalized standard deviation and associated standard deviation at the met-masts at Julsundet. Wind velocity above 12 m s^{-1} for all elevations. Data outside the 1st and 99th percentile were considered as outliers and removed.

JulW	120-195	68	96	1.49±0.28	2.71±0.56	2.66±0.66	0.58±0.11	1.05±0.19
		52	192	1.46±0.29	2.76±0.53	2.62±0.65	0.57±0.10	1.08±0.20
		32	198	1.38±0.28	2.85±0.52	2.61±0.56	0.53±0.09	1.12±0.23
	330-360	68	45	1.58±0.29	1.97±0.40	2.45±0.36	0.65±0.09	0.81±0.11
		52	92	1.58±0.23	2.04±0.48	2.51±0.35	0.63±0.08	0.81±0.12
		32	74	1.53±0.13	2.13±0.31	2.61±0.25	0.59±0.05	0.82±0.12
JulE	120-195	50	97	1.65±0.27	2.65±0.68	2.74±0.55	0.61±0.11	0.97±0.17
		31	102	1.61±0.29	2.85±0.69	2.81±0.48	0.58±0.11	1.02±0.21
		12	5	1.83±0.28	2.42±0.49	3.35±0.48	0.55±0.03	0.72±0.05
	210-285	50	111	1.80±0.32	2.44±0.47	2.84±0.49	0.64±0.05	0.86±0.09
		31	110	1.86±0.31	2.97±0.53	3.31±0.53	0.56±0.04	0.90±0.10
		12	49	1.62±0.42	3.78±1.23	4.12±1.05	0.39±0.02	0.90±0.12
	300-360	50	91	1.21±0.13	2.32±0.59	2.25±0.40	0.55±0.08	1.04±0.22
		31	91	1.20±0.14	2.39±0.66	2.32±0.40	0.53±0.07	1.03±0.21
		12	75	1.05±0.08	2.30±0.56	2.27±0.37	0.47±0.05	1.01±0.19

Table 17: Normalized momentum fluxes: Wind direction, height above terrain (H), number of samples (N), horizontal and vertical momentum fluxes and associated standard deviation at the met-masts at Sulafjorden. Wind velocity above $12\,\mathrm{m\,s^{-1}}$ for all elevations. Data outside the 1^{st} and 99^{th} percentile were considered as outliers and removed.

Mast	Sector (°)	Sensor h. (H)	N	$\frac{\overline{u'v'}}{u_*^2}$	$\frac{\overline{u'w'}}{u_*^2}$	$\frac{\overline{v'w'}}{u_*^2}$
SulaNW	135-165	92	64	0.44±0.74	-0.68±0.36	-0.56±0.32
		71	100	0.32±0.90	-0.58±0.39	-0.67±0.27
		44	69	0.23±1.13	-0.55±0.33	-0.74±0.20
	165-185	92	537	0.56±0.60	-0.73±0.23	-0.45±0.46
		71	522	0.68±0.62	-0.72±0.21	-0.55±0.36
		44	519	1.00±0.79	-0.69±0.20	-0.64±0.27
	300-330	92	96	0.26±1.55	-0.87±0.22	0.11±0.42
		71	87	0.20±1.35	-0.91±0.19	0.11±0.36
		44	112	0.23±1.12	-0.92±0.16	0.13±0.34
SulaNE	300-20	76	83	-0.14±1.13	-0.62±0.37	-0.60±0.35
		48	97	-0.33±1.24	-0.72±0.36	-0.41±0.43
		27	96	-0.55±1.11	-0.64±0.32	-0.59±0.38
	150-210	76	533	0.24±1.31	-0.80±0.30	0.09±0.52
		48	637	0.36±1.48	-0.79±0.27	0.25±0.50
		27	637	0.86±1.54	-0.76±0.24	0.47±0.37
SulaSW	135-165	94	92	0.48±0.45	-0.57±0.26	-0.76±0.19
		75	120	0.39±0.41	-0.48±0.27	-0.82±0.16
		50	131	0.30±0.26	-0.47±0.27	-0.83±0.13
		27	80	0.14±0.23	-0.43±0.25	-0.86±0.10
	285-315	94	34	-0.39±0.39	-0.84±0.28	0.25±0.40
		75	48	-0.33±0.44	-0.90±0.18	0.22±0.34
		50	52	-0.23±0.42	-0.88±0.14	0.37±0.26
		27	31	-0.26±0.36	-0.78±0.15	0.58±0.19
	315-345	94	39	0.55±0.92	-0.84±0.24	0.32±0.37
		75	37	0.79±1.24	-0.72±0.36	0.43±0.42
		50	33	0.73±0.98	-0.68±0.28	0.61±0.30
		27	39	0.72±0.95	-0.53±0.28	0.77±0.24
SulaSE	270-330	62	128	0.06±0.83	-0.55±0.41	-0.66±0.30
		40	121	0.13±0.77	-0.55±0.35	-0.74±0.19
		13	59	-0.41±0.46	-0.63±0.24	-0.70±0.23

Table 18: Normalized momentum fluxes: Wind direction, height above terrain (H), number of samples (N), horizontal and vertical momentum fluxes and associated standard deviation at the met-masts at Halsafjorden and Julsundet. Wind velocity above $12\,\mathrm{m\,s^{-1}}$ for all elevations. Data outside the 1^{st} and 99^{th} percentile were considered as outliers and removed.

Mast	Sector (°)	Sensor h. (H)	N	$\frac{\overline{u'v'}}{u_*^2}$	$\frac{\overline{u'w'}}{u_*^2}$	$\frac{\overline{v'w'}}{u_*^2}$
HalsaW	150-180	50	170	-0.87±1.08	-0.91±0.18	-0.20±0.31
		31	155	-0.78±1.03	-0.92±0.15	-0.21±0.29
		12	114	-0.35±0.51	-0.93±0.14	-0.25±0.24
	285-360	50	27	0.46±1.13	-0.93±0.17	0.11±0.31
		31	24	0.32±2.25	-0.96±0.07	0.16±0.24
		12	21	0.29±2.62	-0.90±0.09	0.28±0.34
HalsaE	150-180	48	199	0.68±1.16	-0.89±0.18	-0.02±0.41
		31	172	0.98±1.18	-0.92±0.15	-0.08±0.36
	210-285	48	33	0.15±0.84	-0.96±0.07	0.15±0.24
		31	19	-0.13±1.10	-0.87±0.12	0.33±0.34
	300-360	48	43	-0.20±1.50	-0.86±0.27	-0.20±0.39
		31	31	-0.67±2.10	-0.84±0.35	-0.18±0.39
JulW	120-195	68	96	-1.72±1.71	-0.35±0.53	-0.61±0.49
		52	192	-1.77±1.50	-0.46±0.43	-0.63±0.46
		32	198	-1.90±1.49	-0.48±0.39	-0.65±0.43
	330-360	68	45	0.52±0.73	-0.76±0.28	0.53±0.26
		52	92	0.58±0.60	-0.74±0.26	0.56±0.27
		32	74	0.77±0.54	-0.65±0.20	0.69±0.25
JulE	120-195	50	97	0.51±1.67	-0.86±0.18	-0.27±0.41
		31	102	0.38±1.63	-0.81±0.18	-0.41±0.37
		12	5	-0.83±0.53	-0.67±0.49	-0.54±0.41
	210-285	50	111	0.10±1.08	-0.74±0.38	0.26±0.49
		31	110	0.14±1.76	-0.76±0.37	0.01±0.54
		12	49	0.83±2.86	-0.66±0.32	0.62±0.28
	300-360	50	91	0.18±1.63	-0.93±0.15	-0.16±0.28
		31	91	0.01±1.91	-0.98±0.04	0.03±0.20
		12	75	-0.00±1.56	-0.96±0.07	0.18±0.19

References

[1] Samferdselsdepartementet, National Transport Plan 2014 - 2023 (English version), Tech. Rep. Meld. St. 26 (2012 - 2013) Report to the Storting (White Paper)., Norwegian Ministry of transport and communications, Oslo, Norway (2013).

[2] R. H. Scanlan, The action of flexible bridges under wind, II: Buffeting theory, *Journal of Sound and Vibration*, 60:201–211 (1978).

[3] A. G. Davenport, The spectrum of horizontal gustiness near the ground in high winds, *Quarterly Journal of the Royal Meteorological Society*, 87:194–211 (1961).

[4] D. Delaunay, G. Grillaud, Field measurements of the wind-induced response of a cable stayed bridge: Validation of previsional studies, *Journal of Wind Engineering and Industrial Aerodynamics*, 74-76:883–890 (1998).

[5] E. Cheynet, J. B. Jakobsen, J. Snæbjörnsson, Buffeting response of a suspension bridge in complex terrain, *Engineering Structures*, 128:474–487 (2016).

[6] P. L. Jackson, D. G. Steyn, P. L. Jackson, D. G. Steyn, Gap winds in a fjord. Part I: Observations and numerical simulation, *Monthly Weather Review*, 122:2645–2665 (1994).

[7] A. D. Sandvik, K. Harstveit, Study of a down slope windstorm over Southern Norway, Rjukan, 16. January 2000, Tech. Rep. no. 18/2005, Norwegian Meterological Institute (2005).

[8] S. Grønås, A. D. Sandvik, Numerical simulations of local winds over steep orography in the storm over north Norway on October 12, 1996, *Journal of Geophysical Research: Atmospheres*, 104:9107–9120 (1999).

[9] H. Ágústsson, H. Ólafsson, Mean gust factors in complex terrain, *Meteorologische Zeitschrift*, 13:149–155 (2004).

[10] M.-V. Guarino, M. A. C. Teixeira, M. H. P. Ambaum, Turbulence generation by mountain wave breaking in flows with directional wind shear, *Quarterly Journal of the Royal Meteorological Society*, 142:2715–2726 (2016).

[11] C. Sacré, D. Delaunay, Structure spatiale de la turbulence au cours de vents forts sur differents sites, *Journal of Wind Engineering and Industrial Aerodynamics*, 41:295–303 (1992).

[12] J. Bietry, D. Delaunay, E. Conti, Comparison of full-scale measurement and computation of wind effects on a cable-stayed bridge, *Journal of Wind Engineering and Industrial Aerodynamics*, 57:225–235 (1995).

[13] M. Hui, A. Larsen, H. Xiang, 20091wind turbulence characteristics study at the Stonecutters bridge site: Part –I mean wind and turbulence intensities, *Journal of Wind Engineering and Industrial Aerodynamics*, 97:22–36 (2009).

[14] M. Hui, A. Larsen, H. Xiang, 20092 wind turbulence characteristics study at the Stonecutters bridge site: Part – II wind power spectra, integral length scales and coherences, *Journal of Wind Engineering and Industrial Aerodynamics*, 97:48–59 (2009).

[15] E. Cheynet, J. B. Jakobsen, J. Snæbjörnsson, N. Angelou, T. Mikkelsen, M. Sjöholm, B. Svardal, Full-scale observation of the flow downstream of a suspension bridge deck, *Journal of Wind Engineering and Industrial Aerodynamics*, 171:261–272 (2017).

[16] A. Fenerci, O. Øiseth, A. Rønnquist, Long-term monitoring of wind field characteristics and dynamic response of a long-span suspension bridge in complex terrain, *Engineering Structures*, 147:269–284 (2017).

[17] A. Fenerci, O. Øiseth, Site-specific data-driven probabilistic wind field modeling for the wind-induced response prediction of cable-supported bridges, *Journal of Wind Engineering and Industrial Aerodynamics*, 181:161–179 (2018).

[18] A. Fenerci, O. Øiseth, Strong wind characteristics and dynamic response of a long-span suspension bridge during a storm, *Journal of Wind Engineering and Industrial Aerodynamics*, 172:116–138 (2018).

[19] N. Jensen, E. Hjort-Hansen, Dynamic excitation of structures by wind–turbulence and response measurements at the Sotra Bridge, Tech. Rep. SINTEF Report No. STF71 A78003, Trondheim-NTH, Norway (1977).

[20] K. Harstveit, Full scale measurements of gust factors and turbulence intensity, and their relations in hilly terrain, *Journal of Wind Engineering and Industrial Aerodynamics*, 61:195–205 (1996).

[21] E. Cheynet, J. B. Jakobsen, J. Snæbjörnsson, Flow distortion recorded by sonic anemometers on a long-span bridge: Towards a better modelling of the dynamic wind load in full-scale, *Journal of Sound and Vibration*, 450:214–230 (2019).

[22] T. Ishihara, K. Hibi, S. Oikawa, A wind tunnel study of turbulent flow over a three-dimensional steep hill, *Journal of Wind Engineering and Industrial Aerodynamics*, 83:95–107 (1999).

[23] B. R. Furevik, H. Ágústson, A. Lauen Borg, M. Zakari, F. Nyhammer, M. Gausen, Meteorological observations in tall masts for mapping of atmo-

spheric flow in Norwegian fjords, *Earth System Science Data Discussions*, pp. 1–28 (2020).

[24] U. NCAR, Weather Research and Forecasting Model — MMM: Mesoscale & Microscale Meteorology Laboratory (2020).

[25] H. Ágústsson, B. R. Broe, M. E. Hoem, Analysis of wind measurements from 6 masts at Sulafjorden 24.11.2016-31.03.2020, Tech. Rep. KVT/HA/2020/R046, Kjeller Vindteknikk, Norconsult (2020).

[26] O. K. Eriksen, E39, brukrysninger Julsundet og Halsafjorden, Møre og Romsdal - Statusrapport for vindmålinger pr desember 2019, Tech. Rep. KVT/OKE/2020/R012, Kjeller Vindteknikk, Norconsult (2020).

[27] J. M. Wilczak, S. P. Oncley, S. A. Stage, Sonic anemometer tilt correction algorithms, *Boundary-Layer Meteorology*, 99:127–150 (2001).

[28] H. J. Oldroyd, E. R. Pardyjak, H. Huwald, M. B. Parlange, Adapting tilt corrections and the governing flow equations for steep, fully three-dimensional, mountainous terrain, *Boundary-Layer Meteorology*, 159:539–565 (2016).

[29] I. Stiperski, M. W. Rotach, On the Measurement of Turbulence Over Complex Mountainous Terrain, *Boundary-Layer Meteorology*, 159:97–121 (2016).

[30] C. Klipp, Turbulent friction velocity calculated from the Reynolds stress Tensor, *Journal of the Atmospheric Sciences*, 75:1029–1043 (2018).

[31] G. L. Geernaert, Measurements of the angle between the wind vector and wind stress vector in the surface layer over the North Sea, *Journal of Geophysical Research*, 93:8215 (1988).

[32] O. Zeman, N. O. Jensen, Modification of turbulence characteristics in flow over hills, *Quarterly Journal of the Royal Meteorological Society*, 113:55–80 (1987).

[33] S. Cao, Strong winds and their characteristics, in *Tamura Y., Kareem A. (eds) Advanced Structural Wind Engineering*, Springer, Tokyo, 2013, pp. 1–25.

[34] R. B. Stull, *An Introduction to Boundary Layer Meteorology*, Kluwer Academic Publishers, Dordrecht, Netherland, 1988.

[35] J. C. Kaimal, J. J. Finnigan, *Atmospheric Boundary Layer Flows: Their Structure and Measurement*, Oxford University Press, 1994.

[36] R. O. Weber, Remarks on the definition and estimation of friction velocity, *Boundary-Layer Meteorology*, 93:197–209 (1999).

[37] M. W. Rotach, M. Andretta, P. Calanca, A. P. Weigel, A. Weiss, Boundary layer characteristics and turbulent exchange mechanisms in highly complex terrain, *Acta Geophysica*, 56:194–219 (2008).

[38] L. Mahrt, Surface wind direction variability, *Journal of applied meteorology and climatology*, 50:144–152 (2011).

[39] C. L. Klipp, M. Adelphi, A new scaling term for use in roughness sublayers, in *18th Symp. on Boundary Layers and Turbulence, Stockholm, Sweden (9-13 June 2008)*, American Meteorological Society, 2008.

[40] B. Furevik, H. Ágústsson, A. L. Borg, F. Nyhammer, The E39 coastal highway observational dataset – atmospheric flow in complex coastal terrain in Mid-Norway, Tech. rep., Norwegian Meteorological Institute (2019).

[41] EN 1991-1-4, Eurocode 1. Actions on structures – Part 1-4: General actions – Wind actions., Tech. rep., [Authority: The European Union Per Regulation 305/2011, Directive 98/34/EC, Directive 2004/18/EC] (2005).

[42] M. Repetto, G. Solari, Wind-induced fatigue of structures under neutral and non-neutral atmospheric conditions, *Journal of Wind Engineering and Industrial Aerodynamics*, 95:1364–1383 (2007).

[43] R. Barthelmie, The effects of atmospheric stability on coastal wind climates, *Meteorological Applications: A journal of forecasting, practical applications, training techniques and modelling*, 6:39–47 (1999).

[44] A. Sathe, S.-E. Gryning, A. Peña, Comparison of the atmospheric stability and wind profiles at two wind farm sites over a long marine fetch in the North Sea, *Wind Energy*, 14:767–780 (2011).

[45] E. Cheynet, J. B. Jakobsen, J. Reuder, Velocity spectra and coherence estimates in the marine atmospheric boundary layer, *Boundary-Layer Meteorology*, 169:429–460 (2018).

[46] L. Kristensen, N. O. Jensen, Lateral coherence in isotropic turbulence and in the natural wind, *Boundary-Layer Meteorology*, 17:353–373 (1979).

[47] A. Golzio, I. M. Bollati, S. Ferrarese, An assessment of coordinate rotation methods in sonic anemometer measurements of turbulent fluxes over complex mountainous terrain, *Atmosphere*, 10:324 (2019).

[48] D. Vickers, L. Mahrt, Quality control and flux sampling problems for tower and aircraft data, *Journal of Atmospheric and Oceanic Technology*, 14:512–526 (1997).

[49] J. C. Wyngaard, On the surface-layer turbulence, in *Workshop on micrometeorology, Boston, USA*, American Meteorological society, 1973, pp. 101–149.

[50] A. G. Davenport, The application of statistical concepts to the wind loading of structures., *Proceedings of the Institution of Civil Engineers*, 19:449–472 (1961).

[51] E. Cheynet, J. Jakobsen, J. Snæbjörnsson, H. Ágústsson, K. Harstveit, Complementary use of wind lidars and land-based met-masts for wind measurements in a wide fjord, *JPhCS*, 1104:012028 (2018).

[52] A. P. Morse, B. A. Gardiner, B. J. Marshall, Mechanisms controlling turbulence development across a forest edge, *Boundary-Layer Meteorology*, 103:227–251 (2002).

[53] A. Fenerci, O. Øiseth, Measured buffeting response of a long-span suspension bridge compared with numerical predictions based on design wind spectra, *Journal of Structural Engineering*, 143:04017131 (2017).

[54] T. Argentini, D. Rocchi, C. Somaschini, Effect of the low-frequency turbulence on the aeroelastic response of a long-span bridge in wind tunnel, *Journal of Wind Engineering and Industrial Aerodynamics*, 197:104072 (2020).

[55] G. Diana, D. Rocchi, T. Argentini, S. Muggiasca, Aerodynamic instability of a bridge deck section model: Linear and nonlinear approach to force modeling, *Journal of Wind Engineering and Industrial Aerodynamics*, 98:363–374 (2010).

[56] G. Diana, S. Omarini, A non-linear method to compute the buffeting response of a bridge validation of the model through wind tunnel tests, *Journal of Wind Engineering and Industrial Aerodynamics*, 201:104163 (2020).

[57] R. Frost, Atmospheric turbulence, *Quarterly Journal of the Royal Meteorological Society*, 74:316–338 (1948).

[58] J. S. Touma, Dependence of the wind profile power law on stability for various locations, *Journal of the Air Pollution Control Association*, 27:863–866 (1977).

[59] J. S. Irwin, A theoretical variation of the wind profile power-law exponent as a function of surface roughness and stability, *Atmospheric Environment (1967)*, 13:191–194 (1979).

[60] A. S. Monin, A. M. Obukhov, Basic laws of turbulent mixing in the surface layer of the atmosphere, *Proceedings of the Geophysical Institute USSR Academy of Sciences*, 24:163–187 (1954).

[61] S. Hsu, E. A. Meindl, D. B. Gilhousen, Determining the power-law wind-profile exponent under near-neutral stability conditions at sea, *Journal of Applied Meteorology*, 33:757–765 (1994).

[62] Y. Tamura, Y. Iwatani, K. Hibi, K. Suda, O. Nakamura, T. Maruyama, R. Ishibashi, Profiles of mean wind speeds and vertical turbulence intensities measured at seashore and two inland sites using Doppler sodars, *Journal of Wind Engineering and Industrial Aerodynamics*, 95:411–427 (2007).

[63] P. S. Jackson, J. C. R. Hunt, Turbulent wind flow over a low hill, *Quarterly Journal of the Royal Meteorological Society*, 101:929–955 (1975).

[64] D. Karmakar, S. Ray-Chaudhuri, M. Shinozuka, Conditional simulation of non-Gaussian wind velocity profiles: Application to buffeting response of Vincent Thomas suspension bridge, *Probabilistic Engineering Mechanics*, 29:167–175 (2012).

[65] A. a. Kareem, M. Tognarelli, K. Gurley, Modeling and analysis of quadratic term in the wind effects on structures, *Journal of Wind Engineering and Industrial Aerodynamics*, 74:1101–1110 (1998).

[66] K. Gurley, A. Kareem, Analysis interpretation modeling and simulation of unsteady wind and pressure data, *Journal of Wind Engineering and Industrial Aerodynamics*, 69-71:657–669 (1997).

[67] P. Fernández-Cabán, F. Masters, Near surface wind longitudinal velocity positively skews with increasing aerodynamic roughness length, *Journal of Wind Engineering and Industrial Aerodynamics*, 169:94–105 (2017).

[68] J. Yuan, M. A. Jouybari, Topographical effects of roughness on turbulence statistics in roughness sublayer, *Physical Review Fluids*, 3:114603 (2018).

[69] J. Wieringa, Updating the Davenport roughness classification, *Journal of Wind Engineering and Industrial Aerodynamics*, 41:357–368 (1992).

[70] T. M. Lystad, A. Fenerci, O. Øiseth, Evaluation of mast measurements and wind tunnel terrain models to describe spatially variable wind field characteristics for long-span bridge design, *Journal of Wind Engineering and Industrial Aerodynamics*, 179:558–573 (2018).

[71] M. de Franceschi, D. Zardi, M. Tagliazucca, F. Tampieri, Analysis of second-order moments in surface layer turbulence in an Alpine valley, *Quarterly Journal of the Royal Meteorological Society*, 135:1750–1765 (2009).

[72] H. Panofsky, D. Larko, R. Lipschutz, G. Stone, E. Bradley, A. J. Bowen, J. Højstrup, Spectra of velocity components over complex terrain, *Quarterly Journal of the Royal Meteorological Society*, 108:215–230 (1982).

[73] H. P. Frank, A simple spectral model for the modification of turbulence in flow over gentle hills, *Boundary-Layer Meteorology*, 79:345–373 (1996).

[74] J. Mann, Spectral velocity tensor in moderately complex terrain, *Journal of Wind Engineering and Industrial Aerodynamics*, 88:153–169 (2000).

[75] G. Solari, G. Piccardo, Probabilistic 3-D turbulence modeling for gust buffeting of structures, *Probabilistic Engineering Mechanics*, 16:73–86 (2001).

[76] Norwegian Public Road Administration, *N400 Handbook for Bridge Design*, Directorate of Public Roads (2015).

[77] J. C. Kaimal, J. C. Wyngaard, Y. Izumi, O. R. Coté, Spectral characteristics of surface-layer turbulence, *Quarterly Journal of the Royal Meteorological Society*, 98:563–589 (1972).

[78] E. Cheynet, J. B. Jakobsen, C. Obhrai, Spectral characteristics of surface-layer turbulence in the north sea, *Energy Procedia*, 137:414–427 (2017).

[79] O. Øiseth, A. Rönnquist, R. Sigbjörnsson, Effects of co-spectral densities of atmospheric turbulence on the dynamic response of cable-supported bridges: a case study, *Journal of Wind Engineering and Industrial Aerodynamics*, 116:83–93 (2013).

[80] Gill Instruments, Technical Key Note KN1509v3* (2016).

[81] D. P. Billesbach, S. W. Chan, D. R. Cook, D. Papale, R. Bracho-Garrillo, J. Verfallie, R. Vargas, S. C. Biraud, Effects of the gill-solent windmaster-pro w-boost firmware bug on eddy covariance fluxes and some simple recovery strategies, *Agricultural and Forest Meteorology*, 265:145–151 (2019).

[82] J. C. Hunt, J. F. Morrison, Eddy structure in turbulent boundary layers, *European Journal of Mechanics-B/Fluids*, 19:673–694 (2000).

[83] J. C. Hunt, P. Carlotti, Statistical structure at the wall of the high Reynolds number turbulent boundary layer, *Flow, Turbulence and Combustion*, 66:453–475 (2001).

[84] U. Högström, J. Hunt, A.-S. Smedman, Theory and measurements for turbulence spectra and variances in the atmospheric neutral surface layer, *Boundary-Layer Meteorology*, 103:101–124 (2002).

[85] A. J. Bowen, R. G. Flay, H. A. Panofsky, Vertical coherence and phase delay between wind components in strong winds below 20 m, *Boundary-Layer Meteorology*, 26:313–324 (1983).

[86] E. Cheynet, Influence of the measurement height on the vertical coherence of natural wind, in *Conference of the Italian Association for Wind Engineering*, Springer, 2018, pp. 207–221.

Paper II

Part II – Spectral flow characteristics

Zakari Midjiyawa, Etienne Cheynet, Joachim Reuder, Hálfdán Ágústsson, and Trond Kvamsdal

Published in *Journal of Wind Engineering and Industrial Aerodynamic* (2021) **211**:104585

Potential and challenges of wind measurements using met-masts in complex topography for bridge design: Part II – Spectral flow characteristics

Zakari Midjiyawa[1,2,*], Etienne Cheynet[3], Joachim Reuder[3], Hálfdán Ágústsson[4], Trond Kvamsdal[2]

[1] *Norwegian Meteorological Institute, Henrik Mohns Plass 1, 0313 Oslo, Norway*
[2] *Department of Mathematical Sciences, Norwegian University of Science and Technology, Alfred Getz' vei 1, 7491 Trondheim, Norway*
[3] *Geophysical Institute and Bergen Offshore Wind Centre, University of Bergen, Allegaten 70, 5007 Bergen, Norway*
[4] *Kjeller Vindteknikk, Norconsult AS, Tærudgata 16, Lillestrøm, Norway*

Abstract

This study quantifies the influence of the local topography on sonic anemometer measurements mounted on tall met-masts deployed in Norwegian fjords. This assessment is done by analysing the second-order structure of turbulence in the frequency space. The objective is to evaluate how the data collected by these masts can help with the design of future fjord-crossing bridges. Using measurements from eight masts deployed in three different fjords, spectral characteristics common to the different locations were identified. Among the characteristics investigated, the one-point velocity spectra and the vertical coherence of turbulence are of special interest for bridge design. Using only situations with a mean wind speed of $12\,\mathrm{m\,s^{-1}}$ and above and rather stationary flow conditions, the remaining wind direction sectors could be classified into two main groups: those with a long fetch over smooth topography and those with a rough heterogeneous terrain upstream of the masts. It was found that if the velocity spectra are normalized by an appropriate estimate of the friction velocity, surface-layer scaling may be applicable in Norwegian fjords, at least under near-neutral conditions. The velocity spectra, estimated with long upstream fjord fetches have characteristics consistent with those collected in coastal and offshore environments. The Davenport model showed limited capabilities in describing the co-coherence of turbulence on vertical separations. The dependency of the Davenport decay coefficient with the height and spatial separation is highlighted and may be substantial in mountainous terrain. Although the spectral flow characteristics estimated on the shore of fjords are relevant for the design of fjord-crossing bridge towers, they may not easily be extrapolated for the modelling of the turbulent flow in the middle of the fjord. Nevertheless, they are still valuable to complement computational fluid dynamic

simulations, wind tunnel tests, or remote sensing of wind across the fjord.

1. Introduction

The characterization of the wind conditions in fjords by tall met-masts can be particularly challenging. [1] showed, for example, that high wind speeds are often recorded for only a limited number of narrow sectors and that the flow characteristics at the mast locations might differ significantly from those in the middle of the fjord.

However, the local topography may not equally affect eddies of different sizes. Deviations of the estimated integral flow characteristics from those in flat terrain were observed in [1]. These may be linked to a perturbation of the low-frequency turbulence fluctuations by the local terrain while the high-frequency range may remain less affected [2]. An investigation of the spectral structure of turbulence is, therefore, vital to identify to what extend the records from the masts on the shore can be used to model the velocity spectra and coherence of turbulence above the water in narrow fjords. The present paper complements the study by [1] by focusing on the second-order spectral characteristics of turbulence, which is relevant for the design of long-span bridges.

The one-point spectrum and coherence are fundamental to calculate turbulent wind loading on long-span bridges [3, 4]. Full-scale studies, focusing on the spectral characteristics of turbulence for bridge design, are typically site-specific [5–9]. Whereas turbulence characteristics in complex terrain are undoubtedly affected by the local topography, there may exist common features between multiple sites in a specific type of topography, for example, a fjord. Identifying such shared features is thus of major interest when modelling the dynamic wind load on fjord-crossing bridges. In this regard, a systematic characterization of turbulence from multiple sites is desirable, but unfortunately rarely done.

As the need for long-span bridges in mountainous environments increases (table 1), turbulence spectra and coherence models appropriate to model the dynamic wind load in rough terrains are required. One-point spectral models [10–14] and coherence models [4] commonly found in the literature were originally established in flat and homogeneous topographies. Their applicability in mountainous terrain, as in fjords, is still unclear.

This paper's aim is to identify potential common features of turbulence in the frequency space by focusing on two sectors in each fjord, characterized by converse flow conditions: long-fetch winds, defined as winds blowing over an extended stretch of water, typically more than two kilometres; and short-fetch winds,

---

[*] Corresponding author.

Email addresses: `midjiyawaz@met.no` (Z. Midjiyawa).

Table 1: Long-span cable-suspended bridges built in mountainous terrain (main span larger than 600 m).

Year	Name	Main span (m)	Location
2020	Jinshajiang Hutiaoxia Bridge	766	China
2020	Honghe Jianyuan Bridge	700	China
2020	Jin'an Bridge	1386	China
2018	Xingkang Bridge	1100	China
2018	Chajiaotan Bridge	1200	China
2018	Hålogaland Bridge	1145	Norway
2018	Sunxihe Bridge	660	China
2016	Longjiang River Bridge	1196	China
2016	Yachi Bridge	800	China
2016	Duge Bridge	720	China
2015	Qingshui River Bridge	1130	China
2015	Puli Bridge	628	China
2013	Hardanger Bridge	1310	Norway
2013	Lishui River Bridge	856	China
2012	Aizhai Bridge	1176	China
2009	Sidu River Bridge	900	China
2009	Baling River Bridge	1088	China
2009	Beipanjiang River Bridge	636	China
1992	Gjemnessund Bridge	623	Norway

defined as winds blowing over irregular and heterogeneous terrain upstream of the measurement location. Furthermore, the study aims at exploring the variation of the co-coherence of turbulence between the different fjords. It also reassesses the applicability of the widely used Davenport model in complex topography.

The rest of the paper is organized as follows; Section 2 discusses the choice of scaling velocity and length in the surface layer. The section further introduces the different co-coherence models. Section 4 presents the methods and assumptions used in the estimation of velocity spectra and co-coherence. Section 5 discusses the influence of topography on the velocity spectra and spectral ratios as well as on the spatial correlation of turbulence.

2. Fundamentals of turbulence and turbulence-induced wind load

2.1. *Choice of the scaling velocity and scaling length*

As in [1], atmospheric turbulence is modelled as a three-variate, three-dimensional correlated random process $\{u, v, w\}$ in a coordinate system $\{x, y, z\}$, where x, y and z denote the along-wind, cross-wind and vertical directions, respectively.

In both wind engineering and micro-meteorology, the velocity spectra are scaled by a characteristic length and velocity. Following Monin-Obukhov Similarity Theory (MOST) [15], the scaling velocity is the friction velocity u_*, whereas the scaling length is the height z above the ground. MOST is applicable only in the surface layer, i.e. roughly the lower 10% of the atmospheric boundary layer. Although u_* and z are sporadically used in wind engineering [14], other characteristic lengths and velocity scaling are more common. In [16] or [17], the spectrum of the along-wind velocity component is of special interest. For this component, the scaling velocity is the standard deviation of the along-wind component σ_u, whereas the scaling length is the integral length scale L_u^x, which is modelled as a non-linear function of z.

Following [16], the use of L_u^x aims to account for the inadequacy of MOST at altitudes above 50 m, which is a reasonable motivation. However, the literature supporting the use of the integral length scale as scaling length is rather scarce, while full-scale measurements indicated that, under neutral conditions, z is still appropriate at heights above 80 m above the surface [18, 19]. Although the integral length scale is a key characteristic in wind-tunnel tests, the full-scale estimation of the integral length scale is prone to significant error and its usefulness in full-scale is thus questionable [20]. The integral length scales are used in the von Kármán spectrum [13, 21] and the ESDU spectrum model [22]. However, the length scale is reliable only if the spectral peak is clearly defined [19], which is rarely the case in full-scale, especially close to the ground, where the spectral peak can be flat [23]. Natural wind includes also a combination of submeso-, meso- and microscale fluctuations, which are not accounted for in wind tunnel tests or spectral tensor models [24]. And this complexity challenges the estimation of the integral length scale. The large uncertainties associated with the estimation of the integral length scales in Norwegian fjords implies that the von Kármán spectrum is not discussed herein. Besides, in the upper part of the atmospheric boundary layer, the thickness of the boundary layer acts as the scaling length [23], such that the turbulence spectrum is independent of the altitude, meaning that both z and L_u^x become inappropriate above a given height. In the present case, the simultaneous presence of mountains and the sea challenge the choice of an adequate boundary layer height. As the measurements were conducted in the first 100 m above the ground, it was decided to use z as a scaling length.

In the inertial subrange, [11] derived some asymptotic relations for the normalized power spectral densities (PSDs) of the three velocity components

$$\frac{fS_u(f)}{u_*^2} \rightarrow 0.3 f_r^{-2/3} \text{ at } f_r \gg 1 \tag{1}$$

$$\frac{fS_v(f)}{u_*^2} \approx \frac{fS_w(f)}{u_*^2} \rightarrow 0.4 f_r^{-2/3} \text{ at } f_r \gg 1 \tag{2}$$

$$f_r = \frac{fz}{u} \tag{3}$$

where S_u, S_v and S_w are the along-wind, crosswind and vertical velocity spectra, respectively; f is the frequency and $\overline{u}$ is the horizontal mean wind speed. Eqs. (1) and (2) satisfy the hypothesis of local isotropy in the inertial subrange [25]

$$\frac{S_w}{S_u} \approx \frac{S_v}{S_u} \rightarrow \frac{4}{3} \text{ at } f_r \gg 1 \tag{4}$$

Eqs. (1) and (2) are of major importance to assess the quality of the anemometer records, for example, to know if flow distortion occurs [26, 27]. The ratios S_w/S_u and S_v/S_u can also be affected by aliasing if the velocity data are recorded with a relatively low sampling frequency or if the data have been decimated without application of a low-pass filter. Failure to satisfy Eq. (4) may also indicate that the inertial subrange has not yet been reached by the S_w or S_v spectrum because of the limited sampling frequency or the sonic-path averaging of the anemometer [28].

Using u_* as the velocity scale together with a logarithmic mean wind speed profile implies that the turbulence intensity is not explicitly used to compute the wind load. For a given velocity spectrum, the turbulence intensity can be modified by changing the roughness length z_0 or the reference mean wind speed $\overline{u}_{ref}$ at a reference height z_{ref}. Therefore, the along-wind dynamic wind load in one point can be modelled using only five parameters: $\{u_*, z_0, u_{ref}, z_{ref}, fS_u/u_*^2\}$, where fS_u/u_*^2 can be derived from [11], [14] or [12].

The friction velocity requires knowledge of the three velocity components and is associated with a larger statistical uncertainty than their standard deviation. The standard deviation of the along-wind velocity σ_u, may, therefore, appear as an attractive alternative velocity scale. Nevertheless, the use of σ_u requires an additional relation between u_* and σ_u, which is often approximated as $\sigma_u = Ku_*$ where K is a coefficient which depends on the terrain roughness [14, 29]. This makes the relation between σ_u and u_* prone to large uncertainties in mountainous regions [1, 30]. If surface-layer scaling is adopted, turbulence modelling with σ_u as scaling velocity leads to more parameters than necessary to compute the wind load. Besides, if the relation between σ_u and u_* is not carefully chosen, it is possible to simulate a flow field that does not satisfy Eqs. (1) and (2), which is not desirable for a realistic simulation of an undisturbed turbulence field. In the present case, u_* was chosen as the scaling velocity based on data collected from 3D sonic anemometers and an averaging interval of 30 min was selected to reduce the statistical uncertainties.

The friction velocity is estimated hereafter using three different methods. First is the traditional approach, suggested by e.g. [31]

$$u_{*C} = \left[\overline{u'w'}^2 + \overline{v'w'}^2\right]^{1/4} \tag{5}$$

Second is the method by [32]

$$u_{*R} = \left[(\lambda_1 - \lambda_3)\cos(\beta)\sin(\beta)\right]^{1/2} \tag{6}$$

where λ_1 and λ_3 are the largest and smallest principal components of the Reynolds stress tensor, respectively; β is defined as

$$\beta = 90 - \arccos\left(\frac{U \cdot \Lambda_3}{|U|\,|\Lambda_3|}\right) \tag{7}$$

where Λ_3 is the eigenvector associated to λ_3 and U is the mean wind velocity vector. The third method incorporates also the horizontal covariance term of the Reynolds stress tensor

$$u_{*M} = \left[\overline{u'w'}^2 + \overline{u'v'}^2 + \overline{v'w'}^2\right]^{1/4} \tag{8}$$

The third method may be justified if $\overline{u'v'}$ contributes considerably to the surface stresses. However, Eq. (8) should be interpreted with caution as its expression is not consistent with the properties of the Reynolds stress tensor [33]. Therefore Eq. (8) is considered only when the other two methods to compute the friction velocity result in non-dimensional spectra that do not satisfy Eqs. (1) and (2). Investigating Eq. (8) is valuable to assess the appropriateness of u_* as the scaling velocity in a fjord-like topography.

For comparison purposes, the estimated PSDs are compared to the one-point auto and cross-spectral densities by [34], defined as

$$\frac{fS_u(f)}{u_*^2} = \frac{102 f_r}{(1+33f_r)^{5/3}} \tag{9}$$

$$\frac{fS_v(f)}{u_*^2} = \frac{17 f_r}{(1+9.5f_r)^{5/3}} \tag{10}$$

$$\frac{fS_w(f)}{u_*^2} = \frac{2 f_r}{1+5f_r^{5/3}} \tag{11}$$

$$\frac{f\mathrm{Re}(S_{uw}(f))}{u_*^2} = -\frac{14 f_r}{(1+9.6f_r)^{7/3}} \tag{12}$$

where $\mathrm{Re}(S_{uw}(f))$ refers to the real part of the cross-spectrum. Since the terrain is heterogeneous, the anemometers may be located in different internal boundary layers. Therefore, the friction velocity is unlikely to be constant with the measurement height. Using local similarity theory [35], it is possible to normalize the velocity spectra and cross-spectra based on local estimates of u_* instead of using the value at the lowest height. Following [36], this approach may be suitable in a mountainous environment and is, therefore, adopted in the following.

2.2. ***Surface-layer velocity spectra in complex terrains***

Figure 1 illustrates the fact that, in the surface layer, the maximal value of the normalized along-wind velocity spectrum is $fS_u/u_*^2 \approx 1$ [11, 23]. In the lower part

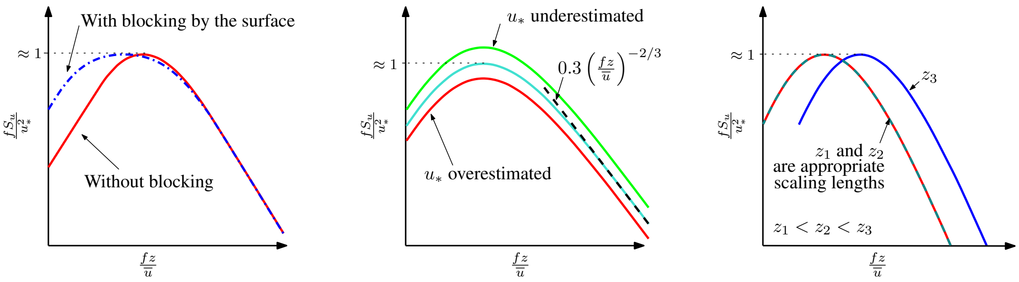

Figure 1: Sketches of the normalized S_u velocity spectra highlighting the influence of the blockage by the surface on the width of the spectral peak (left panel), the value of the friction velocity estimate on the amplitude of the peak (middle panel) and the influence of the scaling length on the frequency at which the peak is reached.

of the surface layer, the strong shear and the blocking by the surface distort the eddies as they impinge and scrap along the surface [23, 37–39]. This phenomenon leads to the distortion of the low-frequency range of the velocity spectrum. In particular, the spectral peak of the velocity spectrum pre-multiplied with the frequency flattens (left panel of fig. 1) to create a plateau [40]. Although the plateau is often observed in the first 30 m above the ground [23], it likely exists at higher altitudes [40]. A practical tool to quantify blocking is to compare the imaginary part and real part of the cross-spectrum S_{uw} [24, 41]. If $\mathrm{Im}(S_{uw})$ is substantially different from zero, the blocking by the surface may not be negligible.

If u_* is the appropriate scaling velocity, an underestimation of its value will lead to a PSD estimate that lies systematically above Eqs. (1) and (2). Such an underestimation can be observed if $u'v'$ substantially affects the turbulent shear stresses. If the altitude above the ground is no longer the adequate scaling length, the peaks of the normalized velocity spectra will be located at different frequencies when expressed as a function of f_r (right panel of fig. 1). In summary, the scaling velocity governs the position of the normalized spectra on the ordinate, whereas the scaling length governs its position on the abscissa.

2.3. Modelling of the co-coherence

The normalized cross-spectrum of turbulence gives the spatial correlation of turbulence in the frequency space [42]. The root-coherence is defined as

$$\gamma_i(z_1, z_2, f) = \frac{S_i(z_1, z_2, f)}{\sqrt{S_i(z_1) S_i(z_2)}} \tag{13}$$

where $i = \{u, v, w\}$; $S_i(z_1)$ and $S_i(z_2)$ are the one-point spectra estimated at heights z_1 and z_2, respectively and $S_i(z_1, z_2, f)$ is the two-point cross-spectral density estimate between the anemometers at the heights z_1 and z_2. Eq. (13) is a complex-valued function, the real part of which is called the co-coherence, whereas its imaginary part is called the quad-coherence.

In wind engineering, wind energy or boundary layer micro-meteorology, the co-coherence is often modelled using the so-called Davenport model [4],

$$\gamma_i(z_1, z_2, f) = \exp\Big(-C^i f_D\Big) \tag{14}$$

$$f_D = \frac{f \mid z_1 - z_2 \mid}{\bar{u}(z_1, z_2)} \tag{15}$$

$$\bar{u}(z_1, z_2) = \frac{\bar{u}(z_1) + \bar{u}(z_2)}{2} \tag{16}$$

where $i = \{u, v, w\}$ and C^i is an empirical decay coefficient. Similarly to the one-point spectrum, the Davenport model was established in flat, and homogeneous terrain and relatively small separation distances. The Davenport model assumes that the decay coefficient (C^i) is constant. In contrast, [43–45] have proposed alternatives approaches of modelling vertical coherence which include the height above the surface. The model by [45] assumes that C^i depends on the height and the vertical separation between anemometers, such that

$$C^i = C_1^i + C_2^i \frac{|z_1 - z_2|}{\overline{z}} \tag{17}$$

$$\overline{z} = \frac{z_1 + z_2}{2}. \tag{18}$$

To account for the fact that the coherence does not equal unity at zero frequency [46], an additional decay parameter C_3^i is introduced in Eq. (17) such that the co-coherence is finally modelled as

$$\gamma_i(z_1, z_2, f) = A(z_1, z_2, f) \cdot \exp\left(-\frac{2C_2^i f \mid z_1 - z_2 \mid^2}{(z_1 + z_2)\bar{u}(z_1, z_2)}\right) \tag{19}$$

$$A(z_1, z_2, f) = \exp\left(-\frac{\mid z_1 - z_2 \mid}{\bar{u}(z_1, z_2)} \sqrt{(C_1^i f)^2 + (C_3^i)^2}\right) \tag{20}$$

The third parameter C_3^i has the dimension of the inverse of a time scale of turbulence. It is lower for the horizontal component compared to the vertical one because the turbulence length scales of the w component are generally smaller than for the u and v components [29]. Furthermore, the introduction of C_3^i reduces the bias in the estimation of C_1^i and C_2^i. Additionally, if the low-frequency records are used without C_3^i, the co-coherence will be equal to 1 when $f = 0\,\mathrm{Hz}$, which is not realistic for large spatial separations. In this study, Eq. (19) is used to illustrate the limits of the Davenport model to describe the vertical co-coherence of turbulence.

3. Observation setup and data processing

The fjords of interest are Sulafjorden, Halsafjorden and Julsundet located on the west coast of Norway. As a part of the E39-project, four masts were deployed in Sulafjorden, two in Halsafjorden and two others in Julsundet [1, 47]. The two masts located on the northern part of Sulafjorden are installed on each side of the fjord and are labelled SulaNW and SulaNE. The masts on the southern area are named SulaSW and SulaSE. On the western and eastern sides of Halsafjorden and Julsundet, the mast deployed are named herein HalsaW/HalsaE and JulW/JulE, respectively. For the sake of brevity, the mast name, heights, types and coordinate location are summarised in table 2. The reader is referred to [47] and [1] for a detailed description of the measurement setup as well as the topography at the mast locations.

Each mast was equipped with three to four 3D sonic anemometers (Gill WindMaster Pro). In total, two years (2018 - 2019) of data from 25 anemometers are used in the current study. The data were saved at a sampling frequency of 10 Hz and pre-processed as described in [1]. The key processing steps were

- Samples with a mean wind speed lower than $12\,\mathrm{m\,s^{-1}}$ were discarded to ensure that the majority of the records are representative of near-neutral conditions.
- The double rotation technique was used for anemometer tilt correction.
- Linear trends were removed to study turbulent fluctuations.
- Highly non-Gaussian, non-stationary fluctuations and samples characterized with high statistical uncertainties in the momentum flux were removed.

4. Methodology for spectral analysis

The selected data were organized into stationary time series of 30 min. The one-point auto and cross-spectral densities of the velocity fluctuations were estimated using Welch's algorithm [48] with a Hanning window and two blocks with 50% overlapping. The use of multiple segments is needed to reduce the bias and the uncertainties associated with the modified periodogram estimate. However, increasing the number of segments reduces also the frequency resolution and increases the lowest frequency recorded. In the present case, two overlapping segments were found to be a reasonable trade-off. The use of 50% overlapping is advised by [49] when a Hanning window is considered. The velocity spectra are ensemble-averaged using arithmetic median for the analysed period and were further smoothed by using bin-averaging over logarithmically-spaced bins, which has the advantage to affect the high-frequency range only. Smoothing filters

Table 2: Overview of the met-masts: Mast acronym, mast location, mast height, mast type, sensor heights, boom orientation, boom length, and coordinate position. Reproduced from [1].

Mast acro.	Mast loc.	Mast h.(m)	Mast type	Sensor h. (m)	Boom orient. (Deg)	Boom l. (m)	Coord.(UTM32)
SulaNW	Kvitneset	100.5	Lattice	92.5, 71.5, 44.5	72, 74, 74	6.1	6924741 N, 345142 E
SulaNE	Trælbodneset	78.0	Lattice	76.8, 48.3, 27.3	289, 290, 290	6.1	6925267 N, 348347 E
SulaSW	Langeneset	97.0	Lattice	94.8, 75.0, 50.0, 27.0	81, 81, 81, 81	4.4	6920740 N, 346520 E
SulaSE	Kårsteinen	63.0	Lattice	62.8, 40.0, 13.4	223, 223, 223	3.6	6922074 N, 351140 E
HalsaW	Halsaneset	50	Tubular	50.3, 31.9, 12.7	106, 106, 104	1.8	6995095 N, 456472 E
HalsaE	Åkvik	50	Lattice	48.3, 31.9, 17.0	227, 227, 227	4	6995697 N, 458519 E
JulW	Nautneset	68	Lattice	68.3, 52.3, 32.7	239, 239, 239	5.1	6957381 N, 394634 E
JulE	Julbo	50	Tubular	50.3, 31.9, 12.7	234, 234, 234	1.8	6957730 N, 396210 E

which distort the low-frequency range of the spectrum, such as the Savitzky-Golay filter [50], may not be adapted for such purpose.

The co-coherence was estimated using Welch's algorithm with ten overlapping segments to smooth the estimates. A larger number of segments than for the one-point spectra is required because the two-point cross-spectrum displays a larger bias and random error. Before computing the co-coherence, the time series were decimated down to 2 Hz to speed-up the algorithm. Also, for the range of vertical separations considered, the co-coherence is nearly zero at frequencies above 1 Hz. The decimation was done after application of a low-pass Chebyshev IIR filter of order eight to reduce aliasing. The estimation of the vertical co-coherence on a single met-mast requires that the data on each sensor passes the data quality assessment described in [1]. This further reduces the amount of data available for the analysis of the co-coherence.

5. Results

5.1. ***Velocity spectra***

The one-point spectra were studied following the wind sectors classification by [1]. The sectors are named long-fetch winds and short-fetch winds as described in section 1. For the sake of clarity, the classification is reproduced in tables 3 and 4 along with their corresponding integral flow characteristics estimated by the anemometer located closest to 50 m above ground.

Using surface-layer scaling, the spectra are normalized by the square of the friction velocity u_{*C} (where c stands for the classical method in Eq. (5)). figs. 2 to 4 and figs. 5 to 7 display the velocity spectra for long-fetch winds and short-fetch winds, respectively. The figures are separated with respect to the three wind components u, v and w. Sectors with less than ten samples were dismissed as they may be associated with statistical uncertainties too large to be meaningful.

Low-frequency part of the velocity spectra

The dynamic wind-induced response of long-span bridges is governed by the low-frequency turbulent wind fluctuations. The planned bridges crossings at Julsundet, Halsafjorden and Sulafjorden will likely have their dominant eigenfrequencies between 0.02 Hz and 0.20 Hz, i.e. possibly lower than those from the the longest suspension bridges in the world [51]. To adequately design such bridges, the large uncertainties associated with the lower-frequency region of the velocity spectra need to be reduced. These uncertainties can be addressed using a probabilistic approach [29, 52] or a more physical approach, which relies on a classification of the topography upstream of the measurement location combined with a rigorous data-quality assessement. The latter method is adopted hereafter since the dataset

Table 3: Normalized standard deviation and turbulence intensity for long-fetch winds. The anemometer closest to 50 m above ground is chosen.

Mast	Sector (°)	σ_w/u_{*C}	σ_v/u_{*C}	σ_u/u_{*C}	σ_w/σ_u	σ_v/σ_u	I_u	I_v	I_w
SulaNW	300-330	1.41±0.19	2.39±0.56	2.09±0.38	0.68±0.10	1.15±0.24	0.08±0.02	0.09±0.03	0.05±0.01
	135-165	1.97±0.34	2.37±0.42	2.62±0.51	0.76±0.09	0.92±0.14	0.13±0.02	0.11±0.02	0.10±0.02
SulaNE	150-210	1.76±0.30	2.81±0.56	2.65±0.51	0.67±0.09	1.07±0.17	0.10±0.02	0.11±0.03	0.07±0.02
	300-20	1.71±0.33	2.35±0.71	2.40±0.52	0.72±0.10	0.97±0.17	0.13±0.03	0.13±0.04	0.09±0.03
HalsaW	150-180	1.42±0.20	2.32±0.42	2.64±0.43	0.54±0.06	0.88±0.12	0.10±0.02	0.09±0.02	0.05±0.01
HalsaE	150-180	1.57±0.29	2.61±0.52	2.91±0.62	0.55±0.05	0.91±0.11	0.11±0.03	0.10±0.02	0.06±0.01
	300-360	1.39±0.27	2.45±0.48	2.55±0.58	0.56±0.08	0.98±0.16	0.17±0.02	0.15±0.03	0.10±0.01
JulW	120-195	1.46±0.29	2.76±0.53	2.62±0.65	0.57±0.10	1.08±0.20	0.09±0.04	0.10±0.04	0.05±0.03
JulE	120-195	1.65±0.27	2.65±0.68	2.74±0.55	0.61±0.11	0.97±0.17	0.11±0.02	0.11±0.03	0.07±0.02
	300-360	1.21±0.13	2.32±0.59	2.25±0.40	0.55±0.08	1.04±0.22	0.10±0.02	0.10±0.03	0.05±0.01

Table 4: Normalized standard deviation and turbulence intensity for short-fetch winds. The anemometer closest to 50 m above ground is chosen.

Mast	Sector (°)	σ_w/u_{*C}	σ_v/u_{*C}	σ_u/u_{*C}	σ_w/σ_u	σ_v/σ_u	I_u	I_v	I_w
SulaNW	165-185	1.98±0.33	1.83±0.35	2.32±0.42	0.85±0.07	0.79±0.07	0.17±0.03	0.13±0.02	0.14±0.02
SulaSW	135-165	1.68±0.24	1.44±0.12	1.81±0.17	0.93±0.12	0.80±0.09	0.22±0.03	0.17±0.03	0.20±0.04
	285-315	1.77±0.24	1.72±0.33	2.19±0.27	0.81±0.07	0.79±0.15	0.18±0.03	0.14±0.04	0.15±0.02
SulaSE	270-330	1.47±0.23	1.96±0.42	2.16±0.38	0.69±0.09	0.92±0.18	0.14±0.04	0.12±0.03	0.10±0.03
HalsaW	285-360	1.52±0.26	2.43±0.70	2.74±0.74	0.57±0.08	0.89±0.12	0.18±0.05	0.16±0.04	0.11±0.04
HalsaE	210-285	1.52±0.17	2.41±0.31	2.61±0.27	0.59±0.05	0.93±0.10	0.17±0.02	0.15±0.03	0.10±0.01
JulW	330-360	1.58±0.23	2.04±0.48	2.51±0.35	0.63±0.08	0.81±0.12	0.15±0.04	0.12±0.03	0.10±0.04
JulE	210-285	1.80±0.32	2.44±0.47	2.84±0.49	0.64±0.05	0.86±0.09	0.18±0.03	0.16±0.03	0.12±0.02

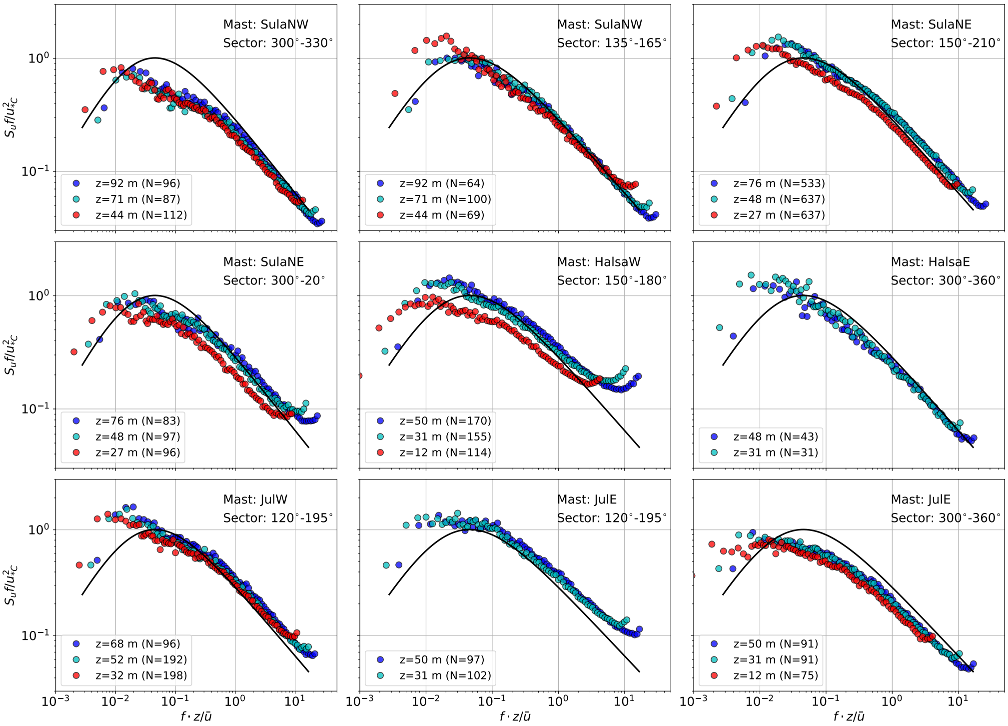

Figure 2: Estimated along-wind velocity spectra for long-fetch winds in Sulafjorden, Halsafjorden and Julsundet, from 01-01-2018 to 31-12-2019. The solid line is the Kaimal spectrum (Eq. (9)).

gives a unique possibility to identify analogous flow characteristics within three different fjords.

The low-frequency spectral content of S_u and S_v, estimated for long-fetch winds, is larger than predicted by the Kaimal model. Furthermore, the spectral peak is moved to the spectrum's lower frequency part. This can be seen, for example, in SulaNW (sector 300°-330°), HalsaE (sector 300°-360°), and JulE (sector 300°-360°). This feature, observed for multiple masts in the selected fjords (figs. 2 and 3) may be one shared spectral characteristic associated with long upstream fjord fetch. On the other hand, for short-fetch winds (figs. 5 and 6) they agree fairly well with the Kaimal spectrum.

The horizontal spectra estimated in SulaNW (sector 135°-165°) and SulaNE (sector 300°-20°) show spectral characteristics compatible with long-fetch winds. However, the calculated integral flow characteristics displayed in table 3 suggest otherwise. The turbulence intensity for both masts and sectors is approximately 0.13 ± 0.03, whereas the normalized standard deviations σ_w/u_* are 1.97 ± 0.34 and 1.71 ± 0.30, respectively. These values are characteristics typically observed

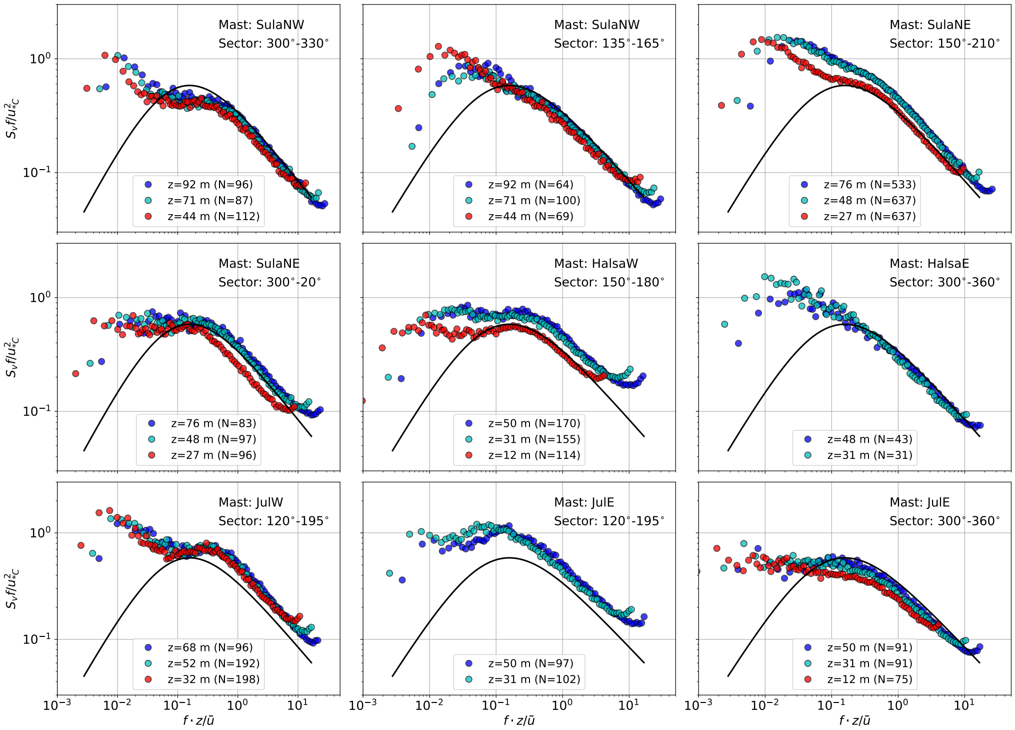

Figure 3: Estimated crosswind velocity spectra for long-fetch winds in Sulafjorden, Halsafjorden and Julsundet, from 01-01-2018 to 31-12-2019. The solid line is the Kaimal spectrum (Eq. (10)).

for short-fetch winds. The inconsistency between integral and spectral flow characteristics indicates that there might be a localized flow from a secondary valley which influences the integral turbulence characteristics [53]. Therefore, further investigation may be required using wind tunnel test or CFD flow simulation.

The vertical spectra S_w reasonably follow surface-layer scaling as they superpose on each other at $f_r < 0.1$. However, the normalized S_w spectra are above the Kaimal model. This is valid for both long-fetch and short-fetch winds (figs. 4 and 7) except for at SulaSE (sector 240°-330°) and SulaSW (sector 135°-165°). The spectral peak of the vertical velocity component is located at higher frequencies than the horizontal components, which reflects the fact that eddies are generally smaller for the w component than for the u and v components [10, 54, 55]. Smaller eddies, located at high wavenumbers, are less affected by the local topography than larger eddies, which may explain why surface-layer scaling seems to apply better to this component.

The low-frequency spectral peak of the horizontal components seen in long-fetch winds, which is more pronounced as the measurement height decreases, was

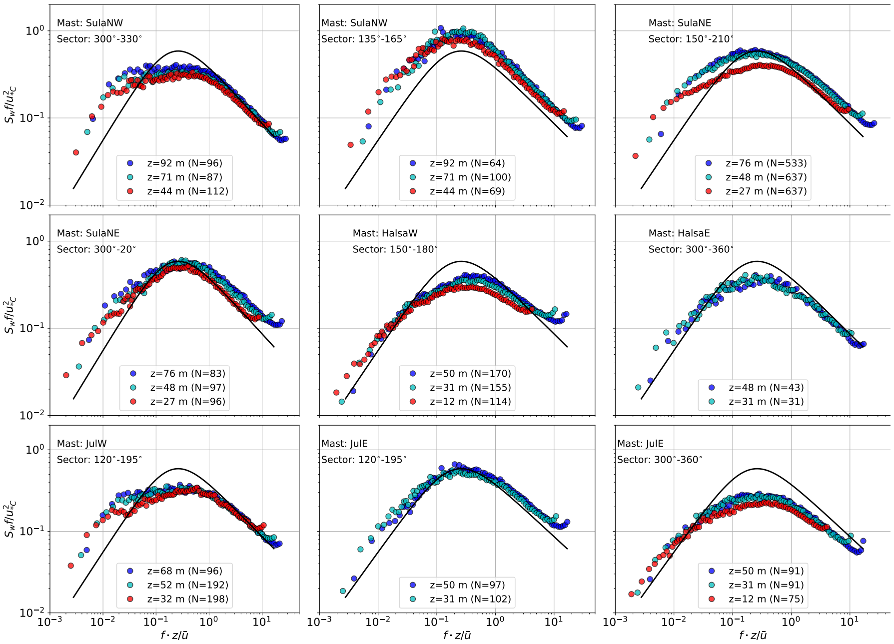

Figure 4: Estimated vertical velocity spectra for long-fetch winds in Sulafjorden, Halsafjorden and Julsundet, from 01-01-2018 to 31-12-2019. The solid line is the Kaimal spectrum (Eq. (11)).

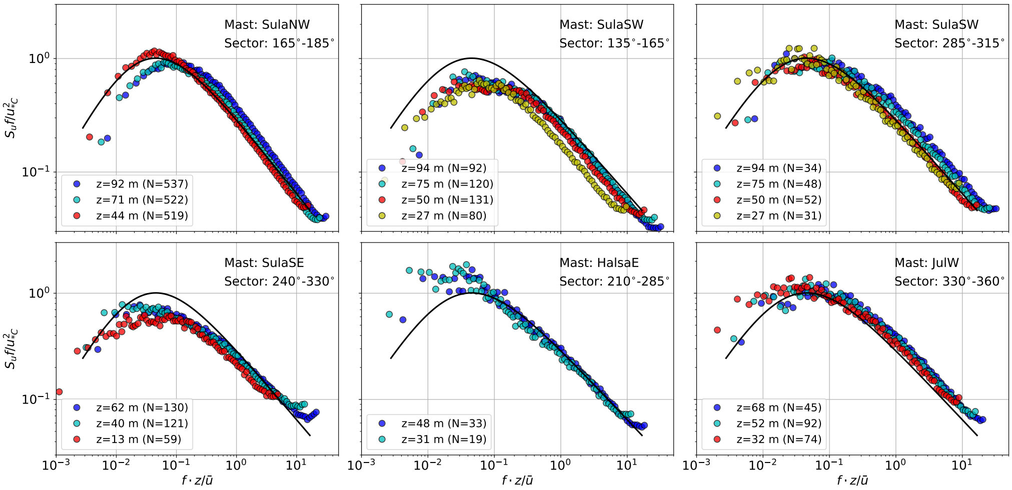

Figure 5: Estimated along-wind velocity spectra for short-fetch winds in Sulafjorden, Halsafjorden and Julsundet, from 01-01-2018 to 31-12-2019. The solid line is the Kaimal spectrum (Eq. (9)).

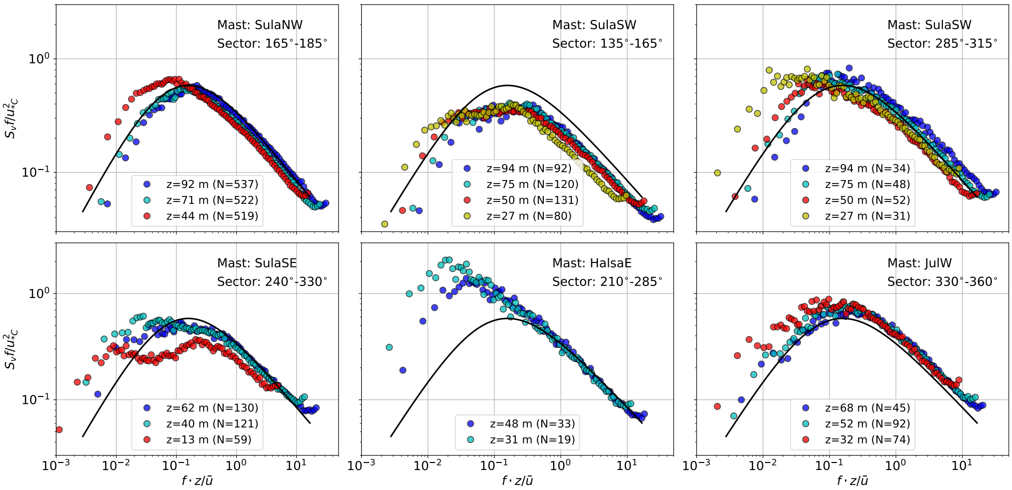

Figure 6: Estimated crosswind velocity spectra for short-fetch winds in Sulafjorden, Halsafjorden and Julsundet, from 01-01-2018 to 31-12-2019. The solid line is the Kaimal spectrum (Eq. (10)).

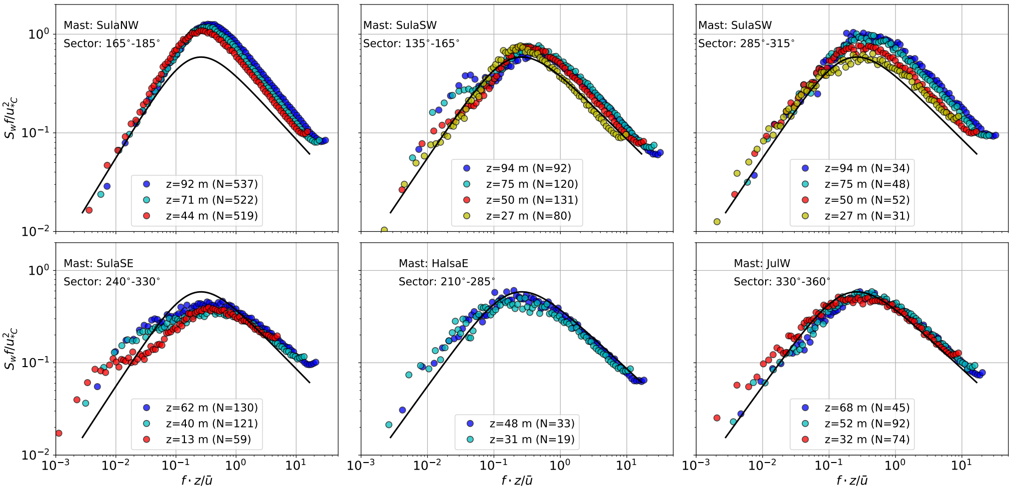

Figure 7: Estimated vertical velocity spectra for short-fetch winds in Sulafjorden, Halsafjorden and Julsundet, from 01-01-2018 to 31-12-2019. The solid line is the Kaimal spectrum (Eq. (11)).

previously observed in coastal areas for a wind coming from the sea [56], but also in the offshore environment [19]. This is likely because S_u and S_v, especially at low frequencies, do not follow MOST [11]. For short-fetch winds, the low-frequency part of the spectrum has a lower spectral energy content than for long-fetch winds. The difference indicates that, although large eddies characterized by low wavenumber could be modified by blocking by the ground, the sea surface or hills [2], the irregular topography may break down the large eddies and, therefore, filter out the low-frequency fluctuations.

For long-fetch winds, the PSD estimates display a double peak, particularly apparent in the cross-wind component (fig. 3). This is the case for SulaNW (sector 300°-330°), SulaNE (sectors 300°-20° and 150°-210°), HalsaW (sector 150°-180°), JulW (sector 120°-195°) and JulE (sectors 120°-195° and 300°-360°). A broad spectral peak, which sometimes looks like a plateau, has also been reported by [40]. For short-fetch winds (figs. 6 and 7), only the sector 240°-330° at SulaSE has a more pronounced spectral plateau for the vertical velocity component and a double peak for the cross-wind component.

Furthermore, the crosswind spectra for JulW (sector 120°-195°) and SulaNW (sector 300°-330°) both show the two most pronounced double peaks. These mast locations and associated wind direction are characterised by wind travelling along the shoreline with mountainous topography on one side and the water inlet on the other. These low-frequency peaks may be due to sub-meso fluctuations. However, it is unsure whether these fluctuations come from topographic elements since similar peaks were observed in offshore environment for the crosswind component [19].

The presence of the spectral plateau may not be limited to the lower part of the surface layer, where blocking by the surface is dominant [40]. Strong shear may also be responsible for a wider spectral peak than predicted in the surface layer, especially for the vertical component [40]. The spectral plateau, when visible, is characterized by $fS_v/u_*^2 \approx 1$ [23]. The aforementioned double peak and spectral plateau are less distinguishable for short-fetch winds which suggest that high-roughness does not seem to favour the distortion of the eddies by the ground but rather act as a high-pass filter.

The semi-empirical models commonly found in the literature [12, 13, 34] rarely account for the presence of a spectral plateau or a double peak. If the von Kármán spectral model [13] is used, the estimation of the integral length scale is generally required. This can be done using the low-frequency range of the velocity spectrum or the spectral peak, which is not always clearly defined. Therefore, the absence of a peak or the presence of multiple peaks can lead to significant errors in the estimation of the integral length scales [19, 20, 57].

High-frequency part of the velocity spectra

The high-frequency range of the velocity spectra is defined as $f_r > 2$ in the following. This range is of lesser importance for the computation of the dynamic displacement of a long-span bridge. However, it is essential to have some confidence in the estimation of the turbulence characteristics. The high-frequency range of the velocity spectrum is characterized by small eddies, which are less affected by the topography. Under neutral conditions, in the surface layer, which are the conditions relevant for structural design, the velocity spectra normalized by f/u_*^2 are expected to satisfy Eqs. (1) and (2). A further quality assessment can be done by comparing the ratios S_w/S_u which should converge toward 4/3 in the inertial subrange [11, 25]. Deviations from these asymptotic relations can be linked to flow-distortion issues, aliasing, nonphysical signal, strong thermal stratification, improper data processing or inadequate method for PSD estimations. Failure to identify the ratio S_w/S_u at high reduced frequencies can lead to a considerable increase of the measurements uncertainties. In this regard, the exploration of the high-frequency part of the velocity spectra offers relevant information on the data quality.

For both long-fetch and short-fetch winds, the normalized S_u and S_v are superposed with each other at $f_r > 2$, except for a limited number of cases e.g SulaNW and the lowest anemometers at the other masts as they may be affected by flow distortion from the surrounding trees. The estimated S_w spectra, in both long-fetch and short-fetch winds, are superposed with each other, as seen for example at JulW (sector 330°-360°) for short-fetch winds and at HalsaE (sector 300°-360°) for long-fetch winds. However, the S_w spectra do not always follow the Kaimal model at higher frequency with the only exception at HalsaE (sector 210°-285°), characterized as short-fetch winds.

The only met-mast in which a consistent collapse is observed with the Kaimal spectrum at a higher frequency for every velocity component is HalsaE, for the sectors 300°-360° and 210°-285°, characterized as long-fetch winds and short-fetch winds, respectively. The HalsaE mast is located in Halsafjorden, where measurements are less influenced by the topography than in the other two fjords [1]. In JulW (sector 120°-195°), characterized as long-fetch winds, the S_w spectrum agrees well with the Kaimal model at high reduced frequencies, whereas it is not the case for the horizontal components.

Following surface-layer scaling, using the friction velocity and the measurement height as the scaling velocity and length, the spectra are expected to superpose onto each other. In this study, S_u, S_v and S_w show the adequacy of surface layer scaling at higher frequency in fjord-like topography. On the other hand, systematic discrepancies with the Kaimal spectrum at high frequencies may indicate that the local friction velocity u_* is biased. The investigation of the alternative methods of computing u_* is done in subsection 5.2.

Influence of topography on the auto- and cross-spectra

The real part of the cross-spectrum, which is called co-spectrum, and its imaginary part, named quad-spectrum herein, are studied for all met-masts and all elevations. For the sake of brevity, fig. 8 shows the normalized cross-spectrum for only two distinctive cases. The mast locations and sectors that are chosen for illustrative

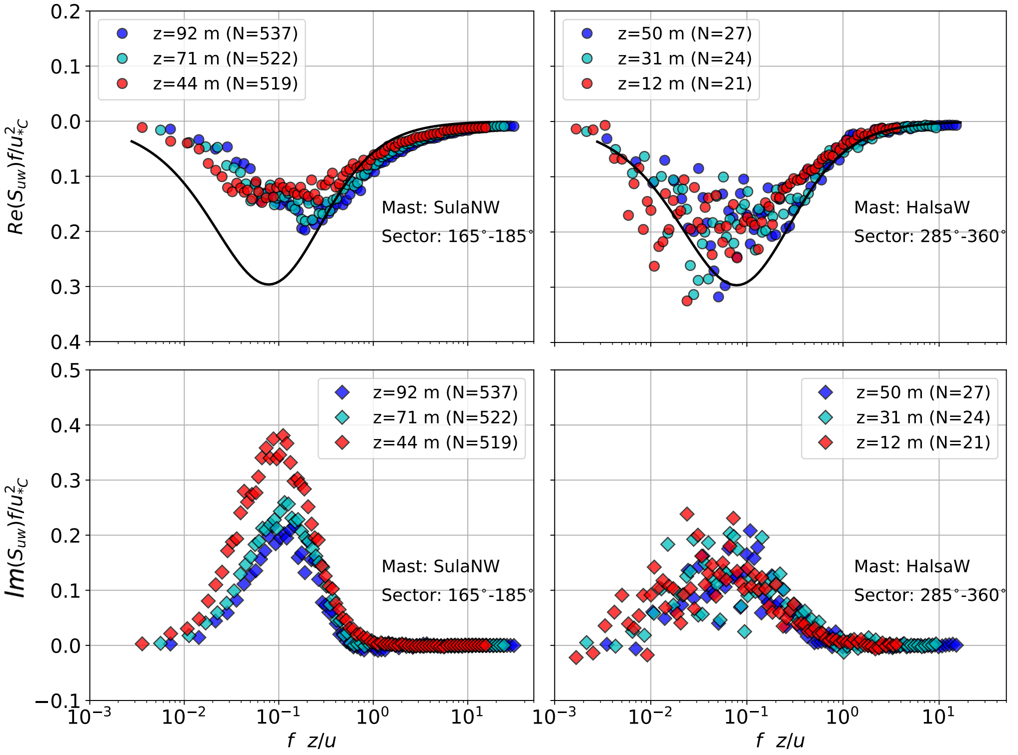

Figure 8: Normalized real and imaginary parts of the cross-spectrum S_{uw} estimated using the records from SulaNW and HalsaW from 01-01-2018 to 31-12-2019. The black line is the Kaimal model given in Eq. (12).

purpose are SulaNW for the sector 165°-185° and HalsaW for the sector 285°-360°.

The quad-spectrum reflects the blocking by the ground [24]. Therefore, the absolute value of the quad-spectrum should decrease with altitude. However, it is not always the case for the fjords analysed, where the quad-spectrum sometimes increases with height. This increase could be related to the fact that the terrain upstream to the masts is often heterogeneous. For long-fetch winds, the quad-spectra and co-spectra have similar amplitudes for all the met-masts analysed. This suggests that even for long-fetch winds, the blocking by the ground or the mountain slopes is not negligible. In many cases, the quad-spectrum estimates are substantially larger in absolute value than reported offshore [41].

Flow distortion by canopy, defined as the vegetation cover above ground, is sometimes visible in the velocity data recorded at heights around or below 30 m above the ground, as shown in fig. 9 for HalsaE (sector 150°-180°). The south side of HalsaE is dominated by a long fetch. The velocity spectrum at 31 m above the ground shows a narrow peak near $f_r \approx 0.5$, likely, reflecting distortion of the flow

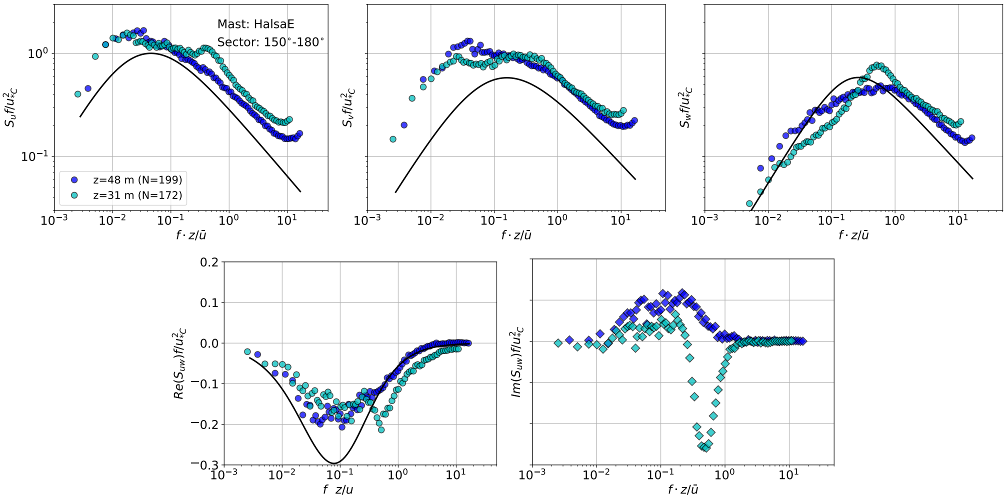

Figure 9: Canopy-induced flow distortion at $z = 31$ m is visible in the velocity spectra estimated at HalsaE (sector 150°-180°) between 01-01-2018 to 31-12-2019. The black lines are the Kaimal model (Eqs. (9) and (12)).

by a canopy, as previously observed by e.g. [58].

Spectral ratios

The spectral ratios between the vertical and along wind components are shown for some of the masts in fig. 10. For the sake of brevity, only three representative masts are selected due to the similarity of the findings. The resulting ratios can be classified into three groups as illustrated in table 5. The first group is the one in which S_w/S_u converges steadily towards 4/3. This is the case for HalsaE (sector 300°-360°) where the 4/3 value is reached at $f_r \geqslant 3$, which is consistent with [11]. The second is the group where the ratio is significantly higher than 4/3 at $f_r > 1$, which is the case for SulaNW (sector 165°-185°). For this sector, the three anemometers show similar ratios, which suggests that the observation is not related to an instrumental error. Yet, such a value is abnormally large, which might be linked to the presence of a hill upstream of the mast responsible for a large negative angle of attack, as indicated by [1]. For large negative incidence angles, flow separation may occur. In this situation, the vertical and along-wind components cannot be reliably retrieved using the double rotation technique.

The third group is the one in which the ratio S_w/S_u remains below 4/3, as observed for HalsaW (sector 150°-180°). Both flow distortion and aliasing can be responsible for such behaviour. In the present case, the three anemometers display a similar trend for S_w/S_u, indicating that flow distortion by the surrounding vegetation is unlikely to explain the failure of S_w/S_u to converge toward 4/3.

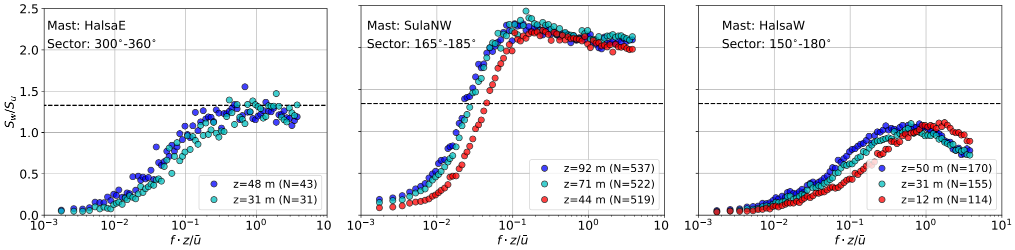

Figure 10: Spectral ratio S_w/S_u at SulaNW (sector 165°-185°), HalsaW (sector 150°-180°), and HalsaE (sector 300°-360°) from 01-01-2018 to 31-12-2019. The black dashed line is 4/3, which is a value representative of the local isotropy in the inertial subrange.

Table 5: Classification of the result obtained in spectral ratio calculation at $f_r \geqslant 3$; Group– I $S_w/S_u \to \frac{4}{3}$, Group– II $S_w/S_u > \frac{4}{3}$, Group– III $S_w/S_u < \frac{4}{3}$

Mast name	Sector	Group categories
SulaNW	135-165	II
	165-185	II
	300-330	II
SulaNE	300-20	II
	150-210	II
SulaSW	135-165	II
	285-315	II
	315-345	I
SulaSE	240-330	I
HalsaW	150-180	III
	285-360	I
HalsaE	150-180	III
	210-285	I
	300-360	I
JulWest	120-195	III
	330-360	I
JulEast	120-195	III
	210-285	I
	300-360	III

Figure 2 shows that aliasing is more important for the u component than for the w component. Therefore, the presence of aliasing is reflected by the negative slope of S_w/S_u at $f_r > 1$ as seen in the right panel of fig. 10. Without aliasing, the ratio would likely have converged toward 4/3.

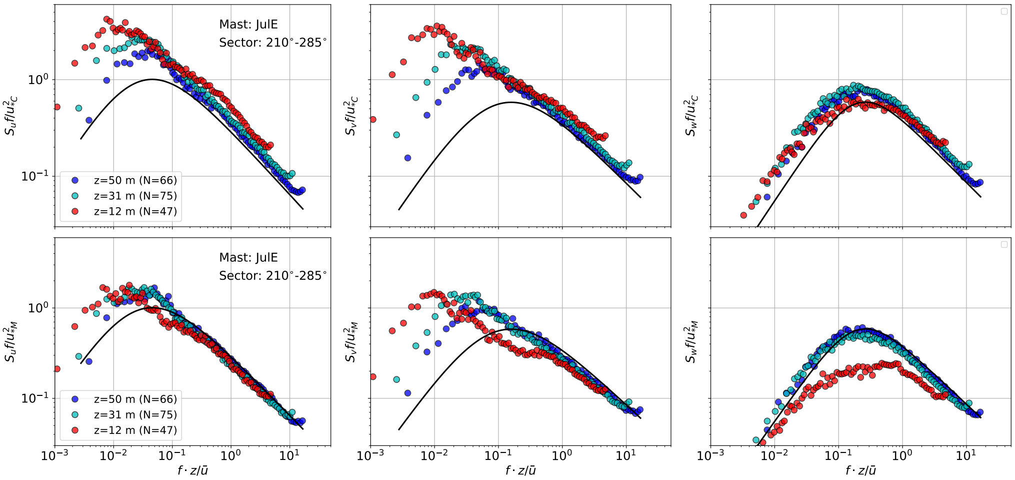

Figure 11: Along-wind, cross-wind, and vertical velocity spectra estimated at JulE (sector 210°-285°) for the period from 01-01-2018 to 31-12-2019. Top panel: the spectra are normalized by Eq. (5). Bottom panel: the spectra are normalized by Eq. (8). The black line is the Kaimal model given from Eq. (9) to Eq. (11).

5.2. Reassessment of the friction velocity as a scaling velocity

Some of the PSDs estimate are systematically above the Kaimal spectra, suggesting that the friction velocity used is underestimated. The underestimation cannot be corrected by using the surface friction velocity. Firstly, because the reduction of the friction velocity from the surface to the measurement height is unlikely to be large enough to explain the discrepancies observed. Secondly, because the terrain is heterogeneous, such that the friction velocity at the surface is not representative of the same roughness as at the anemometer position. Therefore, in this situation, extrapolation techniques are not recommended.

The adequacy of the local friction velocity u_* as scaling velocity is investigated by estimating it with the three different methods summarised in Eqs. (5), (6) and (8). The dataset from JulE (sector 210°-285°) is selected for velocity spectra indicating a possible bias in the estimation of u_*. The western side of JulE is characterized by a long fjord fetch, the length of which is the width of Julsundet. For this sector, the PSDs of the velocity fluctuations showed characteristics from long-fjord fetch but the imaginary part of the cross-wind spectra showed that the blocking by the ground or the surrounding hills was not negligible.

Figure 11 shows that the influence of the method to compute u_* on the amplitude of the spectra is significant. The method by Klipp (Eq. (6)) does not show clear difference with the classical method (Eq. (5)). The application of Eq. (8), on the other hand, leads to PSD estimates that satisfy Eqs. (1) and (2)

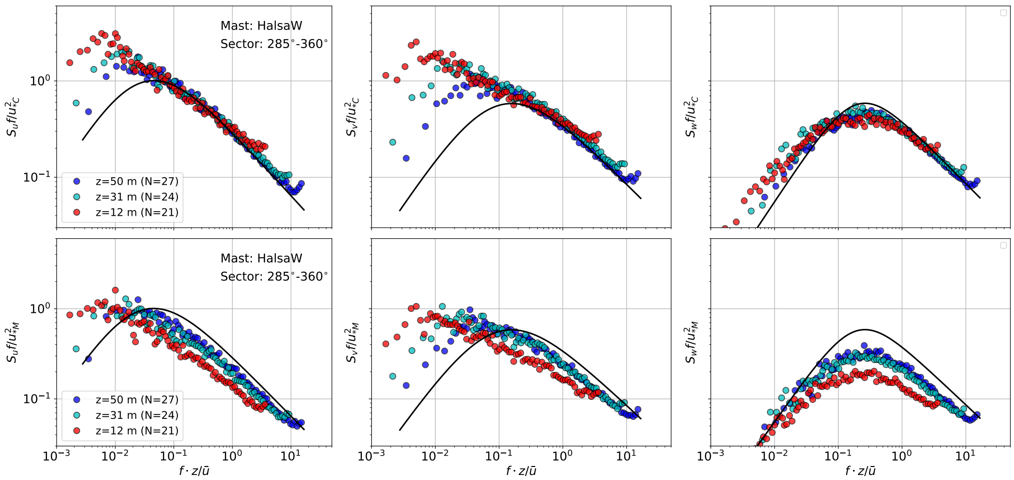

Figure 12: Velocity spectra estimated at HalsaW (sector 285°-360°) for the period from 01-01-2018 to 31-12-2019. Top panel: the spectra are normalized by Eq. (5). Bottom panel: the spectra are normalized by Eq. (8). The black line is the Kaimal model given from Eq. (9) to Eq. (11).

by superposing onto each other and with the Kaimal model at high frequencies. One exception is the S_w spectrum estimated using the data collected by the anemometer located at 12 m above the ground. These measurements are suspected to be influenced by the trees or the vegetation around the mast, as stated in [47]. The use of Eq. (8) indicates that surface layer scaling may be applicable in a Norwegian fjord, providing that it is based on an adequate determination of the friction velocity used as scaling parameter.

However, the application of Eq. (8) does not always seem adequate as shown by fig. 12. For the case at hand (HalsaW, sector 285°-360°), the underestimation of the friction velocity is less important than for JulE (sector 210°-285°). In addition, the use of Eq. (5) seems already appropriate as shown by the good agreement between the S_w spectrum and the Kaimal model in the high-frequency range. Therefore, in this situation, the application of Eq. (8) would not be recommended. Choosing the proper method to compute u_* cannot rely on the argument that the shear stress $u'v'$ is non-negligible compared to $u'w'$ only. One possible reason for the application of Eq. (8) instead of Eq. (5) might be the presence of a substantial horizontal mean wind shear, which is considerable in Sulafjorden or Julsundet compared to Halsafjorden [1]. A further investigation of the turbulent shear stresses in terms of quadrant analysis [59] might also help to identify situations where Eq. (6) or Eq. (8) would be preferred to Eq. (5).

5.3. ***Co-coherence***

Application of the Davenport model

Figure 13 displays the fitted decay coefficients for long-fetch and short-fetch winds. We remind the reader that the least-square fit is conducted by simultaneously considering every combination of measurement height. For long-fetch winds, the decay coefficients are found to vary as follow: $8.4 \leqslant C_z^u \leqslant 14.5$, $6.6 \leqslant C_z^v \leqslant 12.7$, and $3.0 \leqslant C_z^w \leqslant 7.3$. For short-fetch winds, the decay coefficient are similar as for long-fetch winds, with $8.5 \leqslant C_z^u \leqslant 14.2$, $5.7 \leqslant C_z^v \leqslant 13.0$, and $2.3 \leqslant C_z^w \leqslant 4.6$, respectively. The computed Davenport decay coefficients are similar for the two fetches considered. The range of values found is also similar to those found by [5], who also focused on two distinctive sectors with different topographic characteristics.

The decay coefficients estimated at SulaNE for a northwesterly wind coming from the ocean are remarkably close to those obtained offshore by [19], which were computed using similar altitudes and separations. This observation suggests that records obtained on the shore of a mountainous fjord open to the sea may, under certain conditions, exhibit flow characteristics similar to those observed in the offshore environment. The northwesterly wind is flowing past the mountainsides at SulaNW, which may explain why the decay coefficients estimated from this mast deviate from those obtained at SulaNE. The average values of the decay coefficients computed in fig. 13 are also similar to those from the handbook N400 for bridge design in Norway [60], which are $C_z^u = 10$, $C_z^v = 6.5$ and $C_z^w = 3$. However, the handbook N400 assumes that the decay coefficients are identical for lateral and vertical separations, which may not be the case in reality, especially in complex terrain.

Probabilistic approaches have been proposed for several decades to account for the observed variability of the decay coefficients [29, 61]. Figure 13 show that the variation of the decay coefficient is not negligible for wind load calculation. However, this variability is lower than reported in the literature, given the large variety of fetch and locations included in the present study. Over the last sixty years, the large scatter of the reported decay coefficients can partly be explained by the different environmental and experimental conditions. For vertical separations, the Davenport decay coefficient is known to depend on the spatial separation [62], the measurement height [45], the terrain roughness [42] and the thermal stratification of the atmosphere [19, 63]. Besides, the fitted decay coefficient can be biased, depending on the number of sensors used, the signal-to-noise ratio and the algorithm considered. Welch's method [48] is generally used to estimate the co-coherence. A crucial step for the application of this algorithm is the choice of the number of overlapping segments, which can significantly affect the value of the decay coefficient [24, 64]. Finally, it should be noted that the present study focuses on

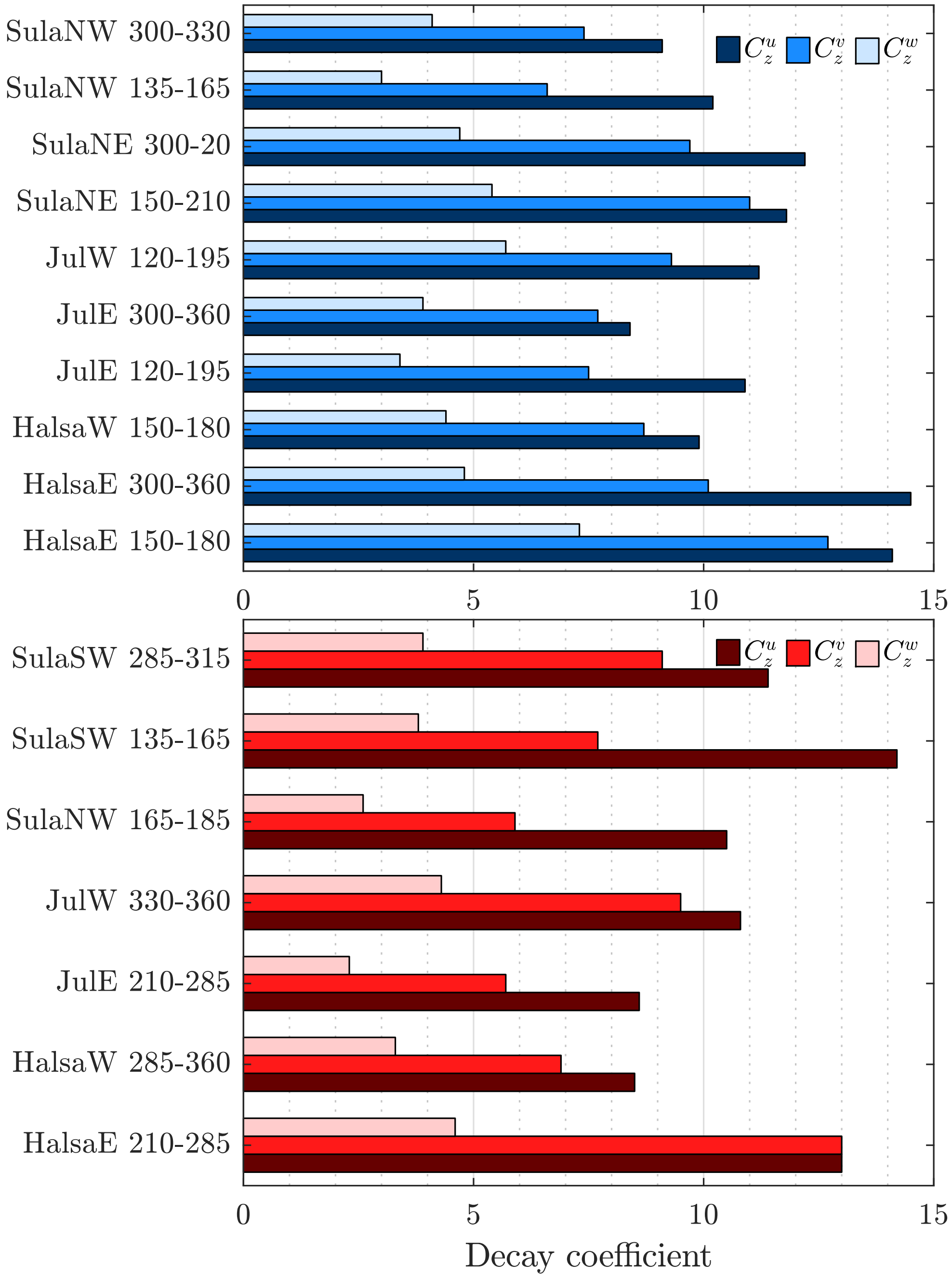

Figure 13: Davenport decay coefficient at Sulafjorden, Halsafjorden and Julsundet, for long-fetch winds (top) and short-fetch winds (bottom).

the co-coherence, which captures the simultaneous fluctuations of velocity along a line. However, the decay coefficient is sometimes estimated using the magnitude-squared coherence, which contrary to the co-coherence, does not converge toward zero at high-frequencies because it is a biased estimate. Although probabilistic methods are certainly valuable to assess the variability of turbulence characteristics, they should be used with caution if the source of uncertainties is unclear.

In the present case, the variability of the decay coefficients is likely due to the different measurement heights, separation distances between the sensors and the heterogeneity of the terrain. For example, most of the decay coefficients are slightly larger in Halsafjorden and Julsundet than in Sulafjorden because the anemometers on JulE, JulW, HalsaW and HalsaE are closer to the surface than those in Sulafjorden. The increasing values of the decay coefficients as the measurement height decreases reflect the presence of smaller eddies close to the surface. A large mean wind shear may also increase the uncertainties associated with the estimated decay coefficient because the coherence is a turbulence characteristic that is meaningful only if the flow is fairly homogeneous. Nevertheless, the dependency of the decay coefficients on the mean wind speed u is likely small, as suggested by e.g. [65], because the Davenport model accounts for the change of the coherence with u.

Application of alternative coherence models

Figure 14 shows the co-coherence estimates for each mast and the wind sectors selected. The solid lines correspond to a least-square fit with Eq. (19), which was referred to as the modified Bowen model. The dashed lines correspond to a least-square fit with the Davenport model.

Per definition, the Davenport coherence model reduces to a single curve when expressed as a function of $fd_z/\overline{u}$ which is called hereafter Davenport similarity. Although the application of Eq. (19) leads to a much better modelling of the vertical co-coherence than the Davenport model, the parameters C_1^i and C_2^i show also a greater variability than the Davenport decay coefficients. A larger scatter is expected since a higher number of free parameters than in the Davenport model is used. A further reduction of the variability of these coefficients could be achieved by combining separations below 10 m and other closer to 100 m, by increasing the number of sensors or assessing alternative fitting techniques. However, such investigations are out of the scope of the present study. In structural dynamics, the exponential decay function by [66] has the advantage of simplicity. This is likely the reason why it is adopted by [17] and subsequently in the [60] Handbook.

The modified Bowen model highlights the limits of the Davenport model to describe the variation of the decay coefficient with vertical separations. If a floating-bridge with pontoons is constructed in Sulafjorden, the proximity of the girder with the sea surface may require a reassessment of the Davenport model to

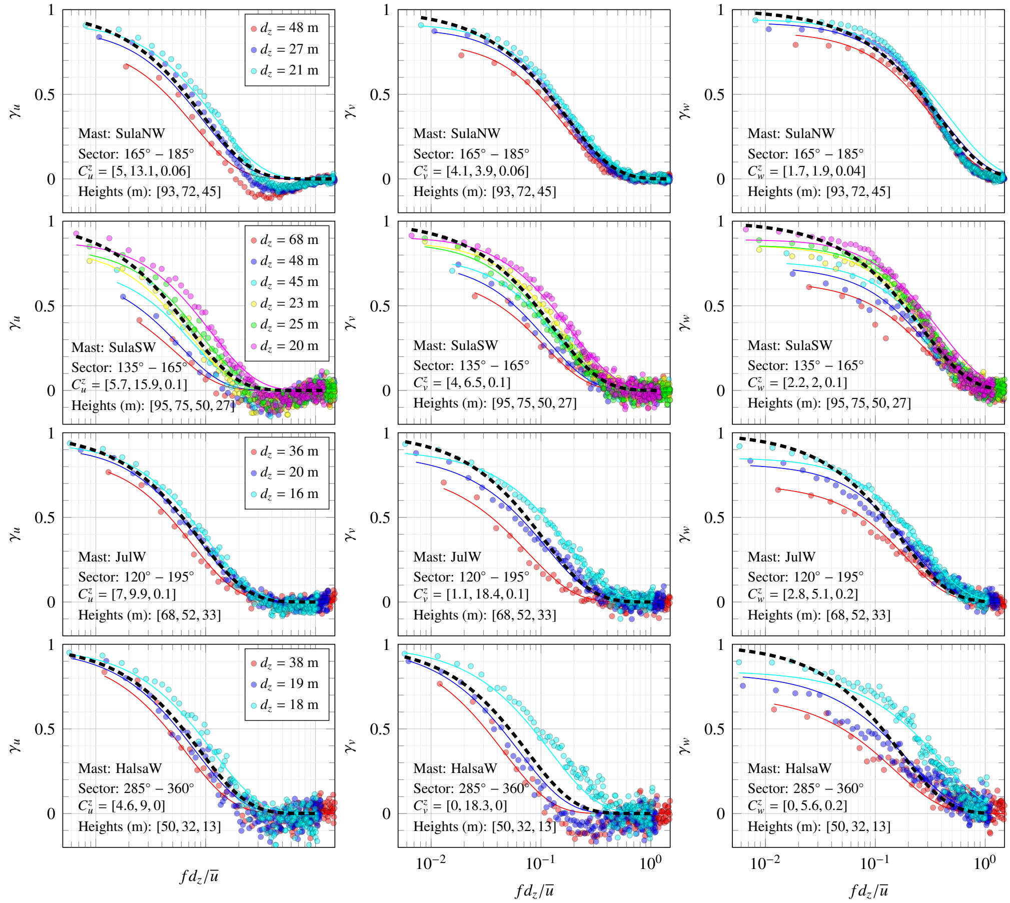

Figure 14: Along-wind, crosswind and vertical co-coherence for selected masts at Sulafjorden, Halsafjorden and Julsundet for the period from 01-01-2018 to 31-12-2019. The continuous lines are the fitted modified Bowen coherence model and the thick dashed lines correspond the Davenport model. In this figure, the notation C_z^i corresponds to $C_z^i = [C_1^i, C_2^i, C_3^i]$ where $i = \{u, v, w\}$.

adequately capture the spatial correlation of turbulence. A similar reassessment may be required for the bridge towers, which will be slender structures as high as 200 m [67]. They will be particularly sensitive to turbulent effects during the construction phase [68–70]. A preliminary comparison between the Davenport coherence model and the modified Bowen model was conducted for a vertical cantilever beam in [41]. The computation of the joint-acceptance functions, which quantifies the contribution of the co-coherence on the modal load, suggested that the Davenport model might lead to an overestimation of the turbulent load for the lowest modes of vibrations. A more detailed comparison for fjord-crossing bridges is, however, a topic for future work.

6. Conclusions

The present work complements the investigations carried out in Part – I, which assessed the integral flow characteristics. Here, we explored the spectral characteristics of turbulence to highlight the challenges and potential of wind measurements using met-masts located on the shoreline of the fjords. The understanding of these flow characteristics will help to identify spectral turbulence models suitable for wind engineering applications in mountainous terrain. Two years of continuous wind measurement on eight masts were analysed, at heights between 12 m and 95 m above ground. The study focused on wind speed relevant to turbulence-induced load in the context of bridge design, i.e. stationary wind conditions with mean wind speed $u > 12\,\mathrm{m\,s^{-1}}$. The influence of the local topography on turbulence was assessed in the frequency space, which led to the following findings:

- The power spectral densities (PSDs) of the along-wind and crosswind components, denoted S_u and S_v, respectively, displayed a higher amplitude at low frequencies for long-fetch wind compared to the short-fetch cases. In contrast, the PSD estimate S_w of the vertical component did not show any significant influence of the fetch on their low-frequency range. However, the S_w spectra, estimated in some met-masts and for some specific sectors, have a much higher spectral peak compared to the Kaimal model. The velocity spectra estimated for long-fetch wind often showed a double spectral peak and a spectral plateau.

- The ratio S_w/S_u reaches the theoretical value 4/3 on the mast HalsaE for the sector 300°-360° only. This mast is located in relatively flat terrain, as seen in Part – I of this study. In some cases, the spectral ratios suggest that high roughness moves the frequency at which local isotropy is reached beyond the highest frequency resolved by the anemometers. In several situations, aliasing, which was highlighted in the PSD estimates, prevented the ratio S_w/S_u from converging toward 4/3.

- The quad-spectrum $\mathrm{Im}(S_{uw})$ and the co-spectrum were often similar, which highlighted the possible blocking by the ground and/or by the mountain slopes. In flat terrain or offshore, $\mathrm{Im}(S_{uw})$ is generally much smaller than $\mathrm{Re}(S_{uw})$, especially when the height increases. For engineering practices, studying the quad-spectrum could be useful to complement the traditional terrain classification by the roughness length.

- The friction velocity u_* was computed using three different methods. The goal was to identify which one was adequate in complex terrain, assuming that surface-layer scaling is applicable in Norwegian fjords. Some of the normalized PSD estimates, for example on JulE (sector 210°-285°), showed a deviation from surface-layer scaling, which was attributed to biased values of u_*. In this case, the application of Klipp's method was not conclusive. However, in some cases, the use of the norm of all the off-diagonal components of the Reynolds stress tensors led to normalized PSDs that satisfied surface-layer scaling, at least in the higher-frequency range. Further work is required to identify which method to compute the friction velocity is best suited, depending on the terrain features.

- The study of the vertical coherence of turbulence indicated that the Davenport decay coefficient did not depend significantly on the upstream topography. Depending on the sector selected, the averaged values of these decay coefficients are consistent with the N400 handbook [60] and from the offshore platform FINO1 [19].
- The co-coherence estimates on the same met-mast rarely collapse into a single curve when expressed as a function of fd_z/u, contrary to what is predicted by the Davenport model. The application of coherence models derived from [45] and [41] highlighted the dependency of the coherence on dz and dz^2/z (z is the height above the ground and dz is the separation distance). Therefore, a more detailed assessment of the dependency of the Davenport decay coefficient on the separation and measurement height may be required in mountainous terrain.

The study by [1] showed that the integral turbulent characteristics estimated on the shores of fjord may not be easily extrapolated on their middle part. The present study elaborates and complements the findings in [1]. Through a spectral analysis, we showed that the differences between the integral turbulence characteristics in fjords and in flat terrain were largely due to the low-frequency fluctuations. More importantly, the high-frequency range of the velocity spectra was found to be compatible with the model by [11], which is advantageous for modelling purposes. Besides, the deployment of masts on the shores is also valuable for the safe design of bridges towers, which will be located close-by. The computation of the mean flow characteristics from multiple masts on the seaside is also meaningful for the validation of CFD models [53], which can be used to assess the wind conditions across the fjord. The combined use of met-mast measurements and numerical analysis can further be complemented by remote sensing of wind and/or wind tunnel tests.

The present study indicates that if the fjords are crossed by single-span suspension bridges or floating suspension bridges, the turbulent wind loading on the main span may be properly modelled using the Simiu & Scanlan model [14] and the Davenport model with the decay coefficients from the N400 handbook. If a floating pontoon bridge is constructed, the blocking by the sea surface may substantially affect the structure of turbulence and will therefore require a more in-depth investigation.

7. Acknowledgements

This work and the measurement campaign is financed by the Norwegian Public Roads Administration as part of the Coastal Highway E39 project in Mid-Norway. We also want to thank Birgitte R. Furevik, Jørn Kristiansen and Knut Helge Midtbø (Norwegian Meteorological Institute), Konstantinos Christakos (University of Bergen), and Adil Rasheed (Norwegian University of Science and Technology) for providing resources and guidance necessary for this work.

References

[1] Z. Midjiyawa, E. Cheynet, J. Reuder, H. Ágústsson, T. Kvamsdal, Potential and challenges of wind measurements using met-masts in complex topography for bridge design: Part 1–integral flow characteristics, *Journal of Wind Engineering and Industrial Aerodynamics*, p. 104584 (2021).

[2] H. P. Frank, A simple spectral model for the modification of turbulence in flow over gentle hills, *Boundary-Layer Meteorology*, 79:345–373 (1996).

[3] R. H. Scanlan, The action of flexible bridges under wind, II: Buffeting theory, *Journal of Sound and Vibration*, 60:201–211 (1978).

[4] A. G. Davenport, The spectrum of horizontal gustiness near the ground in high winds, *Quarterly Journal of the Royal Meteorological Society*, 87:194–211 (1961).

[5] M. Hui, A. Larsen, H. Xiang, 20092 wind turbulence characteristics study at the Stonecutters bridge site: Part – II wind power spectra, integral length scales and coherences, *Journal of Wind Engineering and Industrial Aerodynamics*, 97:48–59 (2009).

[6] E. Cheynet, J. B. Jakobsen, J. Snæbjörnsson, Buffeting response of a suspension bridge in complex terrain, *Engineering Structures*, 128:474–487 (2016).

[7] A. Fenerci, O. Øiseth, A. Rønnquist, Long-term monitoring of wind field characteristics and dynamic response of a long-span suspension bridge in complex terrain, *Engineering Structures*, 147:269–284 (2017).

[8] C. Yu, Y. Li, M. Zhang, Y. Zhang, G. Zhai, Wind characteristics along a bridge catwalk in a deep-cutting gorge from field measurements, *Journal of Wind Engineering and Industrial Aerodynamics*, 186:94–104 (2019).

[9] J.-L. Song, J.-W. Li, R. G. Flay, Field measurements and wind tunnel investigation of wind characteristics at a bridge site in a y-shaped valley, *Journal of Wind Engineering and Industrial Aerodynamics*, 202:104199 (2020).

[10] N. E. Busch, H. A. Panofsky, Recent spectra of atmospheric turbulence, *Quarterly Journal of the Royal Meteorological Society*, 94:132–148 (1968).

[11] J. C. Kaimal, J. C. Wyngaard, Y. Izumi, O. R. Coté, Spectral characteristics of surface-layer turbulence, *Quarterly Journal of the Royal Meteorological Society*, 98:563–589 (1972).

[12] H. W. Tieleman, Universality of velocity spectra, *Journal of Wind Engineering and Industrial Aerodynamics*, 56:55–69 (1995).

[13] T. von Kármán, Progress in the statistical theory of turbulence, *Proceedings of the National Academy of Sciences of the United States of America*, 34:530 (1948).

[14] E. Simiu, R. H. Scanlan, *Wind effects on structures: fundamentals and applications to design*, 3rd edition, John Wiley New York, 1996.

[15] A. S. Monin, A. M. Obukhov, Basic laws of turbulent mixing in the surface layer of the atmosphere, *Proceedings of the Geophysical Institute USSR Academy of Sciences*, 24:163–187 (1954).

[16] C. Dyrbye, S. O. Hansen, *Wind loads on structures*, 1997.

[17] EN 1991-1-4, Eurocode 1. Actions on structures – Part 1-4: General actions – Wind actions., Tech. rep., [Authority: The European Union Per Regulation 305/2011, Directive 98/34/EC, Directive 2004/18/EC] (2005).

[18] T. Mikkelsen, S. E. Larsen, H. E. Jørgensen, P. Astrup, X. G. Larsén, Scaling of turbulence spectra measured in strong shear flow near the earth's surface, *Physica Scripta*, 92:124002 (2017).

[19] E. Cheynet, J. B. Jakobsen, J. Reuder, Velocity spectra and coherence estimates in the marine atmospheric boundary layer, *Boundary-Layer Meteorology*, 169:429–460 (2018).

[20] H. Panosfsky, J. Dutton, *Atmospheric turbulence: Models and methods for engineering applications*, NewYork: JohnWiley&Sons, 1984.

[21] E. Morfiadakis, G. Glinou, M. Koulouvari, The suitability of the von karman spectrum for the structure of turbulence in a complex terrain wind farm, *Journal of wind engineering and industrial aerodynamics*, 62:237–257 (1996).

[22] I. ESDU, Characteristics of atmospheric turbulence near the ground – part ii: Single point data for strong winds (neutral atmosphere), *Engineering Sciences Data Unit, IHS Inc., London, UK, Report No. ESDU*, 85020 (2001).

[23] U. Högström, J. Hunt, A.-S. Smedman, Theory and measurements for turbulence spectra and variances in the atmospheric neutral surface layer, *Boundary-Layer Meteorology*, 103:101–124 (2002).

[24] J. Mann, The spatial structure of neutral atmospheric surface-layer turbulence, *Journal of Fluid Mechanics*, 273:141–168 (1994).

[25] A. N. Kolmogorov, The local structure of turbulence in incompressible viscous fluid for very large reynolds numbers, *Proceedings of the USSR Academy of Sciences*, 30:299–303 (1941).

[26] E. Cheynet, J. B. Jakobsen, J. Snæbjörnsson, Flow distortion recorded by sonic anemometers on a long-span bridge: Towards a better modelling of the dynamic wind load in full-scale, *Journal of Sound and Vibration*, 450:214–230 (2019).

[27] A. Peña, E. Dellwik, J. Mann, A method to assess the accuracy of sonic anemometer measurements, *Atmospheric Measurement Techniques*, 12:237–252 (2019).

[28] M. Chamecki, N. Dias, The local isotropy hypothesis and the turbulent kinetic energy dissipation rate in the atmospheric surface layer, *Quarterly Journal of the Royal Meteorological Society*, 130:2733–2752 (2004).

[29] G. Solari, G. Piccardo, Probabilistic 3-D turbulence modeling for gust buffeting of structures, *Probabilistic Engineering Mechanics*, 16:73–86 (2001).

[30] M. de Franceschi, D. Zardi, M. Tagliazucca, F. Tampieri, Analysis of second-order moments in surface layer turbulence in an Alpine valley, *Quarterly Journal of the Royal Meteorological Society*, 135:1750–1765 (2009).

[31] R. O. Weber, Remarks on the definition and estimation of friction velocity, *Boundary-Layer Meteorology*, 93:197–209 (1999).

[32] C. Klipp, Turbulent friction velocity calculated from the Reynolds stress Tensor, *Journal of the Atmospheric Sciences*, 75:1029–1043 (2018).

[33] C. L. Klipp, M. Adelphi, A new scaling term for use in roughness sublayers, in *18th Symp. on Boundary Layers and Turbulence, Stockholm, Sweden (9-13 June 2008)*, American Meteorological Society, 2008.

[34] J. C. Kaimal, J. J. Finnigan, *Atmospheric Boundary Layer Flows: Their Structure and Measurement*, Oxford University Press, 1994.

[35] Z. Sorbjan, On similarity in the atmospheric boundary layer, *Boundary-Layer Meteorology*, 34:377–397 (1986).

[36] B. Figueroa-Espinoza, P. Salles, Local monin–obukhov similarity in heterogeneous terrain, *Atmospheric Science Letters*, 15:299–306 (2014).

[37] J. C. Hunt, J. F. Morrison, Eddy structure in turbulent boundary layers, *European Journal of Mechanics-B/Fluids*, 19:673–694 (2000).

[38] J. C. Hunt, P. Carlotti, Statistical structure at the wall of the high Reynolds number turbulent boundary layer, *Flow, Turbulence and Combustion*, 66:453–475 (2001).

[39] T. Mikkelsen, S. E. Larsen, H. E. Jørgensen, P. Astrup, X. G. Larsén, Scaling of turbulence spectra measured in strong shear flow near the Earth's surface, *Physica Scripta*, 92:124002 (2017).

[40] P. Drobinski, P. Carlotti, R. K. Newsom, R. M. Banta, R. C. Foster, J.-L. Redelsperger, The structure of the near-neutral atmospheric surface layer, *Journal of the Atmospheric Sciences*, 61:699–714 (2004).

[41] E. Cheynet, Influence of the measurement height on the vertical coherence of natural wind, in *Conference of the Italian Association for Wind Engineering*, Springer, 2018, pp. 207–221.

[42] C. F. Ropelewski, H. Tennekes, H. A. Panofsky, Horizontal coherence of wind fluctuations, *Boundary-Layer Meteorology*, 5:353–363 (1973).

[43] J. Kanda, R. Royles, Further consideration of the height dependence of root-coherence in the natural wind, *Building and Environment*, 13:175–184 (1978).

[44] J. Kanda, Reliability of gust response prediction considering height dependent turbulence parameters, *Journal of Wind Engineering and Industrial Aerodynamics*, 14:455–466 (1983).

[45] A. J. Bowen, R. G. Flay, H. A. Panofsky, Vertical coherence and phase delay between wind components in strong winds below 20 m, *Boundary-Layer Meteorology*, 26:313–324 (1983).

[46] L. Kristensen, N. O. Jensen, Lateral coherence in isotropic turbulence and in the natural wind, *Boundary-Layer Meteorology*, 17:353–373 (1979).

[47] B. R. Furevik, H. Ágústson, A. Lauen Borg, M. Zakari, F. Nyhammer, M. Gausen, Meteorological observations in tall masts for mapping of atmospheric flow in Norwegian fjords, *Earth System Science Data Discussions*, pp. 1–28 (2020).

[48] P. Welch, The use of fast fourier transform for the estimation of power spectra: a method based on time averaging over short, modified periodograms, *IEEE Transactions on Audio and Electroacoustics*, 15:70–73 (1967).

[49] G. Carter, C. Knapp, A. Nuttall, Estimation of the magnitude-squared coherence function via overlapped fast fourier transform processing, *IEEE Transactions on Audio and Electroacoustics*, 21:337–344 (1973).

[50] A. Savitzky, M. J. Golay, Smoothing and differentiation of data by simplified least squares procedures., *Analytical Chemistry*, 36:1627–1639 (1964).

[51] Y. Fujino, Vibration-based monitoring for performance evaluation of flexible civil structures in japan, *Proceedings of the Japan Academy, Series B*, 94:98–128 (2018).

[52] A. Fenerci, O. Øiseth, Site-specific data-driven probabilistic wind field modeling for the wind-induced response prediction of cable-supported bridges, *Journal of Wind Engineering and Industrial Aerodynamics*, 181:161–179 (2018).

[53] E. Cheynet, S. Liu, M. C. Ong, J. B. Jakobsen, J. Snæbjörnsson, I. Gatin, The influence of terrain on the mean wind flow characteristics in a fjord, *Journal of Wind Engineering and Industrial Aerodynamics*, 205:104331 (2020).

[54] H. Panofsky, D. Larko, R. Lipschutz, G. Stone, E. Bradley, A. J. Bowen, J. Højstrup, Spectra of velocity components over complex terrain, *Quarterly Journal of the Royal Meteorological Society*, 108:215–230 (1982).

[55] J. Højstrup, A simple model for the adjustment of velocity spectra in unstable conditions downstream of an abrupt change in roughness and heat flux, *Boundary-Layer Meteorology*, 21:341–356 (1981).

[56] B. Yu, A. Gan Chowdhury, F. J. Masters, Hurricane wind power spectra, cospectra, and integral length scales, *Boundary-Layer Meteorology*, 129:411–430 (2008).

[57] A. K. Iyengar, C. Farell, Experimental issues in atmospheric boundary layer simulations: roughness length and integral length scale determination, *Journal of Wind Engineering and Industrial Aerodynamics*, 89:1059–1080 (2001).

[58] E. Dellwik, F. Bingöl, J. Mann, Flow distortion at a dense forest edge, *Quarterly Journal of the Royal Meteorological Society*, 140:676–686 (2014).

[59] R. H. Shaw, J. Tavangar, D. P. Ward, Structure of the Reynolds stress in a canopy layer, *Journal of Climate and Applied Meteorology*, 22:1922–1931 (1983).

[60] Norwegian Public Road Administration, *N400 Handbook for Bridge Design*, Directorate of Public Roads (2015).

[61] K. Hoffmann, R. Srouji, S. Hansen, Wind effects on long-span bridges: Probabilistic wind data format for buffeting and VIV load assessments, *MS&E*, 276:012005 (2017).

[62] L. Kristensen, H. A. Panofsky, S. D. Smith, Lateral coherence of longitudinal wind components in strong winds, *Boundary-Layer Meteorology*, 21:199–205 (1981).

[63] R. Soucy, R. Woodward, H. Panofsky, Vertical cross-spectra of horizontal velocity components at the boulder observatory, *Boundary-Layer Meteorology*, 24:57–66 (1982).

[64] K. Saranyasoontorn, L. Manuel, On the propagation of uncertainty in inflow turbulence to wind turbine loads, *Journal of Wind Engineering and Industrial Aerodynamics*, 96:503–523 (2008).

[65] W. Schlez, D. Infield, Horizontal, two point coherence for separations greater than the measurement height, *Boundary-Layer Meteorology*, 87:459–480 (1998).

[66] A. G. Davenport, The application of statistical concepts to the wind loading of structures., *Proceedings of the Institution of Civil Engineers*, 19:449–472 (1961).

[67] J. Wang, E. Cheynet, J. Snæbjörnsson, J. B. Jakobsen, Coupled aerodynamic and hydrodynamic response of a long span bridge suspended from floating towers, *Journal of Wind Engineering and Industrial Aerodynamics*, 177:19–31 (2018).

[68] K. Ogawa, M. Matsumoto, M. Kitazawa, T. Yamasaki, Aerodynamic stability of the tower of a long-spanned cable-stayed bridge (Higashi-Kobe Bridge), *Journal of Wind Engineering and Industrial Aerodynamics*, 33:349–358 (1990).

[69] R. Wardlaw, Wind effects on bridges, *Journal of Wind Engineering and Industrial Aerodynamics*, 33:301–312 (1990).

[70] G. Larose, A. Zasso, S. Melelli, D. Casanova, Field measurements of the wind-induced response of a 254 m high free-standing bridge pylon, *Journal of Wind Engineering and Industrial Aerodynamics*, 74:891–902 (1998).

Paper III

Nested computational fluid dynamic modelling – AROME-SIMRA

Zakari Midjiyawa, Jon Vegard Venås, Trond Kvamsdal, Arne Morten Kvarving, Knut Helge Midtbø, and Adil Rasheed

Prepared for submission in *Journal of Wind Engineering and Industrial Aerodynamic*

ISBN 978-82-326-5901-2 (printed ver.)
ISBN 978-82-326-6266-1 (electronic ver.)
ISSN 1503-8181 (printed ver.)
ISSN 2703-8084 (online ver.)

NTNU
Norwegian University of
Science and Technology